Magnetoelastic instabilities in soft composites with ferromagnetic hyperelastic phases

by

Parag Pathak

A dissertation submitted in partial fulfillment
of the requirements for the degree of

Doctor of Philosophy
(Mechanical Engineering)

at the
University of Wisconsin-Madison
2023

Date of Final Oral Exam: December 15th 2023
The dissertation is approved by the following members of the Final Oral Committee:
Stephan Rudykh, Professor of Mechanical Engineering
Shiva Rudraraju, Professor of Mechanical Engineering
Melih Eriten, Professor of Mechanical Engineering
Xiaoping Qian, Professor of Mechanical Engineering
Pavana Prabhakar, Professor of Civil and Environmental Engineering

Abstract

In this dissertation, we investigate the microscopic and macroscopic instabilities developing in magneto-active elastomer (MAE) composites undergoing large deformations in the presence of an external magnetic field. In particular, we consider the MAEs with bi-phasic layered microstructure, with phases exhibiting ferromagnetic behavior. We first start with a basic introduction of MAEs where we introduce the model, characterization, and applications of MAEs. In the theoretical model, we go into the governing equations of the problem that we are trying to solve and lay the foundations for modeling MAEs. We discuss the energy models used in the neo-Hookean with linear magnetic model and the Langevin model (for ferromagnetic materials) which describes the saturation effects. To improve our energy model, we consider adding magnetic energy invariants (I_4, I_5, and I_6) (similar to the energy model for dielectric elastomers). In the analysis section, we then derive an explicit expression for the magnetic field-induced deformation of MAEs with hyperelastic phases. To perform the magneto elastic instability analysis, we employ the small-amplitude perturbations superimposed on finite deformations in the presence of the magnetic field. We examine the interplay between the macroscopic and microscopic instabilities. We find that the layered MAEs can develop microscopic instability with antisymmetric buckling modes, in addition to the classical symmetric mode. Notably, the antisymmetric microscopic instability mode does not appear in a purely mechanical scenario (when a magnetic field is absent). Furthermore, our analysis reveals that the wavelength of buckling patterns is highly tunable by the applied magnetic field, and by the properties and volume fractions of the phases. We find that the effects of I_4, I_5, and I_6 decrease with an increase in permeability. Our findings provide the information for designing materials with reconfigurable microstructures. This material ability can be used to actively tune the behavior of materials by a remotely applied magnetic field. The results can be utilized in designing tunable acoustic metamaterials, soft actuators, sensors, and shape-morphing devices.

Acknowledgements

I would like to thank all the people who are part of this journey, I would like to express sincere gratitude towards my Ph.D. advisor Professor Stephan Rudykh for being a great mentor and friend. His generosity with his time, knowledge, and passion for scientific discovery has helped me to become a much better researcher. I am especially thankful to the Mechanical Engineering Department of the University of Wisconsin–Madison for the generous assistantships I received, which were fundamental for my Ph.D. studies. I would also like to thank all my friends and colleagues at the university who encouraged me to keep going and supported me during this journey.

Declaration

I hereby declare that the work presented here is my own. All works that belong to others have been appropriately cited.

Contents

List of Figures

Chapter 1

Introduction

Magneto-active (MA) materials have become one of the essential smart metamaterials because of their wide range of potential applications. They are broadly classified into magnetorheological fluids (MRFs) and Magneto-active elastomers (MAEs). Their main difference is their effective properties, i.e., MAE devices produce variable stiffness. In contrast, fluids and other non-solid-state devices produce variable damping co-efficient and other fluid-related flow behaviors. In this dissertation, we will mainly focus on the instabilities of magnetoactive elastomers. However, before we begin the discussions regarding instabilities, we will cover some theories about the properties, structure, and applications of MAEs.

1.1 Magnetoactive elastomers (MAEs)

Magnetoactive elastomers (MAEs) belong to a class of soft active materials that respond to a remotely applied magnetic field. The application of magnetic field results in the modification of mechanical behavior and deformation (also referred to as *magnetostriction*). Let us now go over the background for the fabrication, characterization, and magnetostriction of MAEs.

1.1.1 Fabrication

The fabrication of MAEs is done by adding ferromagnetic particles (or fillers with high magnetic permeability) to an elastic material. Ferromagnetic particles (or fillers with high magnetic permeability) such as Carbonyl-iron (CI) particles are added as soft magnetizable microparticles. The magnetizable particles (from micro to nano-size) are added to the matrix material in its liquid state. Upon polymerization, the MAEs with randomly distributed magnetizable particles are produced. Curing in the presence of magnetic field

results in the alignment of magnetizable particles into chain-like structures, as shown in Fig. 1.1 (for a detailed description of the MAE synthesis, interested readers are referred to the review article by Bastola et al., 2020).

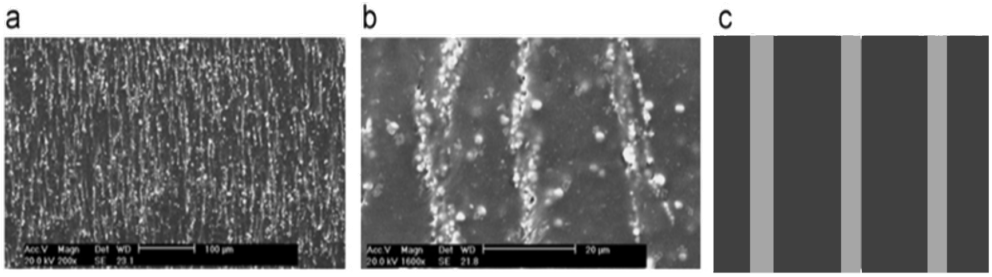

(a) MRE (800 mT) X200. (b) MRE (800 mT) X1600. (c) Idealized MRE.

Figure 1.1: (a) SEM image with 200 times magnification of MRE prepared in 800 mT (Chen et al., 2007); (b) SEM image with 1600 times magnification of MRE prepared in 800 mT (Chen et al., 2007); (c) Schematic representation of the idealized layered microstructure considered in this work.

We shall now understand the materials used to create soft magnetoactive elastomers. In principle, MAEs are composite materials consisting of magnetizable particles (for example, carbonyl iron, nickel, or Terfenol-D) embedded in an elastomeric matrix material such as silicone rubber, polyurethane (Jolly et al., 1996a). The behavior and features of the MAEs highly depend on the properties of the bulk matrix materials and the embedded magnetic fillers. The distribution of the magnetic particles within the matrix can also strongly affect the properties of MAEs. In other words, we can use these changes in properties to effectively "tune" our MAEs to get desired effects. On the other hand, the matrix materials provide the necessary elastomeric properties required for large deformation. These materials are usually magnetically inactive. They are mechanically soft with an elastic modulus in the range of 10 kPa to 10 GPa (Rus and Tolley, 2015). Some examples of matrix materials are polyurethanes (PU), vinyl rubbers (VR), polybutadiene rubber, thermosets/thermoplastics elastomers, silicone rubbers (SR), natural rubbers (NR), and synthetic rubbers such as Ethylene propylene diene monomer (EPDM) (Ginder et al., 2002; Bednarek, 1999; Guan et al., 2008). Among these, silicone rubbers are the most widely used elastomeric materials. CI is a popular choice for magnetic particles because of its high magnetic saturation (700 mT), low magnetic remanence, high magnetic permeability, and negligible magnetic hysteresis. Other choices include magnetic particles such as iron-cobalt, cobalt, nickel, Terfenol-D, and iron sands (Guan et al., 2007; Jolly

et al., 1996b; Bednarek, 2000). The distribution of particles and their concentration can also significantly influence magneto-deformation.

1.1.2 Characterization

There is a significant body of studies concerning the magneto-mechanical characterization of MAEs with different microstructures – random and chain-like – present in the literature. For example, Jolly et al. (1996a) and Danas et al. (2012) studied the shear response of chain-structured MAEs, showing that effective shear modulus increases in the presence of a magnetic field. The effective moduli of MAEs are also reported to be increased by the applied magnetic field under uniaxial compression (Abramchuk et al., 2006) and tensile tests (Soria-Hernández et al., 2019). The magnetostriction of MAEs with randomly distributed magnetizable particles under a very high magnetic field is analyzed by Bednarek (1999).

1.1.3 Magnetostriction

Magnetostriction is defined as the change in the dimensions of materials under the influence of an external magnetic field. The range of motion is very small for ferromagnetic materials such as cobalt, nickel, and iron. For example, after saturation is reached, the stretch ratios of these materials are of the order 1 - 10 [μm/m] (Guan et al., 2008). As far as applications are concerned, the ideal behavior of an MAE would be to generate significant, perfectly reversible deformation by applying small magnetic fields. That's where composites come into the picture. By combining materials that have large reversible elastomeric deformation properties and large reversible magnetic interactions, we can get almost perfect MAE and also be able to tune such behavior for our applications.

When combined with magnetic materials, soft polymer-based materials can significantly impact magnetostriction. Also, large magnetically induced deformation is possible based on the selection of the materials in soft magnetoactive materials. The magnetostriction further increases with the increase in magnetic field-induced Maxwell stress. Therefore, particles with high permeability, such as iron and iron oxides, are usually employed to fabricate MAEs (Rigbi and Jilken, 1983; Guan et al., 2008; Zrínyi et al., 1996). For a free-standing MAE sample in a uniform magnetic field, the deformation is approximately uniform (Tan et al., 2020).

These materials have found applications in stretchable electronics and nonplanar configurations (Scott, 2012). Ginder et al. (2002) and Guan et al. (2008) determined the magnetostriction of random and chain-structured MAEs. The effect of particle rotation on the effective magnetization of MAEs is investigated by Lanotte et al. (2003a). Moreno

et al. (2021) provided a comprehensive experimental characterization of MAEs focusing on the material response under various strain rates. Dargahi et al. (2019) performed the dynamic characterization of MAEs subjected to a wide range of excitation frequencies and magnetic flux densities. In these studies, the magnetizable particles are effectively rigid compared to the elastomer matrix. Therefore, the magneto-mechanical coupling observed in these MAEs is majorly governed by the two underlying mechanisms, namely, magnetic torques and magnetic interaction between the particles.

The pioneering works of Brown (1966), Maugin and Eringen (1972), Tiersten (1964), Toupin (1956), Truesdell and Toupin (1960) laid the foundation for the theory of magnetoelastic (and mathematically analogous electro-elastic) behavior of continuum, which has been reformulated and further developed by Dorfmann and Ogden (2004a), Kankanala and Triantafyllidis (2004), Vu and Steinmann (2007). In parallel, many microstructural-based magneto-elastic constitutive models are also developed—for example, the lattice model (Garcia-Gonzalez and Hossain, 2020; Ivaneyko et al., 2014; Jolly et al., 1996a).

Additionally, significant efforts have been made to implement the non-linear magnetoelastic framework into numerical schemes (Keip and Rambausek, 2017; Javili et al., 2013; Keip and Rambausek, 2016). Ponte Castañeda and Galipeau (2011) proposed an analytical approach to estimate the effective behavior of MAEs with the random distribution of magnetoactive particles. In particular, they developed a finite strain non-linear homogenization framework to determine the total magnetoelastic stress in MAEs under the combined mechanical and magnetic loading. By employing this framework, Galipeau and Ponte Castañeda (2012) studied the effects of randomly distributed magnetizable particle shape, distribution, and concentration on the effective properties of MAEs. Moreover, Galipeau et al. (2014) investigated the behavior of MAEs with periodic arrangements of circular and elliptical fibers, showing that by tailoring the periodic micro-structure of MAEs, their magneto-mechanical behavior could be highly tuned. We note that these systems share some similarities with their mathematically analogous dielectric elastomer composites (Rudykh et al., 2013; Tian et al., 2012; Goshkoderia et al., 2020a).

1.1.4 Soft magnetic materials

When magnetic materials are subjected to magnetic fields, they are observed to retain some magnetization, even after the magnetic field is removed. This ability to retain the magnetization is known as hysteresis. The different parameters that characterize hysteresis are shown in Fig. 1.2. For details refer (Szczygłowski, 2001; Jiles and Atherton, 1983; Stoner and Wohlfarth, 1991).

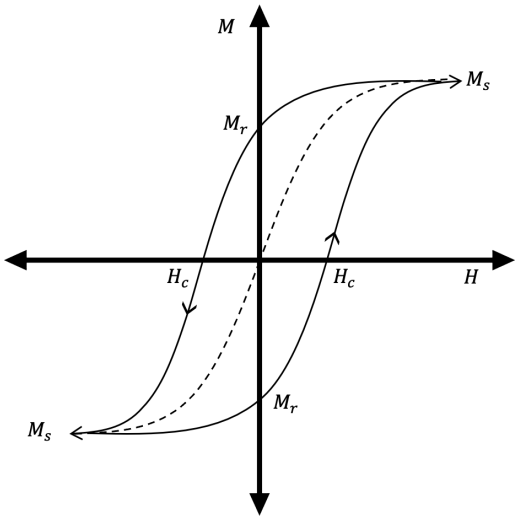

Figure 1.2: Schematic representation of the hysteresis showing the magnetic coercivity H_c, magnetic remanence M_r, and saturation magnetization M_s. A ferromagnetic saturation behavior is assumed for the applied magnetic field. The dotted line (- -) represents the ideal behavior without hysteresis, while the solid $(-)$ line represents the behavior with hysteresis. (Zhang and Rudykh, 2022; Bira et al., 2020).

Coercivity H_c, (see Fig. 1.2), also called magnetic coercivity, coercive field, or coercive force, is defined as the resistance of a magnetic material to changes in magnetization, equivalent to the field intensity necessary to demagnetize the fully magnetized material. It measures the ability of a ferromagnetic material to withstand an external magnetic field without becoming demagnetized. Hysteresis is considered a lossy phenomenon with respect to energy. Therefore, it is undesirable when rapid fluctuations in the magnetic field are involved, as happens in the various applications of MAEs (McHenry, 2001). Based on the magnitude of the hysteresis, ferromagnetic materials are broadly classified as either hard or soft, depending on how easily the materials can be magnetized and demagnetized. Although in this dissertation, we mainly focus on soft magnetic materials, it is worth noting the differences between them to understand properties that would suit our applications.

Soft magnetoactive materials have a low hysteresis and can be easily magnetized and demagnetized; in other words, their magnetization is easily reversible. Although there is not a strict criterion to distinguish soft and hard magnetic materials, soft magnetic materials show a low coercivity H_c of $(10^{-1} - 10^2 A/m)$, and high M_s (Inoue and Kong, 2022). Technical properties of interest for soft magnets include (i) high permeability, (ii) low hysteresis loss, and (iii) low eddy current and anomalous losses. Soft magnetic materials are used primarily to enhance the flux produced by an electric current. A typical

hysteresis loop of soft and hard magnetic materials is shown in Fig. 1.3.

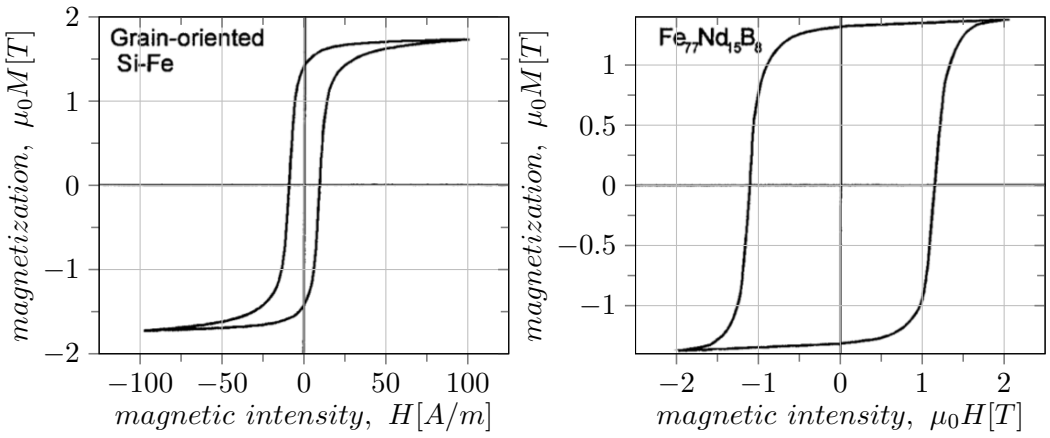

(a) Soft magnetic materials ($H_c \approx 10$ A/m)

(b) Hard magnetic materials ($H_c \approx 10^6$ A/m)

Figure 1.3: magnetization vs. the magnetic field, hysteresis curves for different magnetic field values describing the coercivity H_c and residual magnetic field B_r and the magnetic remanence, M_r for (a) hard and (b) soft magnetic materials(Bertotti, 1998; Bira et al., 2020).

In contrast, hard magnetic materials act more like permanent magnets and require a higher magnetic field (also known as a coercive force) to demagnetize them and show a large coercivity of $(10^3 - 10^5 A/m)$ (Inoue and Kong, 2022; Attard et al., 2021) and high magnetic remanence M_r.

Recently, particles of hard magnetic materials or high-coercivity ferromagnetic materials, including NdFeB, hard ferrite, and alnico alloys, have been used in the creation of hard-magnetic active elastomers (hMAEs) (Lum et al., 2016; Kim et al., 2018b; Zhao et al., 2019; Mukherjee et al., 2021). These new magnetoactive composites exhibit programmable and intricate shape transformations at low magnetic fields (Mukherjee et al., 2021; Garcia-Gonzalez and Hossain, 2021; Yan et al., 2021; Moreno-Mateos et al., 2023). Notebly, once exposure to a substantial magnetic field, hard magnetic materials retain their magnetization even after the removal of the external field. The high coercivity characteristics enables these materials to maintain their remanent magnetization over a wide range of applied magnetic fields below the coercive field strength. When the applied magnetic field does not align with the magnetization direction of the hard magnetic particles, the induced magnetic torque endeavors to align the particle's magnetization direction with the applied field, resulting in the deformation of the hMAE composite (Montgomery et al.,

2020; Alapan et al., 2020; Moreno-Mateos et al., 2022; Yan et al., 2023).

1.1.5 Applications

Due to their simple, remote, and reversible principle of operation, MAEs can provide the material platform for applications such as creating a variety of actuators and sensors. As the macroscopic stiffness of MAEs can be modified smoothly, quickly, and reversibly by applying a magnetic field, the macroscopic response of MAEs can be actively controlled in real-time. Additionally, the strain in the MAE composites can also change the overall magnetization, which could be detected by magnetometers or other sensors. This also makes their application well-suited for different sensors. Some examples of applications are variable-stiffness devices

The remote and reversible shape-transformative properties of hMAEs have paved the way for versatile applications in areas such as soft robotics (Hu et al., 2018; Cui et al., 2019), biomedical devices (Wang et al., 2021), and mechanical metamaterials (Chen et al., 2021; Zhang and Rudykh, 2022; Sim et al., 2023; Alam et al., 2023; Zhang et al., 2023b; Zhang et al., 2023a; Yang and Keten, 2023; Pal and Sitti, 2023).

(Sunaryono et al., 2013; Varga et al., 2005; Yoon et al., 2013; Erb et al., 2012; Ginder et al., 2002), self-assembly and self-organization (Piranda et al., 2021), mechanical metamaterials (Chen et al., 2021), tunable vibration absorbers (Ginder et al., 2001a; Wang et al., 2018; Sun et al., 2016; Deng et al., 2006), damping devices (Gong et al., 2012; Yang et al., 2012; Lerner and Cunefare, 2008; Ginder et al., 2001b; Deng et al., 2006; Hoang et al., 2011), sensors (Lanotte et al., 2003b; Tian et al., 2011; Zadov et al., 2012; Bednarek, 2000; Lanotte et al., 2003a; Kawasetsu et al., 2018), biomedicine (Bowen et al., 2015; Crivaro et al., 2016; Wang et al., 2021; Qi et al., 2020; Makarova et al., 2016; Luo et al., 2019; Zhou et al., 2021) noise barriers (Farshad and Le Roux, 2004; Karami Mohammadi et al., 2019; Yu et al., 2018), remotely controlled actuators (Ciambella et al., 2017; Kim et al., 2020; Tang et al., 2018; Stanier et al., 2016; Kim et al., 2018a), soft robotics (Hu et al., 2018; Yim and Sitti, 2011; Anil et al., 2021; Cui et al., 2019; Kim et al., 2019; Tang et al., 2019),

1.2 Instabilities

While the heterogeneity provides access to tailored and enhanced coupled behavior, it is also a source for developing micro-structural instabilities. The instability phenomenon historically has been considered a failure mode, which is to be predicted and avoided. This motivated the investigation of instabilities in composites subjected to purely mechanical

loading (Pathak et al., 2022; Arora et al., 2020; Geymonat et al., 1993; Greco et al., 2020; Li et al., 2021; Li et al., 2019; Rosen, 1965; Rudykh and deBotton, 2012; Arora et al., 2019; Slesarenko and Rudykh, 2017; Triantafyllidis and Maker, 1985; Arora et al., 2022).

The elastic instability phenomenon has recently been embraced to design materials with unusual properties and switchable functionalities (Florijn et al., 2016; Kochmann and Bertoldi, 2017). Examples include instability-induced elastic wave band gaps (Bertoldi and Boyce, 2008; Rudykh and Boyce, 2014), auxetic behavior (Li et al., 2018; Shim et al., 2013; Li and Rudykh, 2019), and photonic switches (Krishnan and Johnson, 2009). The possibility of controlling the instability development via a magnetic field can provide the opportunity to activate these functionalities remotely.

Extending the instability analysis for the coupled magneto-mechanical case, Ottenio et al. (2008) studied the onset of magneto-mechanical instabilities in isotropic MAEs with a focus on surface instabilities of a homogeneous magnetoactive half-space. Kankanala and Triantafyllidis (2008) investigated the failure modes of a rectangular MAE subjected to plane-strain loading conditions in the presence of a magnetic field. Rudykh and Bertoldi (2013) analyzed the onset of macroscopic instabilities in anisotropic MAEs by deriving the exact solution for MAEs with layered microstructure. Danas and Triantafyllidis (2014) studied the finite-wavelength instability modes occurring in an MAE substrate/layer system under a transverse magnetic field. Recently, Goshkoderia and Rudykh (2017) employed a numerical finite element-based code to investigate macroscopic instabilities in MAEs with circular and elliptical inclusions. Very recently, Goshkoderia et al. (2020b) experimentally illustrated that the instability pattern can be tailored by the application of magnetic field in particulate magnetoactive composites.

Motivated by recent experimental studies showing the tunability of finite-wavelength instabilities via magnetic field (Goshkoderia et al., 2020b; Psarra et al., 2017), in this work, we study the onset of microscopic instabilities and associated buckling patterns in MAEs. In particular, we consider the MAEs with biphasic layered microstructure exhibiting ferromagnetic behavior. To investigate the onset of instabilities, we consider the small-amplitude perturbations superimposed on finite deformations in the presence of a magnetic field to perform the microscopic instability analysis. Moreover, we analyze the limit corresponding to the long-wave or macroscopic instability. We examine the influences of the applied magnetic field and material parameters on MAE's stability. Additionally, we study the magnetostriction of layered MAEs and derive an explicit expression for the induced stretch as a function of the applied magnetic field, mechanical and magnetic properties of layers, and their volume fractions.

1.3 Structure of this dissertation

This dissertation is structured as follows:

- Chapter 2 presents the theoretical background on magneto-elastics and incremental analysis together with the constitutive laws for magnetically linear and ferromagnetic behavior.
- Chapter 3 is concerned with the analysis of the magneto-deformation and determination of the microscopic and macroscopic instabilities in layered MAEs.
- Chapter 4 illustrates the results with examples of magnetostriction and magnetoelastic instabilities in MAEs with various morphologies and material properties.
- Chapter 5 concludes the thesis with a summary and a discussion inferred from the results.

1.4 List of Publications

The following publication resulted from the dissertation.

- Pathak, P., Arora, N. and Rudykh, S. (2022). Magnetoelastic instabilities in soft laminates with ferromagnetic hyperelastic phases. International Journal of Mechanical Sciences, 213, 106862.

Chapter 2

Theoretical background

In this section, we will go through some fundamental theories of elasticity and magnetism necessary for understanding MAEs (Holzapfel, 2001).

2.1 Kinematics

Consider material points in a continuous deformable body, occupying a stress-free region (configuration), residing in three-dimensional Euclidean point space ($\mathbf{R}^3$) with the material particles labeled by their position vectors.

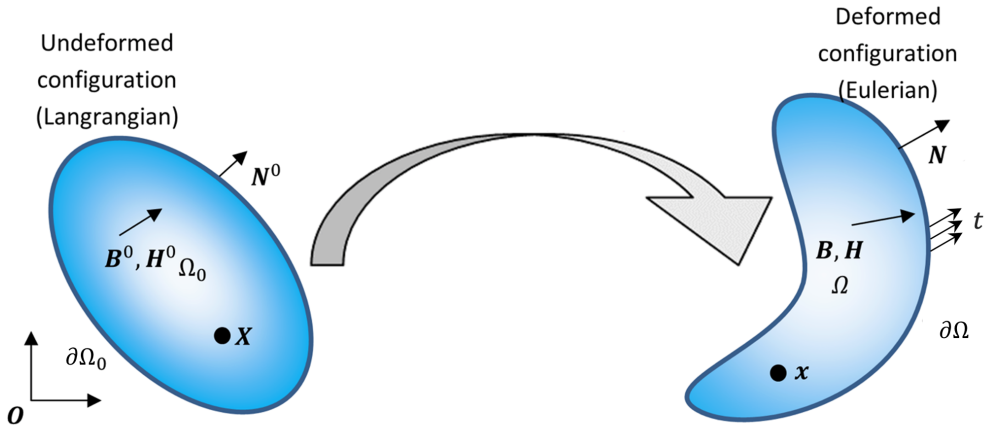

Figure 2.1: Transformation from undeformed (Lagrangian) to deformed (Euler) configuration describing applied traction $\mathbf{t}$, magnetic field and intensity $\mathbf{B}$, $\mathbf{H}$ across a region Ω with boundary $\partial\Omega$. The 0 symbol in $\mathbf{B}^0$, $\mathbf{H}^0$, $\partial\Omega_0$ and Ω_0 denotes corresponding fields in the undeformed configuration.

We consider a magneto-elastic deformable solid with a transformation from undeformed

that occupies a region $\Omega_0 \to \Omega$ with a boundary $\partial\Omega_0 \to \partial\Omega$ of outward normal $\partial N_{\mathbf{0}} \to \partial\mathbf{N}$ in the reference (and current) configuration, where $(\to)$ denotes a transformation from undeformed configuration to a deformed configuration. Ω_0 and $\Omega \subset \mathbf{R}^3$ region are undeformed and deformed configurations, respectively. The Cartesian position vector of a material point in the reference configuration of a body is $\boldsymbol{X}$, and its position vector in the deformed configuration is $\boldsymbol{x}$. The deformation is described by the function χ that maps the reference point $\boldsymbol{x}$ in Ω_0 to its deformed position $\boldsymbol{x} = \chi(\mathbf{X})$ in Ω. We introduce a mapping vector function χ such that

$$\boldsymbol{x} = \chi(\boldsymbol{X}) \tag{2.1}$$

Under the action of a combination of mechanical loading and magnetic field, the body deforms into the current configuration Ω, where deformation gradient $\mathbf{F}$ is defined such that

$$F = \frac{\partial \boldsymbol{x}}{\partial \boldsymbol{X}} \tag{2.2}$$

a Jacobian $J > 0$ is then defined as

$$J = \det \mathbf{F} \tag{2.3}$$

and $\mathbf{C}$ is the right Cauchy-Green strain tensor is defined as

$$\mathbf{C} = \mathbf{F}^T\mathbf{F} \tag{2.4}$$

2.2 Eulerian formulation

This work considers quasi-static deformation in the absence of an electric field, electrical charges, or electrical currents within the material.

2.2.1 Eulerian governing relations

Let $\mathbf{B}$ and $\mathbf{H}$ be the magnetic induction and magnetic intensity in the Eulerian reference frame. Let $\boldsymbol{\sigma}$ be the Cauchy stress. Assuming the absence of body forces, the magnetic induction $\mathbf{B}$ and magnetic intensity $\mathbf{H}$ (in the current configuration) satisfy the following field equations.

$$\operatorname{div} \mathbf{B} = 0, \quad \operatorname{curl} \mathbf{H} = \mathbf{0}, \quad \operatorname{div} \boldsymbol{\sigma} = \mathbf{0} \tag{2.5}$$

where the div and curl are the differential operators defined with respect to x. In the standard Nabla notation, Eq. (2.5) can be rewritten as

$$\nabla\cdot \mathbf{B} = 0, \quad \nabla\times \mathbf{H} = \mathbf{0}, \quad \nabla\cdot \boldsymbol{\sigma} = \mathbf{0} \tag{2.6}$$

2.2.2 Eulerian boundary conditions

Moreover, in heterogeneous bodies such as laminates, many phases of different materials differ in magnetic and elastic properties. The boundaries between the phases can be considered to be interfaces. The magnetic fields have to satisfy the jump conditions across the interface. Consequently, for a given phase, the Maxwell equations and boundary conditions at $\partial\Omega$ take the form.

$$\mathbf{N}\cdot[\![\mathbf{B}]\!]=0,\quad \mathbf{N}\times[\![\mathbf{H}]\!]=\mathbf{0},\quad [\![\boldsymbol{\sigma}]\!]\mathbf{N}=\mathbf{0} \tag{2.7}$$

where $\mathbf{N}=\mathbf{F}^T\mathbf{N}^0$ and $\mathbf{N}^0$ denote the normals to the interface in the current and reference configurations, respectively. The jump operator $[\![\bullet]\!]\equiv(\bullet)^+-(\bullet)^-$ is defined such that $\mathbf{N}$ and $\mathbf{N}^0$ are pointing towards phase $(\bullet)^-$.

2.2.3 Eulerian to Lagrangian transformations

Let $\mathbf{H}^0$ be the magnetic intensity and $\mathbf{B}^0$ be magnetic induction in the Lagrangian reference configuration. To transform the magnetic induction, magnetic intensity, and stress between Euler and Lagrangian fields, we use the following relations.

$$\mathbf{H}^0=\mathbf{F}^T\mathbf{H},\quad \mathbf{B}^0=J\mathbf{F}^{-1}\mathbf{B},\quad \mathbf{P}=J\mathbf{F}^{-T}\boldsymbol{\sigma} \tag{2.8}$$

Here transformation between Cauchy stress ($\boldsymbol{\sigma}$) and the first Piola-Kirchhoff stress tensor ($\mathbf{P}$) is given. The inverse transformations from Lagrangian to Eulerian are as follows.

$$\mathbf{H}=\mathbf{F}^{-\mathbf{T}}\mathbf{H}^0,\quad \mathbf{B}=J^{-1}\mathbf{F}\mathbf{B}^0,\quad \boldsymbol{\sigma}=J^{-1}\mathbf{F}^T\mathbf{P} \tag{2.9}$$

2.3 Lagrangian formulation

2.3.1 Lagrangian governing relations

In the Lagrangian form, Eq. (2.5) can be written as (Dorfmann and Ogden, 2004a)

$$\operatorname{Div}\mathbf{B}^0=0,\quad \operatorname{Curl}\mathbf{H}^0=\mathbf{0},\quad \operatorname{Div}\mathbf{P}=\mathbf{0} \tag{2.10}$$

where the Div and Curl operators are defined with respect to $\mathbf{X}$

2.3.2 Lagrangian boundary conditions

Moreover, for a heterogeneous infinite body, the boundary conditions across interfaces separating different phases at $\partial\Omega^0$ take the form.

$$[\![\mathbf{B}^0]\!]\cdot\mathbf{N}^0=0,\quad [\![\mathbf{H}^0]\!]\times\mathbf{N}^0=\mathbf{0},\quad [\![\mathbf{P}]\!]\cdot\mathbf{N}^0=\mathbf{0}, \tag{2.11}$$

2.4 Stress, magnetism and energy relations

2.4.1 Magnetism relations

Magnetization is customarily defined as

$$\mathbf{M} = \frac{\mathbf{B}}{\mu_0} - \mathbf{H} \tag{2.12}$$

where μ_0 is the vacuum magnetic permeability. Following the works of Brown (1966), Coleman and Noll (1974), Kovetz (2000), the magnetization is constitutively defined in terms of free-energy function $\phi(\mathbf{F}, \mathbf{B})$ as

$$\mathbf{M} = -\rho \frac{\partial \phi}{\partial \mathbf{B}}, \tag{2.13}$$

ϕ is the magnetic energy density function and ρ is the material density in the current configuration.

2.4.2 Stress relations

Consequently, stress equations due to magnetization $\boldsymbol{M}$ take the form (Zhang and Rudykh, 2022)

$$\boldsymbol{\sigma} = \rho \frac{\partial \phi}{\partial \mathbf{F}} \mathbf{F}^T + (\mathbf{M} \cdot \mathbf{B})\mathbf{I} - \mathbf{M} \otimes \mathbf{B} + \boldsymbol{\sigma_m} \tag{2.14}$$

where $\boldsymbol{\sigma}_m$ which is given by

$$\boldsymbol{\sigma_m} = \frac{1}{\mu_0} \left(\mathbf{B} \otimes \mathbf{B} - \frac{\mathbf{B} \cdot \mathbf{B}}{2} \mathbf{I} \right) \tag{2.15}$$

The corresponding stress tensor $\boldsymbol{\sigma}_m$ is also called Maxwell stress. Note that in the absence of material (or vacuum), the stress tensor Eq. (2.15) is still non-zero and depends on the magnetic field.

2.4.3 Energy relations

In terms of these relations, the energy-density function ϕ fully characterizes the behavior of magneto-active elastomers. The free energy in Lagrangian form is defined as $\Phi(\mathbf{F}, \mathbf{B}^0) = \phi(\mathbf{F}, J^{-1}\mathbf{F}\mathbf{B}^0)$. In terms of Φ, a Lagrangian *amended* energy function can be constructed as follows (Dorfmann and Ogden, 2004a). For a conservative material whose response is described by a free-energy density function $\Psi\left(\boldsymbol{F}, \boldsymbol{B}^0\right)$.

$$\Psi(\mathbf{F}, \mathbf{B}^0) = \rho_0 \Phi(\mathbf{F}, \mathbf{B}^0) + \frac{\mathbf{F}\mathbf{B}^0 \cdot \mathbf{F}\mathbf{B}^0}{2\mu_0 J}, \tag{2.16}$$

where $\rho_0 = \rho J$ is the material density in the reference configuration. Ψ, which is expressed as a function of the deformation gradient tensor $\boldsymbol{F}$ and magnetic induction vector $\boldsymbol{B}$, obeys the following constitutive equations.

$$\boldsymbol{P} = \frac{\partial \Psi\left(\boldsymbol{F}, \boldsymbol{B}^0\right)}{\partial \boldsymbol{F}} \text{ and } \boldsymbol{H}^0 = \frac{\partial \Psi\left(\boldsymbol{F}, \boldsymbol{B}^0\right)}{\partial \boldsymbol{B}^0} \tag{2.17}$$

For incompressible materials ($J = 1$) (2.17) transforms into

$$\boldsymbol{P} = \frac{\partial \Psi\left(\boldsymbol{F}, \boldsymbol{B}^0\right)}{\partial \boldsymbol{F}} - p\boldsymbol{F}^{-T} \tag{2.18}$$

where $\boldsymbol{P}$ is the total first Piola-Kirchhoff stress tensor, p is the Lagrange multiplier associated with the incompressibility constraint, and the corresponding total Cauchy stress tensor is

$$\boldsymbol{\sigma} = \frac{\partial W(\mathbf{F}, \mathbf{B}^0)}{\partial \mathbf{F}}\mathbf{F}^T - p\mathbf{I}, \tag{2.19}$$

In terms of $\boldsymbol{H}$, the relationship can be rewritten as follows (Goshkoderia and Rudykh, 2017)

$$\boldsymbol{P} = \frac{\partial \Psi\left(\boldsymbol{F}, \boldsymbol{H}^0\right)}{\partial \boldsymbol{F}} \text{ and } \boldsymbol{B}^0 = -\frac{\partial \Psi\left(\boldsymbol{F}, \boldsymbol{H}^0\right)}{\partial \boldsymbol{H}^0} \tag{2.20}$$

For incompressible materials ($J = 1$) (2.20) transforms into

$$\boldsymbol{P} = \frac{\partial \Psi\left(\boldsymbol{F}, \boldsymbol{H}^0\right)}{\partial \boldsymbol{F}} - p\boldsymbol{F}^{-T} \tag{2.21}$$

2.4.4 Traction boundary conditions

It can be shown (see Galipeau, 2012; Kankanala and Triantafyllidis, 2004) that the traction on the boundary of the specimen can be expressed in the form

$$\mathbf{t} = \left[\mathbf{T} + \frac{\mu_0}{2}(\mathbf{H}\cdot\mathbf{H})\mathbf{I} - \mathbf{B}\otimes\mathbf{B}\right]\mathbf{n} - \frac{\mu_0}{2}(\mathbf{M}\cdot\mathbf{n})^2\mathbf{n} \tag{2.22}$$

where $\boldsymbol{H}$, $\boldsymbol{B}$ and $\boldsymbol{M}$ are just inside the boundary, and $\boldsymbol{n}$ is the outward normal to the boundary of the material surface and $\boldsymbol{t}$ is the traction outside the material. Let us consider a 2D square with two adjacent surfaces, A and B (as shown in Fig. 2.2), oriented along the $\mathbf{e}_1$ and $\mathbf{e}_2$ directions, respectively. Stress inside the materials are $\boldsymbol{\sigma}_A$ and $\boldsymbol{\sigma}_B$. The externally applied traction on these surfaces is $\mathbf{t_A}$ and $\mathbf{t_B}$. A magnetic field $\mathbf{B} = B\mathbf{e}_2$ is applied. We are assuming surfaces 1 and 2 are free surfaces; therefore, externally applied traction ($\mathbf{t}_A$ and $\mathbf{t}_B$) are zero on the outer surfaces.

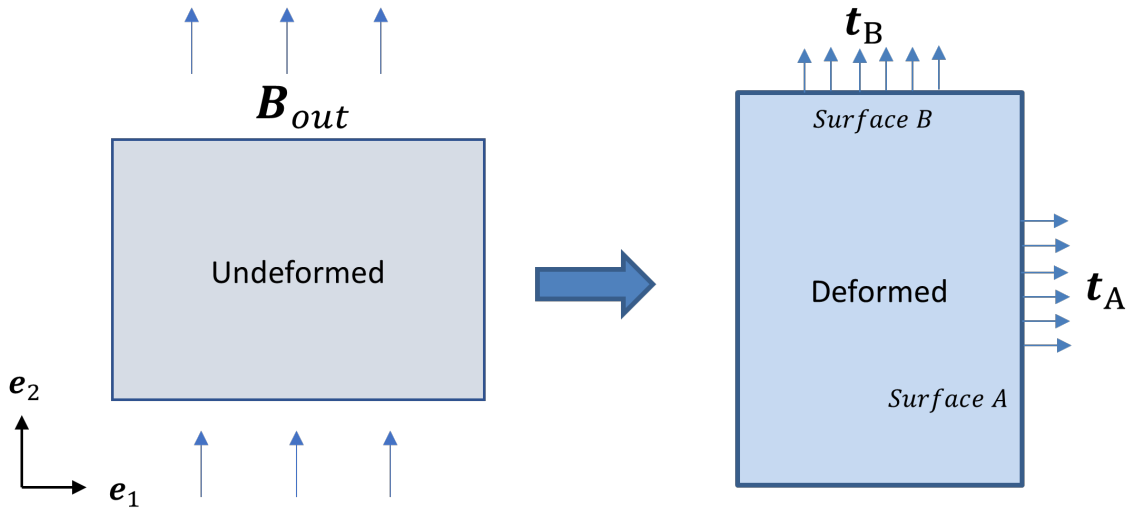

Figure 2.2: Surface traction and Maxwell stress in the elastomer placed in an externally applied magnetic field

For surface A, considering stress and traction components along $\mathbf{e_1}$ direction, we get the following result

$$\begin{aligned} t_1 &= \sigma_{11} + \frac{\mu_0 H^2}{2} = 0 \\ \sigma_{11} &= -\frac{\mu_0 H^2}{2} \end{aligned} \tag{2.23}$$

For surface B, considering stress and traction components along $\mathbf{e_2}$ direction, we get the following result

$$\begin{aligned} t_2 &= \sigma_{22} - \frac{B^2}{2\mu_0} = 0 \\ \sigma_{22} &= \frac{B^2}{2\mu_0} \end{aligned} \tag{2.24}$$

Here σ_{11} and σ_{22} become the Maxwell stress inside the material in the calculation of the traction as measured on the surface of the material. The pressure term is derived using the traction boundary conditions (2.22) along with the energy relations of Cauchy stress. The corresponding Cauchy stress σ_{22} equals Maxwell stress (2.24) in that direction. We then combine the traction boundary condition (2.24) and incompressible total Cauchy stress (2.19) to the expression for the Lagrange multiplier in (2.25)

$$p = \left[\frac{\partial W(\mathbf{F}, \mathbf{B}^0)}{\partial \mathbf{F}} \mathbf{F}^T \right]_{22} - \sigma_{22}, \tag{2.25}$$

To calculate the $\frac{\partial W(\mathbf{F},\mathbf{B}^0)}{\partial \mathbf{F}}\mathbf{F}^T$ term, the deformation gradient and the material model are used as inputs at the boundary and taking σ_{22} from (2.24), we can get the equation of the Lagrange multiplier.

2.5 Incremental analysis

The mechanics of incremental deformations superimposed upon a given state of finite initial deformation allow the investigation of instabilities that develop in MAEs subjected to magnetic fields. For further reading, refer to the works of Goshkoderia and Rudykh (2017), Ottenio et al. (2008), Rudykh and Bertoldi (2013), Wu and Destrade (2021), Dorfmann and Haughton (2006).

2.5.1 Lagrangian incremental formulation

Lagrangian incremental governing relations

Following the approach recently developed to investigate instabilities in magnetoactive composites (Dorfmann and Ogden, 2004b; Bertoldi and Gei, 2011; Rudykh and deBotton, 2011), we derive the governing equations for the incremental deformations superimposed upon a given state of finite deformation in the presence of a magnetic field. We derive the incremental Lagrangian equation from the Lagrangian governing equations (2.5).

$$\text{Div}\,\dot{\mathbf{B}}^0 = 0, \qquad \text{Curl}\,\dot{\mathbf{H}}^0 = \mathbf{0}, \qquad \text{Div}\,\dot{\mathbf{P}} = \mathbf{0} \tag{2.26}$$

where $\dot{\mathbf{P}}$, $\dot{\mathbf{B}}^0$, and $\dot{\mathbf{H}}^0$ are the incremental changes in $\mathbf{P}$, $\mathbf{B}^0$, and $\mathbf{H}^0$, respectively.

Lagrangian incremental constitutive relation

Assuming that all incremental quantities are sufficiently small, the relations (2.17) can be linearized as follows. The linearized expressions for the incremental changes in the linearized constitutive relations can be expressed using the Einstein summation notation. In the first Piola-Kirchhoff stress tensor and magnetic induction are given as

$$\begin{aligned} \dot{P}_{ij} &= \mathcal{A}^0_{ijkl}\dot{F}_{kl} + \mathcal{M}^0_{ijk}\dot{B}^0_k, \\ \dot{H}^0_i &= \mathcal{M}^0_{jki}\dot{F}_{jk} + \mathcal{H}^0_{ij}\dot{B}^0_j, \end{aligned} \tag{2.27}$$

For an incompressible material, Eq. $(2.27)_1$ modifies to

$$\dot{P}_{ij} = \mathcal{A}^0_{ijkl}\dot{F}_{kl} + \mathcal{M}^0_{ijk}\dot{B}^0_k + (pF^{-1}_{jk}\dot{F}_{kl}F^{-1}_{li} - \dot{p}F^{-1}_{ji}), \tag{2.28}$$

where $\dot{p}$ is the incremental change in p.

Lagrangian incremental constitutive tensors

The magneto-elastic moduli tensors are derived as follows

$$\mathcal{A}^0_{ijkl} = \frac{\partial^2 W}{\partial F_{ij} \partial F_{kl}}, \quad \mathcal{M}^0_{ijk} = \frac{\partial^2 W}{\partial F_{ij} \partial B^0_k}, \quad \mathcal{H}^0_{ij} = \frac{\partial^2 W}{\partial B^0_i \partial B^0_j} \tag{2.29}$$

Lagrangian to Eulerian incremental transformations

The push forward transformations (denoted by $\dot{\mathbf{H}} \to \dot{\mathbf{H}}^0, \dot{\mathbf{B}} \to \dot{\mathbf{B}}^0$) and $\dot{\boldsymbol{\sigma}} \to \dot{\mathbf{P}}$ to the current configuration are

$$\dot{\mathbf{H}} = \mathbf{F}^{-T} \dot{\mathbf{H}}^0, \quad \dot{\mathbf{B}} = J^{-1} \mathbf{F} \dot{\mathbf{B}}^0, \quad \dot{\boldsymbol{\sigma}} = J^{-1} \mathbf{F}^T \dot{\mathbf{P}} \tag{2.30}$$

In the current configuration, the magneto-elastic moduli are transformed as

$$\begin{aligned} \mathcal{A}_{ijkl} &= J^{-1} F_{j\alpha} F_{l\beta} \mathcal{A}^0_{i\alpha k\beta} \\ \mathcal{M}_{ijk} &= F_{j\alpha} F^{-1}_{\beta k} \mathcal{M}^0_{i\alpha\beta} \\ \mathcal{H}_{ij} &= J F^{-1}_{\alpha i} F^{-1}_{\beta j} \mathcal{H}^0_{\alpha\beta} \end{aligned} \tag{2.31}$$

and they possess the following symmetries

$$\mathcal{A}_{ijkl} = \mathcal{A}_{klij}, \quad \mathcal{M}_{ijk} = \mathcal{M}_{jik}, \quad \text{and} \quad \mathcal{H}_{ij} = \mathcal{H}_{ji}. \tag{2.32}$$

2.5.2 Eulerian incremental formulation

For further analysis of instabilities, it is convenient to reformulate the incremental boundary value problem in an Eulerian formulation, where the reference configuration moves and is identified with the current configuration.

Eulerian incremental governing relations

Substituting the above equation yields the standard governing relations, similar to non-incremental governing relations. The updated incremental governing equations take the form

$$\operatorname{div} \dot{\boldsymbol{\sigma}} = \mathbf{0} \quad , \quad \operatorname{curl} \dot{\mathbf{H}} = \mathbf{0}, \quad \operatorname{div} \dot{\mathbf{B}} = 0 \tag{2.33}$$

where $\dot{\boldsymbol{\sigma}}$, $\dot{\mathbf{B}}$, and $\dot{\mathbf{H}}$ are the 'push-forward' counterparts of $\dot{\mathbf{P}}$, $\dot{\mathbf{B}}^0$, and $\dot{\mathbf{H}}^0$, respectively.

Eulerian incremental constitutive relations

Substituting the transformations Eqs. (2.31) and (2.30) to the constitutive relations Eqs. $(2.27)_2$ and (2.28), we obtain

$$\begin{aligned}\dot{\sigma}_{ij} &= \mathcal{A}_{ijkl}\frac{\partial v_k}{\partial x_l} + \mathcal{M}_{ijk}\dot{B}_k - \dot{p}\delta_{ij} + p\frac{\partial v_j}{\partial x_i} \\ \dot{H}_i &= \mathcal{M}_{jki}\frac{\partial v_j}{\partial x_k} + \mathcal{H}_{ij}\dot{B}_j\end{aligned} \tag{2.34}$$

where $\boldsymbol{v}$ is the velocity field in the current configuration and δ_{ij} is the Kronecker delta given as

$$\delta_{ij} = \begin{cases} 1 & \forall \ i = j \\ 0 & \forall \ i \neq j \end{cases} \tag{2.35}$$

Here we have used the following expressions for the incremental deformation gradient and incremental displacements (Goshkoderia and Rudykh, 2017)

$$\begin{aligned}\dot{\mathbf{F}} &= \frac{\partial \boldsymbol{v}}{\partial \boldsymbol{X}} = \frac{\partial \boldsymbol{v}}{\partial \boldsymbol{x}}\frac{\partial \boldsymbol{x}}{\partial \boldsymbol{X}} = \nabla \boldsymbol{v}\mathbf{F} \\ \dot{\boldsymbol{x}} &= \boldsymbol{v}\end{aligned} \tag{2.36}$$

where $\dot{\mathbf{F}}$ is the incremental deformation gradient.

Eulerian incremental field equations for velocity and magnetic field

Upon substitution of Eqs. (2.34) into Eqs. $(2.33)_1$ and $(2.33)_2$, we obtain the Eulerian tensor moduli field equations

$$\begin{aligned}\mathcal{A}_{ijkl}\frac{\partial^2 v_k}{\partial x_j \partial x_l} + \mathcal{M}_{ijk}\frac{\partial \dot{B}_k}{\partial x_j} - \frac{\partial \dot{p}}{\partial x_i} &= 0 \\ \epsilon_{spi}\left(\mathcal{M}_{jki}\frac{\partial^2 v_j}{\partial x_k \partial x_p} + \mathcal{H}_{ij}\frac{\partial \dot{B}_j}{\partial x_p}\right) &= 0\end{aligned} \tag{2.37}$$

where ϵ_{spi} is the Levi-Civita permutation tensor.

2.6 Background of linear and non-linear magnetism

In this section, we cover some theoretical background of magnetism and the constitutive laws used to predict the behavior of MAEs.

2.6.1 Permeability

The magnetic permeability constant μ is defined as the ratio between the magnetic flux density $\boldsymbol{B}$ within a material, and the intensity of an applied magnetic field $\boldsymbol{H}$

$$\mathbf{B} = \mu\mathbf{H}, \tag{2.38}$$

where μ is the magnetic permeability. Let $\mu_r = \mu/\mu_0$ be the relative permeability of the material. Based on the value of the relative permeability, magnetic materials can be roughly classified into diamagnetic ($\mu_r < 1$), paramagnetic ($1 < \mu_r < 5$), and ferromagnetic ($\mu_r > 5$) (See Fig. 2.3).

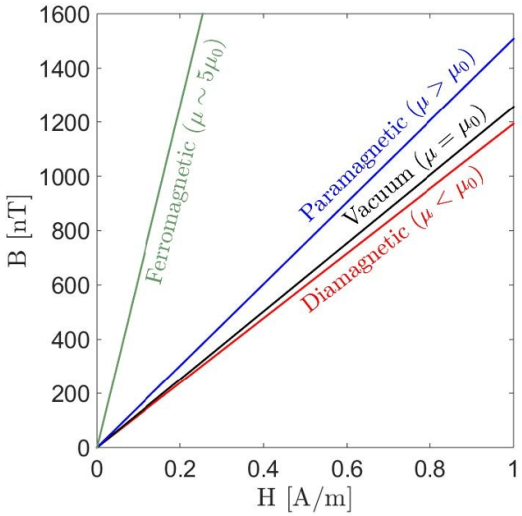

Figure 2.3: Comparison of the permeability of various permeable materials (Developers, 2017)

2.6.2 Initial susceptibility

The relation between magnetic field $\mathbf{B}$ and magnetization $\mathbf{M}$ (defined in Eq. (2.12)) is initially linear with slope χ as the initial susceptibility.

$$\mu_0\mathbf{M} = \mathbf{B}\chi \tag{2.39}$$

where χ is the initial susceptibility. The relation between magnetic intensity and the magnetic field is initially linear with a constant initial slope $(1 - \chi)$

$$\mu_0\mathbf{H} = \mathbf{B}(1 - \chi) \tag{2.40}$$

Here the conversion between μ_r and χ is

$$\chi = \frac{\mu_r - 1}{\mu_r} \quad \text{and} \quad \mu_r = \frac{1}{1-\chi} \tag{2.41}$$

The paramagnetic and ferromagnetic materials all have $\chi > 0$. The ferromagnetic materials show large magnetic susceptibility of $\chi = 0.9$–0.99. Diamagnetic materials have $\chi < 0$. A typical value of χ at room temperature is in the order of $\chi = -10^{-5}$ for diamagnetic materials. The lowest limit of χ for a diamagnetic material is a superconductor with $\chi_H = -1$ [1].

2.6.3 Magnetization

Magnetization $\mathbf{M}$ for paramagnetic materials is parallel to the applied field $\mathbf{H}$ and increases by applying a magnetic field. Magnetization of diamagnetic is weak and opposes the applied magnetic field. Thus magnetic flux density reduces within a magnetic field. Ferromagnetic materials exhibit strong magnetism in the same direction as the field. These materials are either soft or hard depending on hysteresis, and they can be easily magnetized and demagnetized.

2.6.4 Superparamagnetism

Superparamagnetic substances are magnetic nanoparticles (refer Fig. 2.4), with a size ranging from a few nanometers to a couple of tenths of nanometers (usually 3 to 50 nm). At this size, depending on the type of materials, the materials transition from ferromagnetic to paramagnetic (Bhattacharya, 2021). They behave like a giant paramagnetic with fast responses to applied magnetic fields, negligible remanence (residual magnetism), and coercivity.

[1] In this work, we use the magnetic susceptibility, χ, defined via magnetic induction as $\mu_0\mathbf{M} = \chi\mathbf{B}$. Note the alternative definition of magnetic susceptibility in terms of magnetic intensity is $\mathbf{M} = \chi_H\mathbf{H}$. These susceptibilities are related as $\chi_H = \chi/(1-\chi)$ or $\chi = \chi_H/(\chi_H + 1)$.

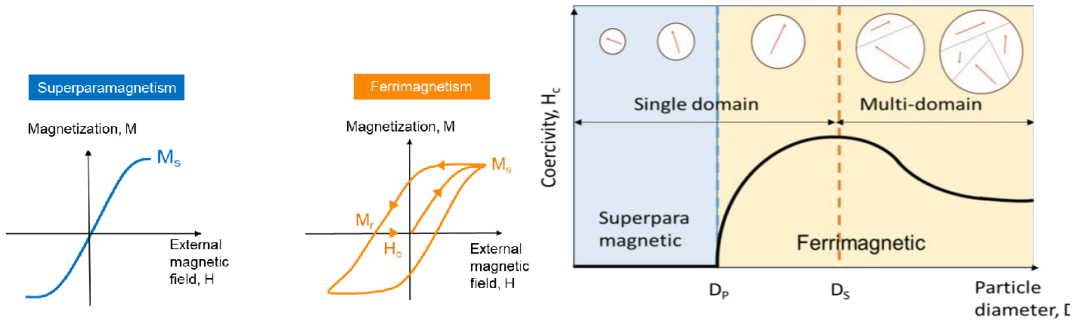

(a) (b)

Figure 2.4: (a)Differences between superparamagnetic and ferromagnetic are highlighted using a schematic (b) Effect of nanoparticle size on coercivity (Koo et al., 2019)

The differences between paramagnetic and superparamagnetic materials are highlighted in Fig. 2.5. We can see a higher magnetization for the same magnetic field level. By definition of a superparamagnetic material, the hysteresis effects are also negligible in a superparamagnetic material as compared to ferromagnetic (as can be seen from the hysteresis curves in Fig. 2.5 (a),(b). (Koo et al., 2019; Naseer et al., 2014; Bertotti, 1998)

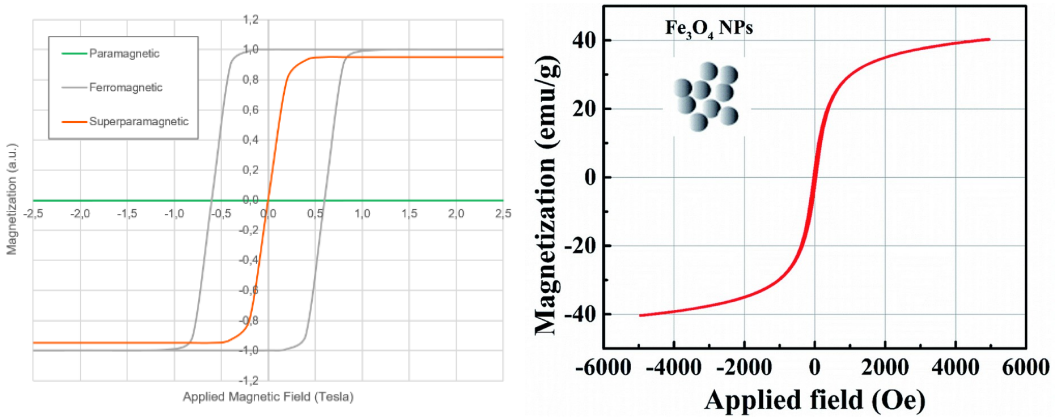

(a) (b)

Figure 2.5: (a)Schematic of Hysteresis curves for paramagnetic, ferromagnetic and superparamagnetic (Martínez, 2018) (b) Hysteresis loop of Fe_2O_3 nanoparticles at room temperature (Nguyen et al., 2020; Moskvin et al., 2020)

2.7 Theory of non-linear elasticity

The theory of elasticity is covered in detail in the books by (Truesdell and Noll, 1965; Wang and Truesdell, 1973; Ogden, 1997; Holzapfel, 2001)

2.7.1 Hyperelastic materials

Hyperelastic materials are materials whose models are described by a strain-energy function. The strain-energy function is a scalar-valued energy function of the deformation gradient **F**. In the purely mechanical isotropic material, the deformation gradient can be adequately described using three invariants (I_1,I_2, and I_3). Hence only three parameters are needed to describe the energy-density function (Holzapfel, 2001).

$$\psi(F) = \psi(I_1, I_2, I_3) \tag{2.42}$$

where ψ is the scalar-valued energy density function, **F** is the deformation gradient and I_1, I_2 and I_3 are the three invariants of deformation gradient **F**. Where invariants,

$$I_1 = \operatorname{Tr} \mathbf{C}, \quad I_2 = \frac{1}{2}\left(I_1^2 - \operatorname{Tr} \mathbf{C}^2\right), \quad I_3 = \det \mathbf{C} \tag{2.43}$$

Hyperelastic material models are primarily designed for modeling rubber or rubber-like materials that have large deformations. They can have a high degree of non-linearity in their stress-strain response. There are many strain-energy models for materials. Some examples are the neo-Hookean model (Rivlin, 1949), Mooney–Rivlin model (Rivlin, 1949; Mooney, 1940b; Mooney, 1940a; Ogden, 1992) and polynomial models, etc. Mooney-Rivlin model is well-known to model rubber-like materials within moderate strain regions.

2.7.2 Neo-Hookean model

The neo-Hookean model is a special case of the Mooney-Rivlin model, which is described by the following relation,

$$\psi(I_1) = \frac{G}{2}(\mathbf{F} : \mathbf{F} - 3) = \frac{G}{2}(I_1 - 3) \tag{2.44}$$

2.8 Magnetoelastic energy models

Elastomeric models are then combined with magnetic models to create a Magnetoelastic model of materials. In this work, we assume the magnetoactive elastomers to be magnetically soft, so the hysteresis effects can be neglected. Moreover, we consider the magnetic particles to be isotropic and superparamagnetic, i.e., demagnetization effects are neglected.

2.8.1 Linear magnetic model

The relation between the magnetic field and the magnetic intensity affects the overall stability of the composite. This relationship depends on the energy model used, as well as

the initial susceptibility and saturation value. The corresponding magnetic energy is

$$\rho\phi_m(\mathbf{B}) = -\frac{1}{2\mu_0}\mathbf{B}\cdot\chi\mathbf{B}. \tag{2.45}$$

The constitutive relationship is defined by a hyperelastic solid model. In general, the energy density function Ψ for an isotropic function is a function of six invariants

$$\Psi\left(\mathbf{F},\mathbf{B}^0\right) = \Psi\left(I_1, I_2, I_3, I_4, I_5, I_6\right) \tag{2.46}$$

In the special case of the linear magnetic energy model, the expression is

$$\Psi\left(\mathbf{F},\mathbf{B}^0\right) = \frac{G}{2}\left(I_1 - 3\right) + \frac{I_5}{2\mu J} \tag{2.47}$$

where the invariant I_5

$$I_5 = \mathbf{F}\mathbf{B^0}\cdot\mathbf{F}\mathbf{B^0} \tag{2.48}$$

$\mathbf{C}$ is the right Cauchy-Green strain tensor, $\mathbf{B^0}$ is the Lagrangian magnetic field in the reference configuration, $\mathbf{H^0}$ is the Lagrangian magnetic intensity in the reference configuration. In terms of the current configuration, (2.47) can also be written as

$$\Psi(\mathbf{F},\mathbf{B}) = \frac{G}{2}\left(I_1 - 3\right) + \frac{J}{2\mu}\mathbf{B}\cdot\mathbf{B} \tag{2.49}$$

where $\mathbf{B}$ is the magnetic field in the current configuration.

2.8.2 Ferromagnetic material model

For ferromagnetic materials, the magnetization reaches a saturation state at sufficiently high magnetic fields, beyond which there is no further increase in magnetization. Assuming the soft ferromagnetic behavior and magnetic particles are large compared to the typical domain size, the material behavior can be idealized as having a single-valued constitutive behavior. Although other models can be used, we use the isotropic Langevin model to define the ferromagnetic behavior in the forthcoming analysis. For this model, magnetization is defined by the following relation.

The relation between magnetic intensity and magnetization is nonlinear, with initial slope χ as the initial susceptibility and in the direction of the magnetic field. The magnetization asymptotically reaches a saturation value of m_s.

$$\mathbf{M}(\mathbf{B}) = -\rho\frac{\partial\Phi}{\partial\mathbf{B}} = m_s\frac{\mathbf{B}}{|\mathbf{B}|}\left[\coth\left(\frac{3\chi|\mathbf{B}|}{\mu_0 m_s}\right) - \left(\frac{3\chi|\mathbf{B}|}{\mu_0 m_s}\right)^{-1}\right] \tag{2.50}$$

where m_s is the saturation magnetization and B is the magnitude of the magnetic induction vector $\mathbf{B}$, i.e., $B = |\mathbf{B}|$. Using the identity for magnetic field $\mu_0\mathbf{M} + \mu_0\mathbf{H} = \mathbf{B}$. we derive

the equation for magnetic intensity $\mathbf{H}$ by subtracting the magnetization from the magnetic field. Alternatively, the constitutive relation can also be expressed as

$$\mathbf{B} = \mu(\mathbf{B})\mathbf{H} \tag{2.51}$$

where

$$\mu(\mathbf{B}) = \mu_0\left(1 - \frac{\mu_0 m_s}{|\mathbf{B}|}\left[\coth\left(\frac{3\chi|\mathbf{B}|}{\mu_0 m_s}\right) - \frac{\mu_0 m_s}{3\chi|\mathbf{B}|}\right]\right)^{-1} \tag{2.52}$$

The corresponding magnetic energy is

$$\rho\phi_m(\mathbf{B}) = -\frac{\mu_0 m_s^2}{3\chi}\left[\ln\left(\sinh\left[\frac{3\chi|\mathbf{B}|}{\mu_0 m_s}\right]\right) - \ln\left(\frac{3\chi|\mathbf{B}|}{\mu_0 m_s}\right)\right] \tag{2.53}$$

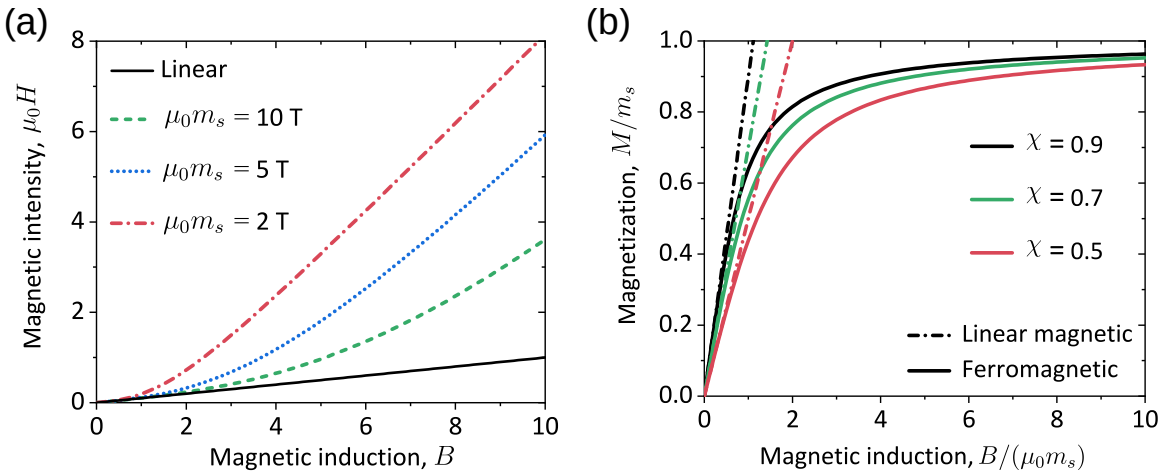

Figure 2.6: The dependence of magnetic intensity magnitude H (a) and magnetization M (b) on the magnetic induction magnitude B; initial susceptibility is $\chi = 0.9$ in (a).

Fig. 2.6a illustrates the magnetic $B - H$ dependence for linear and ferromagnetic materials. Here, we plot the magnitude of magnetic intensity H as the function of B for materials with initial susceptibility $\chi = 0.9$. The dashed curves represent the behavior of the linear magnetic material, while the solid curves show the corresponding response of ferromagnetic materials with magnetic saturation values: $\mu_0 m_s = 2$ T (red dash-dotted curve), $\mu_0 m_s = 5$ T (blue dotted curve), and $\mu_0 m_s = 10$ T (green dashed curve). As expected, the $B - H$ curve for linear magnetic material shows a linear response. However, for ferromagnetic materials, the dependence is nonlinear, specifically in small magnetic fields. However, once the saturation limit of magnetization is achieved at a relatively high magnetic field, they show the linear relation in H and B.

Fig. 2.6b shows the normalized magnitude of magnetization M/m_s as the function of normalized magnetic induction $B/(\mu_0 m_s)$. The solid curves represent the response

of the ferromagnetic materials, whereas the dash-dotted curves correspond to the linear magnetic materials. We consider the materials with three initial susceptibilities: $\chi = 0.9$ (black curves), $\chi = 0.7$ (green curves), and $\chi = 0.5$ (red curves). As expected, the linear magnetic materials show the linear dependence of magnetization on magnetic induction, with slopes proportional to their corresponding magnetic susceptibilities χ. Ferromagnetic materials also show a linear response, however, only at small magnetic fields. At relatively high magnetic induction magnitudes, the magnetization in these materials approaches the saturation values, $M/m_s \to 1$ (see the solid curves). In ferromagnetic materials with higher initial susceptibilities, the saturation magnetization values are achieved at comparatively smaller magnetic induction magnitudes. The corresponding energy has three parts neo-Hookean energy (Ψ_{nH}), magnetic field energy(Ψ_{B}) and energy of magnetization (Ψ_{M}) where

$$\begin{aligned} \Psi_{nH} &= \frac{G}{2}\left(I_1 - 3\right) \\ \Psi_{\mathrm{B}} &= \frac{\left(\mathbf{FB^0}\right)\cdot\left(\mathbf{FB^0}\right)}{2\mu_0 J} \\ \Psi_{\mathrm{M}} &= \rho\Phi(|\mathbf{B}|) \end{aligned} \tag{2.54}$$

and invariant I_1 is defined in (2.43), G is the initial shear modulus, μ_0 is the permeability in a vacuum, $|\mathbf{B}|$ and $|\mathbf{B^0}|$ is the absolute value of the magnetic induction vector in the current configuration and reference configuration respectively, and ρ is a proportionality constant. The total energy of function Ψ is the sum of the material's mechanical and magnetization energy plus the energy due to the magnetic field.

$$\Psi\left(\mathbf{F}, \mathbf{B^0}\right) = \Psi_{nH} + \Psi_{\mathrm{B}} + \Psi_{\mathrm{M}} \tag{2.55}$$

The full expression of the total energy is

$$\Psi\left(\mathbf{F}, \mathbf{B^0}\right) = \frac{G}{2}\left(I_1 - 3\right) + \frac{\left(\mathbf{FB^0}\right)\cdot\left(\mathbf{FB^0}\right)}{2\mu_0 J} + \rho\Phi(|\mathbf{B}|) \tag{2.56}$$

where

$$\rho\Phi(|\mathbf{B}|) = -\frac{\mu_0 m_s^2}{3\chi}\left[\ln\left(\sinh\left(\frac{3\chi|\mathbf{B}|}{\mu_0 m_s}\right)\right) - \ln\left(\frac{3\chi|\mathbf{B}|}{\mu_0 m_s}\right)\right] \tag{2.57}$$

and m_s is the saturation magnetization, χ is the initial susceptibility and $|\mathbf{B}|$ is the absolute value of the magnetic induction vector. Magnetization is defined by the following relation.

$$\mathbf{M}(\mathbf{B}) = -\rho\frac{\partial\Phi}{\partial\mathbf{B}} = m_s\frac{\mathbf{B}}{|\mathbf{B}|}\left[\coth\left(\frac{3\chi|\mathbf{B}|}{\mu_0 m_s}\right) - \left(\frac{3\chi|\mathbf{B}|}{\mu_0 m_s}\right)^{-1}\right] \tag{2.58}$$

Note that Eq. (2.58) implies that magnetization and magnetic field vectors are co-linear. Thus, the interaction of the magnetic field and the magnetic moment does not result in

the appearance of the magnetic torque under this assumption. The magnetic force in the particles, which is proportional to the rate of change of the magnetic field, is non-zero only if the magnetic field is homogeneous.

2.8.3 neo-Hookean energy model with magnetic invariants I_4, I_5 and I_6

We consider adding additional invariants to the magnetic hyperelastic to improve our energy model. Galich and Rudykh (2016) uses these invariants to model dielectric elastomers. Analogously, we use the additional invariants I_4, I_5 and I_6 for modelling MAEs. The constitutive relationship is defined by a hyperelastic solid model. The energy density function Ψ for an isotropic function is a function of six invariants

$$\Psi\left(\mathbf{F}, \mathbf{B}^0\right) = \Psi\left(I_1, I_2, I_3, I_4, I_5, I_6\right) \tag{2.59}$$

$$\Psi\left(\mathbf{F}, \mathbf{B}^0\right) = \frac{G}{2}\left(I_1 - 3\right) + \frac{1}{2\mu_0\mu J}\left(\gamma_0 I_4 + \gamma_1 I_5 + \gamma_2 I_6\right) \tag{2.60}$$

where invariants I_4, I_5 and I_6 are

$$I_4 = \mathbf{B^0}\cdot\mathbf{B^0}, \quad I_5 = \mathbf{FB^0}\cdot\mathbf{FB^0}, \quad I_6 = \mathbf{CB^0}\cdot\mathbf{CB^0} \tag{2.61}$$

and γ_0, γ_1, and γ_2 are the empirically determined proportionality constants. It is important to remember that the additional invariants have no physical analog and their effect on the total material energy is purely empirical. In the special case of an undeformed state, the deformation gradient $\mathbf{F} = \mathbf{I}$ (the 3×3 identity matrix), and since there is only a pure magnetic field, (2.61) becomes $I_4 = I_5 = I_6 = \mathbf{B}^0 \cdot \mathbf{B}^0$. To maintain consistency with the linear magnetic model, the Eq. (2.60) must be equivalent to the standard linear magnetic energy model (2.47). This can only happen if the proportionality constants γ_0, γ_1, and γ_2 sum to unity i.e. (2.60) is consistent with (2.47) for all values of the deformation gradient (F) if and only if

$$\gamma_0 + \gamma_1 + \gamma_2 = 1 \tag{2.62}$$

For the special case of plain strain where the deformation gradient is

$$\mathbf{F} = \lambda\mathbf{e_1}\otimes\mathbf{e_1} + \lambda^{-1}\mathbf{e}_2\otimes\mathbf{e}_2 + \mathbf{e}_3\otimes\mathbf{e}_3 \tag{2.63}$$

the magnetization equations (2.39) reduces to the following

$$\mu_0\mathbf{M} = \mathbf{B}\left(1 - \frac{1}{\mu'}\left(\frac{\gamma_2}{\lambda^2} + \gamma_1 + \gamma_0\lambda^2\right)\right) \tag{2.64}$$

The magnetic intensity equations (2.38) reduces to the following

$$\mu_0\mathbf{H} = \frac{\mathbf{B}}{\mu}\left(\frac{\gamma_2}{\lambda^2} + \gamma_1 + \gamma_0\lambda^2\right) \tag{2.65}$$

Chapter 3

Analysis

3.1 The microstructure of the composite material

We examine incompressible magnetoactive elastomers with bilayered microstructure (schematically shown in Fig. 3.1 having lamination direction $\mathbf{L}$. The constituents have a volume fraction of the matrix phase as $c^{(m)}$, and that of the stiff layer as $c^{(f)} = 1 - c^{(m)}$. Hereafter, we denote the parameters and fields corresponding to the matrix and stiff layers as $(\bullet)^{(m)}$ and $(\bullet)^{(f)}$, respectively. The average deformation gradient $\bar{\mathbf{F}}$ and magnetic induction $\bar{\mathbf{B}}$ are defined as

$$\begin{aligned} \bar{\mathbf{F}} &= c^{(m)}\mathbf{F}^{(m)} + c^{(f)}\mathbf{F}^{(f)} \\ \bar{\mathbf{B}} &= c^{(m)}\mathbf{B}^{(m)} + c^{(f)}\mathbf{B}^{(f)} \end{aligned} \tag{3.1}$$

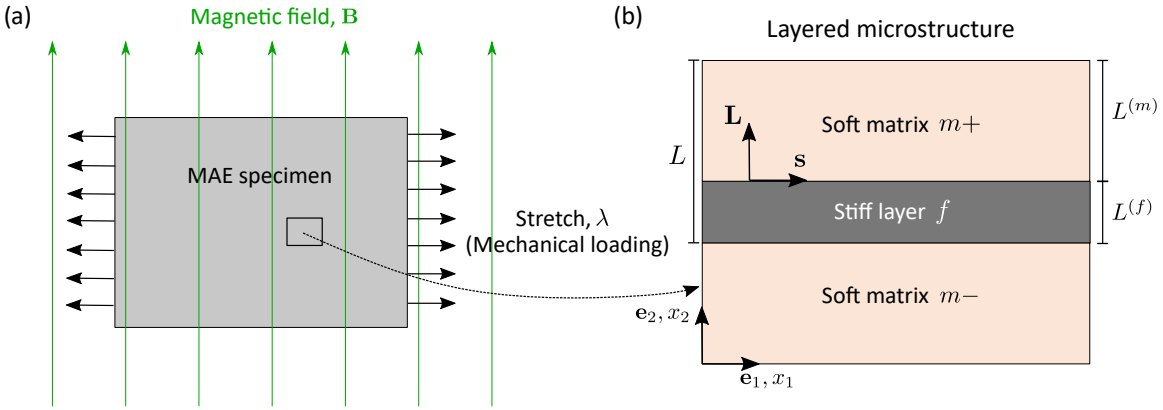

Figure 3.1: Schematic representation of the composite under investigation. Magneto active elastomer (MAE) specimen is placed in the presence of an external magnetic field (a). The MAE has layered micro-structure (b).

3.2 Energy equation of laminates with the isotropic layers

We consider the laminates with the isotropic layers, with each layer $(r) \in \{m, f\}$ defined by the following amended energy function

$$W^{(r)} = W_e^{(r)} + W_m^{(r)}, \tag{3.2}$$

where $W_e^{(r)}$ is the elastic part and $W_m^{(r)}$ is the magnetic part. Although the analysis presented here is general, we consider the elastic part of both phases to adopt the neo-Hookean material model for simplicity. The corresponding energy function is

$$W_e^{(r)} = \frac{G^{(r)}}{2}(I_1 - 3), \tag{3.3}$$

where $G^{(r)}$ is the shear modulus of the phase (r) and $I_1^{(r)} = \operatorname{tr} \mathbf{C}^{(r)}$, $\mathbf{C}^{(r)} = \mathbf{F}^{(r)\mathsf{T}}\mathbf{F}^{(r)}$ is the right Cauchy-Green deformation tensor, and $\mathbf{F}^{(r)}$ is the deformation gradient. The magnetic part of the amended energy function $W_m^{(r)}$ for each layer is defined as

$$W_m^{(r)} = \rho^{(r)}\phi_m^{(r)} + \frac{1}{2\mu_0}\mathbf{B}\cdot\mathbf{B}, \tag{3.4}$$

where the term $\rho^{(r)}\phi_m^{(r)}$ can be defined either using the expression (2.45) or (2.53), according to the magnetic behavior of the layer; $\mathbf{B}^{(r)}$ denotes the magnetic induction vector. Note that the second term, $\mathbf{B}^{(r)}\cdot\mathbf{B}^{(r)}/(2\mu_0)$, is independent of material constants; therefore, the magnetic energy is non-zero in the free space or a non-magnetic material.

3.3 Magnetostriction

Here, we evaluate the deformation of the magneto-active laminates with the application of magnetic field $\bar{\mathbf{B}} = B\mathbf{e}_2$ without any mechanical traction. In particular, we study the homogenized response of the periodic unit cell shown in Fig. 3.1b. Using Eq. (2.19), the stress field inside an incompressible layer (r), with the amended energy function given by Eqs. (3.2)–(3.4) can be written as

$$\boldsymbol{\sigma}^{(r)} = G^{(r)}\bar{\mathbf{F}}\bar{\mathbf{F}}^T + \frac{1}{\mu^{(r)}}\bar{\mathbf{B}}\otimes\bar{\mathbf{B}} - p^{(r)}\mathbf{I}, \tag{3.5}$$

where the magnetic permeability $\mu^{(r)}$ can either be constant or a function of B (2.52) depending on the choice of the energy function.

The stress field jump condition across the interface $\mathbf{L} = \mathbf{e}_2$ yields $\sigma_{22}^{(m)} = \sigma_{22}^{(f)}$. We assume that the finite MAE specimen (Fig. 3.1a) is surrounded by a vacuum. Using the *mechanical* traction-free boundary conditions and the stress field jump condition, we obtain

$$c^{(m)}\boldsymbol{\sigma}^{(m)} + c^{(f)}\boldsymbol{\sigma}^{(f)} = \boldsymbol{\sigma}_m^*, \tag{3.6}$$

where $\boldsymbol{\sigma}_m^*$ is the Maxwell stress tensor defined as

$$\boldsymbol{\sigma}_m^* = \frac{1}{\mu_0}\left(\bar{\mathbf{B}} \otimes \bar{\mathbf{B}} - \frac{1}{2}(\bar{\mathbf{B}} \cdot \bar{\mathbf{B}})\mathbf{I}\right). \tag{3.7}$$

Then, the stress components become

$$\begin{aligned} &\sigma_{22}^{(r)} = \frac{G^{(r)}}{\lambda^2} + \frac{B^2}{\mu^{(r)}} - p^{(r)} = \frac{B^2}{2\mu_0}, \quad \text{and} \\ &c^{(m)}\sigma_{11}^{(m)} + c^{(f)}\sigma_{11}^{(f)} = \bar{G}\lambda^2 - (c^{(m)}p^{(m)} + c^{(f)}p^{(f)}) = -\frac{B^2}{2\mu_0}, \end{aligned} \tag{3.8}$$

By eliminating the Lagrange multipliers $p^{(m)}$ and $p^{(f)}$ from Eqs. (3.8), the relation between the applied magnetic field and induced stretch is obtained as

$$\lambda^2 - \lambda^{-2} = \frac{B^2}{\bar{G}\mu_0}(\tilde{\mu}_r^{-1} - 1), \tag{3.9}$$

where $\bar{G}$ is the average of the shear modulus of the materials weighted over volume fraction,

$$\bar{G} = c^{(m)}G^{(m)} + c^{(f)}G^{(f)} \tag{3.10}$$

and $\tilde{\mu}_r$ is the harmonic mean of relative magnetic permeability weighted over the volume fraction, defined as

$$\tilde{\mu}^{-1} = c^{(m)}{\mu^{(m)}}^{-1} + c^{(f)}{\mu^{(f)}}^{-1} \tag{3.11}$$

Here, $\mu_r^{(r)} = \mu^{(r)}/\mu_0$ is the relative magnetic permeability of phase (r). In the case of the linear magnetic layer, $\mu_r^{(r)}$ is a constant. However, for the ferromagnetic layer, $\mu_r^{(r)}$ can be expressed as a function of B, in terms of layer's magnetic saturation value $m_s^{(r)}$ and the initial magnetic susceptibility $\chi^{(r)}$ (see Eq. (2.52)). Hence, expression (3.9) is applicable for MAEs having layers with any type of magnetic behavior – linear or ferromagnetic. Eq. (3.9) further simplifies to yield an explicit expression for λ, namely,

$$\lambda = \left[\frac{\alpha + (\alpha^2 + 4)^{1/2}}{2}\right]^{1/2}, \tag{3.12}$$

where

$$\alpha = \frac{B^2(\tilde{\mu}_r^{-1} - 1)}{\bar{G}\mu_0}. \tag{3.13}$$

For magnetoactive layers ($\tilde{\mu}_r > 1$), the application of magnetic field results in contraction along the layer direction, $\lambda < 1$ (or $\lambda_2 > 1$). We note that certain magneto-mechanical loading conditions can lead to the development of magnetoelastic instabilities (Kankanala and Triantafyllidis, 2008; Rudykh and Bertoldi, 2013); the analysis of the magnetoelastic instabilities is provided in the following subsection.

3.4 Loading condition

Let us introduce a fixed Cartesian coordinate system with orthonormal basis vectors $x_i^0 (i = 1, 2, 3)$, such that the vector x_2^0 is perpendicular to the direction of lamination in the reference configuration (see Fig. 3.1). A pure homogeneous plane-strain deformation in the $x_1^0 - x_2^0$ plane is considered so that the deformation is completely described by

$$x_1 = \lambda x_1^0 \quad , \quad x_2 = \frac{x_2^0}{\lambda}, \quad x_3 = x_3^0 \tag{3.14}$$

where λ is the stretch along direction x_1^0. Homogeneity and perfect bonding between layers requires that all phases r share the same longitudinal stretch, namely $\lambda^\rho = \lambda (\rho = m, f)$.

In the plane-strain case in Fig. 3.1, we also assume the absence of a magnetic field in the x_3^0 direction. Application of the periodic boundary conditions allows us to determine the solution along a magneto-mechanical loading path. In this work, we investigate the magneto-mechanical loading defined as

$$\begin{aligned} \bar{\mathbf{F}} &= \lambda \mathbf{e_1} \otimes \mathbf{e_1} + \lambda^{-1} \mathbf{e}_2 \otimes \mathbf{e}_2 + \mathbf{e}_3 \otimes \mathbf{e}_3 \\ \bar{\mathbf{B}} &= B \mathbf{e}_2, \end{aligned} \tag{3.15}$$

where λ is the stretch along the direction of layers. Note that we consider an idealization of the periodic micro-structure that is made up of unit cells (schematically shown in Fig. 3.1b) and situated far from the specimen's boundaries. The mechanical and magnetic fields within the unit cell are assumed to be homogeneous in each layer of the laminate and are determined by the appropriate jump conditions.

3.5 General solution of the loaded specimen

Here diffuse modes corresponding to the non-homogeneous response of the composite with wavelengths (given by $2\pi/k_1$, where k_1 is the wavenumber) on the same order of the characteristic length of the heterogeneity are investigated. We then apply the Bloch-Floquet quasi periodicity condition at each L interval with wave number as k_2.

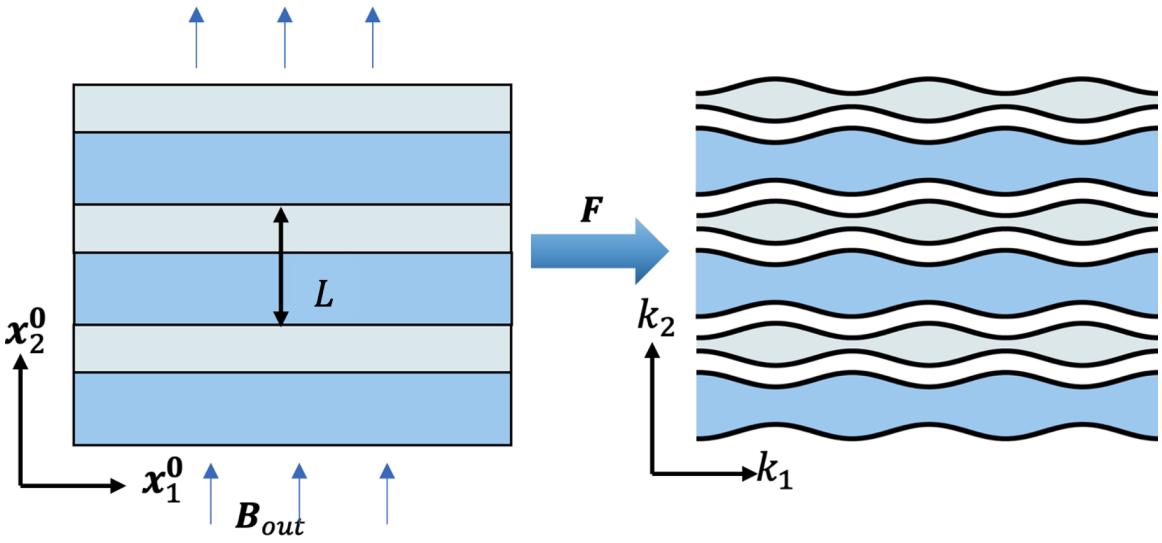

Figure 3.2: The onset of microscopic instabilities

The onset of instabilities Fig. 3.2 in MAE with bi-layered micro-structure is determined as follows. To solve the incremental boundary-value problem given by tensor Eq. (2.37) in each layer, we seek solutions in the form (Bertoldi and Gei, 2011).

$$\begin{aligned} v_1(x_1,x_2) &= \nu_1(x_2)\, e^{ik_1x_1} \\ v_2(x_1,x_2) &= \nu_2(x_2)\, e^{ik_1x_1} \\ \dot{B}_1(x_1,x_2) &= \mathcal{B}_1(x_2)\, e^{ik_1x_1} \\ \dot{B}_2(x_1,x_2) &= \mathcal{B}_2(x_2)\, e^{ik_1x_1} \\ \dot{p}(x_1,x_2) &= \rho(x_2)\, e^{ik_1x_1} \end{aligned} \tag{3.16}$$

where k_1 is the wavenumber along the $\mathbf{e}_1$-direction.

3.6 Substitution of general solution in magneto-elastic governing equations

From applying divergence laws $\nabla \cdot \dot{\boldsymbol{\sigma}} = \mathbf{0}$ given in Eq. (2.33) to the solution (3.16)

$$\begin{aligned} \frac{\partial \dot{\sigma}_{11}}{\partial x_1} + \frac{\partial \dot{\sigma}_{12}}{\partial x_2} &= 0 \\ \frac{\partial \dot{\sigma}_{21}}{\partial x_1} + \frac{\partial \dot{\sigma}_{22}}{\partial x_2} &= 0 \end{aligned} \tag{3.17}$$

Applying $\nabla \times \dot{\boldsymbol{H}} = \boldsymbol{0}$ given in Eq. (2.33) to the solution (3.16)

$$\frac{\partial \dot{H}_2}{\partial x_1} - \frac{\partial \dot{H}_1}{\partial x_2} = 0 \tag{3.18}$$

Substitution of $\nabla \cdot \dot{\boldsymbol{B}} = 0$ from Eq. $(3.16)_3$ into the Eq. $(2.33)_2$ results in

$$\frac{\partial \dot{B}_1}{\partial x_1} + \frac{\partial \dot{B}_2}{\partial x_2} = ik_1\mathcal{B}_1 + \mathcal{B}_2' = 0 \tag{3.19}$$

Incompressibility condition $\nabla \cdot \boldsymbol{v} = 0$ implies

$$\frac{\partial v_1}{\partial x_1} + \frac{\partial v_2}{\partial x_2} = ik_1\nu_1 + \nu_2' = 0 \tag{3.20}$$

where $(\bullet)' = (\bullet)_{,2}$.

3.7 Transformation of magneto-elastic governing equations into second order system

To get the final differential equations, substitute the tensor Eq. (2.37) into the stress governing Eq. (3.17) to get a second-order system of equations.

$$\begin{aligned} -ik_1\rho + k_1^2\left(\mathcal{A}_{1122} + \mathcal{A}_{1221} - \mathcal{A}_{1111}\right)\nu_1 + \mathcal{A}_{1212}\nu_1'' + ik_1\mathcal{M}_{112}\mathcal{B}_2 + \mathcal{M}_{121}\mathcal{B}_1' = 0 \\ i\rho' + ik_1^2\mathcal{A}_{2121}\nu_2 + \left(\mathcal{A}_{1221} + \mathcal{A}_{1122} - \mathcal{A}_{2222}\right)k_1\nu_1' + k_1\left(\mathcal{M}_{121} - \mathcal{M}_{222}\right)\mathcal{B}_1 = 0 \end{aligned} \tag{3.21}$$

Substitute the tensor Eq. (2.37) into magnetic intensity Eq. (3.18).

$$\mathcal{M}_{121}\nu_1'' + \left(\mathcal{M}_{112} + \mathcal{M}_{121} - \mathcal{M}_{222}\right)k_1^2\nu_1 + \mathcal{H}_{11}\mathcal{B}_1' - i\mathcal{H}_{22}k_1\mathcal{B}_2 = 0 \tag{3.22}$$

In terms of the non-zero components of magnetoelastic tensors, the incremental governing equation (2.37) can also be written as

$$\begin{aligned} &-ik_1\rho - k_1^2\mathcal{A}_{1111}\nu_1 + \mathcal{A}_{1212}\nu_1'' + \mathcal{M}_{121}\mathcal{B}_1' = 0, \\ &i\rho' + ik_1^2\mathcal{A}_{2121}\nu_2 - k_1\mathcal{A}_{2222}\nu_1' + k_1(\mathcal{M}_{121} - \mathcal{M}_{222})\mathcal{B}_1 = 0, \\ &\mathcal{M}_{121}\nu_1'' + k_1^2(\mathcal{M}_{121} - \mathcal{M}_{222})\nu_1 + \mathcal{H}_{11}\mathcal{B}_1' - ik_1\mathcal{H}_{22}\mathcal{B}_2 = 0. \end{aligned} \tag{3.23}$$

3.8 Transformation of magneto-elastic governing equations into a first-order system

Introducing a 6^{th} new variable substitution for ν_1'', such that $w_1 = \nu_1'$. We then transform the second order system (3.23) to first order system (3.26), and rearrange

$$\begin{gathered}
\nu_1' - w_1 = 0 \\
\mathcal{A}_{1212} w_1' + \mathcal{M}_{121} \mathcal{B}_1' + k_1^2 \left(\mathcal{A}_{1122} + \mathcal{A}_{1221} - \mathcal{A}_{1111}\right) \nu_1 + i k_1 \mathcal{M}_{112} \mathcal{B}_2 - i k_1 \rho = 0 \\
\nu_2' + i k_1 \nu_1 = 0 \\
\mathcal{M}_{121} w_1' + A_{11}\ \mathrm{B}_1' + \left(\mathcal{M}_{112} + \mathcal{M}_{121} - \mathcal{M}_{222}\right) k_1^2 \nu_1 - i \mathcal{H}_{22} k_1 \mathcal{B}_2 = 0 \\
\mathcal{B}_2' + i k_1 \mathcal{B}_1 = 0 \\
i \rho' + \left(\mathcal{A}_{1221} + \mathcal{A}_{1122} - \mathcal{A}_{2222}\right) k_1 w_1 + i k_1^2 \mathcal{A}_{2121} \nu_2 + k_1 \left(\mathcal{M}_{121} - \mathcal{M}_{222}\right) \mathcal{B}_1 = 0
\end{gathered} \tag{3.24}$$

Eqs. (3.20), (3.19) and (3.23) provide a set of six linear homogeneous first-order differential equations that depend on the vector of six unknown quantities. Let x be the distance in the $\mathbf{e}_2$ direction within a given phase and starting at its phase boundary, and let $\mathbf{y}(x)$ be a vector function such that

$$\mathbf{y}\left(x\right) = \left[\begin{array}{cccccc} \nu_1(x) & w_1(x) & \nu_2(x) & \mathcal{B}_1(x) & \mathcal{B}_2(x) & \rho(x) \end{array}\right]^T \tag{3.25}$$

Using (3.25), we transform the first-order system (3.24) into a matrix form.

$$\mathbf{A}\mathbf{y}' + \mathbf{B}\mathbf{y} = \mathbf{0} \tag{3.26}$$

where

$$\mathbf{y} = \left(\nu_1, w_1, \nu_2, \mathcal{B}_1, \mathcal{B}_2, \rho\right)$$

simplifying (3.26) further, the equations can be written together as

$$\mathbf{y}' = \mathbf{V}\mathbf{y} \tag{3.27}$$

where $\mathbf{V} = -\mathbf{A}^{-1}\mathbf{B}$. The non-zero components of the matrix $\mathbf{V}$ are calculated from Matrices $\mathbf{A}$ and $\mathbf{B}$

$$\mathbf{A} = \begin{pmatrix} 1 & 0 & 0 & 0 & 0 & 0 \\ 0 & \mathcal{A}_{1212} & 0 & \mathcal{M}_{121} & 0 & 0 \\ 0 & 0 & 1 & 0 & 0 & 0 \\ 0 & \mathcal{M}_{121} & 0 & \mathcal{H}_{11} & 0 & 0 \\ 0 & 0 & 0 & 0 & 1 & 0 \\ 0 & 0 & 0 & 0 & 0 & i \end{pmatrix} \tag{3.28}$$

$$\mathbf{B} = \begin{pmatrix} 0 & -1 & 0 & 0 & 0 & 0 \\ k_1^2\left(\mathcal{A}_{1122}+\mathcal{A}_{1221}-\mathcal{A}_{1111}\right) & 0 & 0 & 0 & ik_1\mathcal{M}_{112} & -ik_1 \\ ik_1 & 0 & 0 & 0 & 0 & 0 \\ \left(\mathcal{M}_{112}+\mathcal{M}_{121}-\mathcal{M}_{222}\right)k_1^2 & 0 & 0 & 0 & -i\mathcal{H}_{22}k_1 & 0 \\ 0 & 0 & 0 & ik_1 & 0 & 0 \\ 0 & \left(\mathcal{A}_{1221}+\mathcal{A}_{1122}-\mathcal{A}_{2222}\right)k_1 & ik_1^2\mathcal{A}_{2121} & k_1\left(\mathcal{M}_{121}-\mathcal{M}_{222}\right) & 0 & 0 \end{pmatrix} \tag{3.29}$$

3.9 Matrix solution of first order magneto-elastic system of equations

The general solution to first-order differential Eq. (3.27) is of the form

$$\mathbf{y}(x) = \mathbf{W}e^{\mathbf{Z}x}\mathbf{k}, \tag{3.30}$$

where $\mathbf{W}$ is the eigenvector matrix of $\mathbf{V}$, Here, $\mathbf{z}$ is the eigenvalue vector of matrix $\mathbf{V}$; $\mathbf{Z} = \text{diag}[(\mathbf{z})]$ is a diagonal eigenvalue matrix of $\mathbf{V}$. $\mathbf{k}$ is an arbitrary constant vector that will be determined using the continuity and quasi-periodic boundary conditions of the unit cell.

For initial conditions, let $\mathbf{y}(0) = \mathbf{y}_0$. Then $\mathbf{k} = \mathbf{W}^{-1}\mathbf{y}_0$ therefore the general solution to the first-order system (3.26) can be rewritten in terms of the initial value $\mathbf{y}_0$ as

$$\mathbf{y}(x) = \mathbf{W}e^{\mathbf{Z}x}\mathbf{W}^{-1}\mathbf{y_0} \tag{3.31}$$

3.10 Jump conditions at the fiber-matrix interface

Applying Euler boundary conditions (2.7) and converting to incremental form and substituting the microscopic solution (3.16). The displacement continuity condition at the layer interface implies

$$\left(\mathbf{F}^{(m)} - \mathbf{F}^{(f)}\right)\cdot\mathbf{s} = \mathbf{0} \tag{3.32}$$

where $\mathbf{s}$ is a unit vector perpendicular to the lamination direction $\mathbf{N}$. Using Eq. (3.32), for the deformation gradient $\bar{\mathbf{F}}$ $(3.15)_1$ with incompressible phases, we can write

$$\mathbf{F}^{(m)} = \mathbf{F}^{(f)} = \lambda\mathbf{e_1}\otimes\mathbf{e_1} + \lambda^{-1}\mathbf{e}_2\otimes\mathbf{e}_2 + \mathbf{e}_3\otimes\mathbf{e}_3. \tag{3.33}$$

In the deformed configuration, the thicknesses of the matrix and stiff layers are $L^{(m)} = c^{(m)}L$ and $L^{(f)} = c^{(f)}L$, respectively, where L is the period of the layered material in

the current state. Moreover, using the magnetic induction jump condition (2.7) at the interface for the current magnetic loading $(3.15)_2$, we obtain

$$\mathbf{B}^{(f)} = \mathbf{B}^{(m)} = B\mathbf{e}_2 \tag{3.34}$$

The set of interface jump conditions for the incremental fields are

$$[\![\dot{\boldsymbol{\sigma}}]\!]\mathbf{N} = \mathbf{0}, \quad [\![\dot{\mathbf{B}}]\!] \cdot \mathbf{N} = 0, \quad \text{and} \quad [\![\dot{\mathbf{H}}]\!] \times \mathbf{N} = \mathbf{0} \tag{3.35}$$

the displacement continuity equations are

$$\begin{aligned} [\![\nu_1]\!] &= 0 \\ [\![\nu_2]\!] &= 0 \end{aligned} \tag{3.36}$$

the traction continuity equations are

$$\begin{aligned} [\![\mathcal{M}_{121}\mathcal{B}_1 + ik_1\left(\mathcal{A}_{1221} + p\right)\nu_2 + \mathcal{A}_{1212}w_1]\!] &= 0 \\ [\![\mathcal{M}_{222}\mathcal{B}_2 + ik_1\left(\mathcal{A}_{1122} - \mathcal{A}_{2222} - p\right)\nu_1 - q]\!] &= 0 \end{aligned} \tag{3.37}$$

The magnetic field interface conditions are

$$\begin{aligned} [\![\mathcal{B}_2]\!] &= 0 \\ [\![\mathcal{H}_{11}\mathcal{B}_1 + \mathcal{M}_{121}w_1 + i\mathcal{M}_{121}k_1\nu_2]\!] &= 0 \end{aligned} \tag{3.38}$$

Change (3.39) to differential equation $[\![\boldsymbol{Q}\mathbf{y}]\!] = \mathbf{0}$, at each boundary interface Using Eqs. (3.16), (3.20), and (3.19), the jump conditions (3.35) can be rewritten in terms of the non-zero tensor components as

$$\begin{aligned} &[\![\nu_1]\!] = 0, \quad [\![\nu_2]\!] = 0, \quad [\![\mathcal{B}_2]\!] = 0, \\ &[\![\mathcal{M}_{121}\mathcal{B}_1 + ik_1 p\nu_2 + \mathcal{A}_{1212}\nu_1']\!] = 0, \\ &[\![\mathcal{M}_{222}\mathcal{B}_2 - ik_1(\mathcal{A}_{2222} + p)\nu_1 - q]\!] = 0, \\ &[\![\mathcal{H}_{11}\mathcal{B}_1 + \mathcal{M}_{121}\nu_1' + i\mathcal{M}_{121}k_1\nu_2]\!] = 0. \end{aligned} \tag{3.39}$$

Based on the interface boundary conditions, we can create a $\mathbf{Q}$ matrix to indicate the change of variables at the interface.

$$\mathbf{Q}^{(m)}\mathbf{y}^{(m)} = \mathbf{Q}^{(f)}\mathbf{y}^{(f)} \tag{3.40}$$

writing $\mathbf{y}^{(f)}$ in explicit form,

$$\mathbf{y}^{(f)} = \left(\mathbf{Q}^{-1^{(f)}}\mathbf{Q}^{(m)}\right)\mathbf{y}^{(m)} \tag{3.41}$$

where $\mathbf{Q}$ is

$$\boldsymbol{Q} = \begin{pmatrix} 1 & 0 & 0 & 0 & 0 & 0 \\ 0 & 0 & 1 & 0 & 0 & 0 \\ 0 & \mathcal{A}_{1212} & ik_1\left(\mathcal{A}_{1221}+p\right) & \mathcal{M}_{121} & 0 & 0 \\ ik_1\left(\mathcal{A}_{1122}-\mathcal{A}_{2222}-p\right) & 0 & 0 & 0 & \mathcal{M}_{222} & -1 \\ 0 & 0 & 0 & 0 & 1 & 0 \\ 0 & \mathcal{M}_{121} & i\mathcal{M}_{121}k_1 & \mathcal{H}_{11} & 0 & 0 \end{pmatrix} \tag{3.42}$$

Eq. (3.39) can be written in the form $[\![\mathbf{Qy}]\!] = \mathbf{0}$. The non-zero components of the matrix $\mathbf{Q}$ are

$$\begin{aligned} &Q_{11} = Q_{23} = Q_{55} = -Q_{46} = 1, \quad Q_{32} = \mathcal{A}_{1212}, \quad Q_{33} = ik_1 p, \\ &Q_{34} = \mathcal{M}_{121}, \quad Q_{41} = -ik_1(\mathcal{A}_{2222}+p), \quad Q_{45} = \mathcal{M}_{222}, \\ &Q_{62} = \mathcal{M}_{121}, \; Q_{63} = ik_1\mathcal{M}_{121}, \quad Q_{64} = \mathcal{H}_{11}. \end{aligned} \tag{3.43}$$

3.11 Bloch-Floquet periodicity condition

For the periodic unit cell of the layered composite (as shown in Fig. 3.3a), the quasi-periodic boundary conditions are

$$\mathbf{y}(x_2 + L) = \mathbf{y}(x_2)\exp(ik_2 L), \tag{3.44}$$

where $k_2 \in [0, 2\pi/L)$ is the Floquet parameter. We apply the Bloch-Floquet quasi-periodicity condition at each L interval. The wavenumber k_2 is frequently termed the 'Bloch parameter' and sets the shape of modes along the transverse direction.

$$\mathbf{y_L} = e^{ik_2 L}\mathbf{y_0} \tag{3.45}$$

As $\mathbf{y_0}$ and $\mathbf{y_L}$ are both real,

$$e^{ik_2 L} = \pm 1 \tag{3.46}$$

using definition of stretch in x_2 direction as $1/\lambda = L/L_0$ and solving for k_2,

$$k_2 = \frac{n\lambda\pi}{L^0} \tag{3.47}$$

where n is an integer. Normalizing k_2 with respect to L^0, we get the normalized wavenumber $\bar{k}_2$ as

$$\bar{k}_2 = k_2 L^0 = n\lambda\pi \tag{3.48}$$

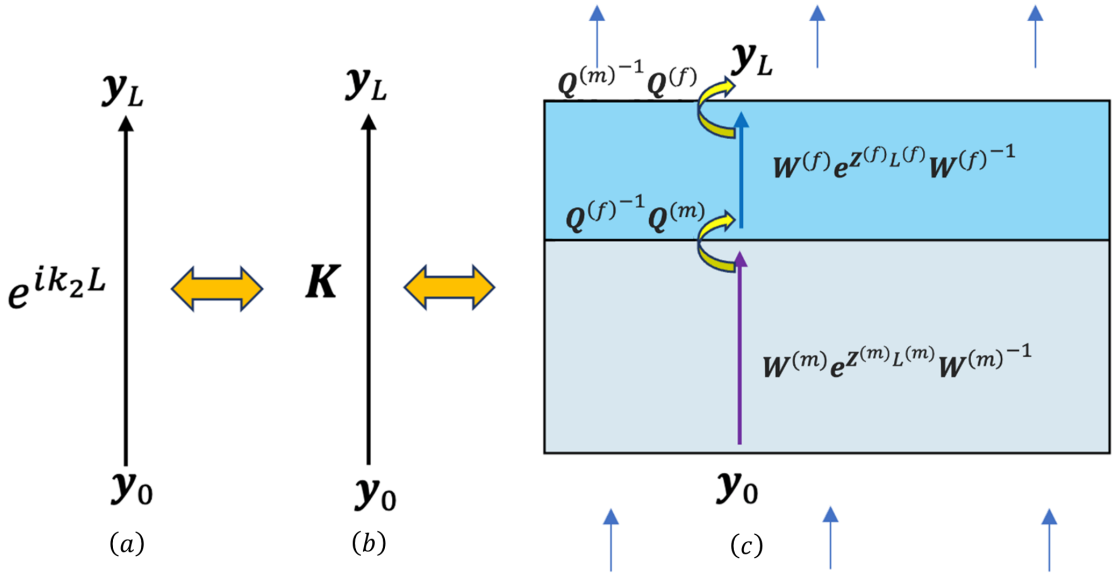

Figure 3.3: The following three relations are equivalent (a) The Bloch-Floquet boundary condition (b) **K** matrix definition (c) the non-trivial solution with interface jump conditions

3.12 Non-trivial solution of the magneto-elastic equations

Combining the interface (3.41), and first-order solution (3.31) into a single equation, we get the general solution (3.49), in the form of a **K** matrix(3.50)

$$\mathbf{y} = \boldsymbol{K}\boldsymbol{y}_0 \tag{3.49}$$

where the matrix **K** is as follows

$$\begin{aligned}\mathbf{K} = &\left[\boldsymbol{Q}^{(m)^{-1}}\boldsymbol{Q}^{(f)}\right]\left[\boldsymbol{W}^{(f)}e^{\boldsymbol{Z}^{(f)}L^{(f)}}\boldsymbol{W}^{(f)^{-1}}\right]\cdots \\ &\left[\boldsymbol{Q}^{(f)^{-1}}\boldsymbol{Q}^{(m)}\right]\left[\boldsymbol{W}^{(m)}e^{\boldsymbol{Z}^{(m)}L^{(m)}}\boldsymbol{W}^{(m)^{-1}}\right]\end{aligned} \tag{3.50}$$

Here $(\cdots)$ indicates that the matrix product is continued on the next line. The derivation of the **K** matrix can also be visualized from Fig. 3.3c.

Alternatively, the **K** matrix can also be derived using the following analytical method (see Bertoldi and Gei, 2011). let $\mathcal{Z}^{(r)}(x) = e^{\mathbf{Z}^{(r)}x}$. In the domain $0 < x_2 < L + L^{(m)}$, solution (3.30) takes the form

$$\begin{aligned}\mathbf{y}(x_2) &= \mathbf{W}^{(m)}\mathcal{Z}^{(m)}(x_2)\mathbf{y}_0{}^{(m-)}, \quad 0 < x_2 < L^{(m)}., \\ \mathbf{y}(x_2) &= \mathbf{W}^{(f)}\mathcal{Z}^{(f)}(x_2)\mathbf{y}_0{}^{(f)}, \quad L^{(m)} < x_2 < L., \\ \mathbf{y}(x_2) &= \mathbf{W}^{(m)}\mathcal{Z}^{(m)}(x_2)\mathbf{y}_0{}^{(m+)}, \quad L < x_2 < L + L^{(m)}\end{aligned} \tag{3.51}$$

On substituting Eqs. (3.51) into (3.44), we obtain

$$\mathbf{y}_0{}^{(m+)} = \exp(ik_2 L)\Big(\mathcal{Z}^{(m)}(L)\Big)^{-1}\mathbf{y}_0{}^{(m-)}. \tag{3.52}$$

Finally, by using Eq. (3.51) we obtain

$$\begin{aligned}\mathbf{Q}^{(m)}\mathbf{W}^{(m)}\mathcal{Z}^{(m)}(L^{(m)})\mathbf{y}_0{}^{(m-)} &= \mathbf{Q}^{(f)}\mathbf{W}^{(f)}\mathcal{Z}^{(f)}(L^{(m)})\mathbf{y}_0{}^{(f)}\\ \mathbf{Q}^{(m)}\mathbf{W}^{(m)}\mathcal{Z}^{(m)}(L)\mathbf{y}_0{}^{(m-)} &= \mathbf{Q}^{(f)}\mathbf{W}^{(f)}\mathcal{Z}^{(f)}(L)\mathbf{y}_0{}^{(f)}\end{aligned} \tag{3.53}$$

Combining Eqs. (3.52) and (3.53) results in the following condition for the existence of a non-trivial solution

$$\det\Big[\mathbf{K} - e^{ik_2 L}\mathbf{I}\Big] = 0, \tag{3.54}$$

where

$$\begin{aligned}\mathbf{K} = \Big[\mathbf{Q}^{(m)}\mathbf{W}^{(m)}\Big]^{-1}\mathbf{Q}^{(f)}\mathbf{W}^{(f)}\mathcal{Z}^{(f)}(L^{(f)})\cdots\\ \Big[\mathbf{Q}^{(f)}\mathbf{W}^{(f)}\Big]^{-1}\mathbf{Q}^{(m)}\mathbf{W}^{(m)}\mathcal{Z}^{(m)}(L^{(m)})\end{aligned} \tag{3.55}$$

3.13 Eigen value constraint of K matrix

Combining the Bloch-Floquet boundary condition (3.45) with the K-matrix solution (3.49), a constraint condition for the eigenvalue of $\boldsymbol{K}$ matrix is derived

$$\boldsymbol{y}_L = \boldsymbol{K}\boldsymbol{y}_0 = e^{ik_2 L}\boldsymbol{y}_0 \tag{3.56}$$

Let ζ_i be an eigenvalue of matrix $\mathbf{K}$, by definition of eigenvalue, we have

$$\boldsymbol{K}\boldsymbol{y_0} = \zeta_i\boldsymbol{y_0} \tag{3.57}$$

For non-trivial solution to exist (3.56), at least one of eigenvalue ζ_i of $\mathbf{K}$ must be $e^{ik_2 L}$. Therefore from (3.57) and (3.56)

$$\zeta_i = e^{ik_2 L} \tag{3.58}$$

To eliminate k_2, we use the fact that the magnitude of the imaginary exponent is unity. Thus the magnitude of at least one of the eigenvalues of $\boldsymbol{K}$ must be 1. Therefore, the eigenvalue constraint (3.58) reduce to

$$|\zeta_i| = 1 \tag{3.59}$$

Thus, the first occurrence of unity magnitude of the eigenvalue along any path is the point on the onset of the microscopic instability. If the condition (3.54) is satisfied for a combination of mechanical and magnetic loads, an incremental solution of the form (3.16)

exists, making the elastomer unstable. The solution $\mathbf{y}$ lies in the real space, e^{ik_2L} is also real-valued; hence, Using Eq. (3.44), (3.58), (3.46) the eigenvalue constraint is further simplified to

$$\zeta_i = \pm 1 \tag{3.60}$$

The instability criterion (3.60) is evaluated by scanning over the values of k_1 at different deformation levels for a given magnetic field until the eigenvalue with $\zeta_i = \pm 1$ is obtained. Once the condition is satisfied, the corresponding stretch along the direction of layers ($\mathbf{e}_1$) that separates the unstable and stable domain is termed as the critical stretch λ_{cr} and the corresponding wave number is the critical wave number k_{1cr}.

3.14 Symmetric vs. anti-symmetric modes

Based on the buckling pattern wavelength, we distinguish the macroscopic (or long-wave) and microscopic instabilities. Macroscopic instability is characterized by the critical wavelength significantly larger than the characteristic microstructure ($k_{1cr} \to 0$). In contrast, microscopic instability may lead to the formation of a new periodicity of the order of the initial microstructure.

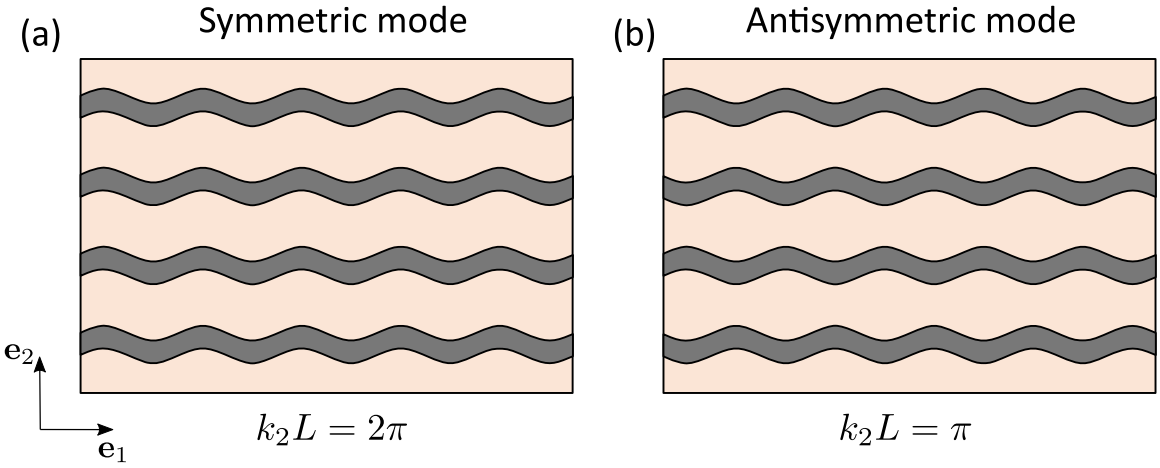

Figure 3.4: Schematic representation of the symmetric (a) and anti-symmetric (b) microscopic instability modes.

Furthermore, depending on the two possible values of eigenvalue: $\exp(ik_2L) = 1$ and -1, the buckling modes can be classified as symmetric for $k_2L = 2n\pi$ and anti-symmetric for $k_2L = (2n-1)\pi$ (with n being an integer). For illustrating these instability modes in the plots, hereafter, we use $k_2L = 2\pi$ and $k_2L = \pi$ (with $n = 1$) to represent the symmetric and anti-symmetric modes, respectively. These buckling modes are schematically shown in Fig. 3.4.

3.15 Pure mechanical loading

In the special case of a pure mechanical model in the absence of a magnetic field, the expressions for the bi-layered laminates are given below. (see Bertoldi and Lopez-Pamies, 2012), we keep the displacement (3.36) and the traction continuity conditions (3.37) and remove the magnetic field conditions by eliminating 2 of the rows and columns relating to magnetic fields from the following matrices $\mathbf{y}$, $\mathbf{A}$, $\mathbf{B}$, and $\mathbf{Q}$ transform into the following matrices (see Geymonat et al., 1993, for the purely mechanical case). The vector y from (3.25) reduces to

$$\mathbf{y}(x) = \begin{bmatrix} \nu_1 & \nu_1' & \nu_2 & \rho \end{bmatrix}^T \tag{3.61}$$

The matrix $\mathbf{A}$ from (3.28) reduces to

$$\boldsymbol{A} = \begin{pmatrix} 1 & 0 & 0 & 0 \\ 0 & \mathcal{A}_{1212} & 0 & 0 \\ 0 & 0 & 1 & 0 \\ 0 & 0 & 0 & i \end{pmatrix} \tag{3.62}$$

The matrix $\mathbf{B}$ from (3.29) reduces to

$$\boldsymbol{B} = \begin{pmatrix} 0 & -1 & 0 & 0 \\ k_1^2\left(\mathcal{A}_{1122} + \mathcal{A}_{1221} - \mathcal{A}_{1111}\right) & 0 & 0 & -ik_1 \\ ik_1 & 0 & 0 & 0 \\ 0 & \left(\mathcal{A}_{1221} + \mathcal{A}_{1122} - \mathcal{A}_{2222}\right)k_1 & ik_1^2\mathcal{A}_{2121} & 0 \end{pmatrix}$$

The matrix $\mathbf{Q}$ from (3.42) reduces to

$$\boldsymbol{Q} = \begin{pmatrix} 1 & 0 & 0 & 0 \\ 0 & 0 & 1 & 0 \\ 0 & \mathcal{A}_{1212} & ik_1\left(\mathcal{A}_{1221} + p\right) & 0 \\ ik_1\left(\mathcal{A}_{1122} - \mathcal{A}_{2222} - p\right) & 0 & 0 & -1 \end{pmatrix} \tag{3.63}$$

Other parts of the analysis (like the K-matrix and the eigenvalue constraints etc.) remain identical to the procedure described previously for Eq. (3.50) and Eq. (3.59).

Chapter 4

Results

4.1 Numerical methods for evaluating solutions to the magneto-elastic equations

To validate our analysis, we used the following explicit expression for macroscopic analysis (see Rudykh and Bertoldi, 2013, for reference).

$$\lambda_{cr}(B) = \left[1 - \frac{\tilde{G}}{\bar{G}} + \frac{B}{\bar{G}\tilde{\mu}}\left(1 - \frac{\tilde{\mu}}{\bar{\mu}}\right)\right]^{\frac{1}{4}} \tag{4.1}$$

where $(\bar{G})$ is the average and $(\tilde{\mu})$ is the harmonic average, both weighted over the volume fractions of the phases, such that

$$\begin{aligned} \bar{\mu} &= c^{(m)}\mu^{(m)} + c^{(f)}\mu^{(f)}, \\ \tilde{G}^{-1} &= c^{(m)}{G^{(m)}}^{-1} + c^{(f)}{G^{(f)}}^{-1} \end{aligned} \tag{4.2}$$

and $\bar{G}$, $\tilde{\mu}$ are as defined in (3.10) and (3.11) respectively.

Eq. (4.1) is valid for a special case of macroscopic analysis when $(k_{1_{cr}} \to 0)$. In general, for any value of $(k_{1cr} > 0)$, we do not have an explicit expression for λ_{cr}; therefore, we have to resort to numerical methods for getting the value λ_{cr} and k_{1cr}.

4.1.1 Eigenvalue characteristic polynomial function

In this section, we will go through a numerical method for solving the eigenvalue constraint Eq. (3.59). Although the final eigenvalue Eq. (3.59) appears to be trivial, algorithmically calculating these eigenvalues over a large domain has its fair share of challenges and limitations. In this analysis, the $\mathbf{K}$ matrix expression (3.50) is considered to be a function of parameters stretch λ and the wavenumber k_1, while other variables in the $\mathbf{K}$ matrix are

assumed to be constants. Let us define a characteristic eigenvalue function as $f(\lambda, k_1, \zeta)$ such that

$$f(\lambda, k_1, \zeta) = |\boldsymbol{K}(\lambda, k_1) - \zeta \boldsymbol{I}| \tag{4.3}$$

where ζ is a parameter and $|\bullet|$ is the determinant of the matrix expression $\boldsymbol{K} - \zeta \boldsymbol{I}$. Let ζ_i be one of the eigenvalue of matrix $\mathbf{K}$. If $\zeta = \zeta_i$ and is indeed an eigenvalue of $\mathbf{K}$, then by definition of eigenvalue,

$$f(\lambda, k_1, \zeta_i) = |\boldsymbol{K}(\lambda, k_1) - \zeta_i \boldsymbol{I}| = 0 \tag{4.4}$$

According to (3.59), to solve for the critical point, we apply the eigenvalue constraint $\zeta_i = \pm 1$ in (4.4). Therefore, we search the pairs of values (λ, k_1) within an empirically determined domain, such that $f(\lambda, k_1, \pm 1)$ becomes equal to 0.

$$f(\lambda, k_1, \pm 1) = 0 \tag{4.5}$$

To visualize the point where $f = 0$, the function f is then plotted using colored contours and the corresponding (λ, k_1) points at which this condition (4.5) is visible as a sharp and distinct boundary between the two colors in Fig. 4.1. Among these boundary points, the point that has the highest (λ) value is the onset of instabilities. Eigenvalues $\zeta_i = 1$ and $\zeta_i = -1$ correspond to the symmetric and anti-symmetric modes, respectively, as the complex phase angle of k_2 is 360° and 180°degrees, respectively.

The function f has matrix exponents, and in general, the intersection with zero is hard to discern. So to make function f more well-behaved and have a clear boundary around 0, we transform f. Let's define the transformation as a logarithmic bounding function $b(f)$ such that we get the lower bound and upper bound as 0 and 20, respectively.

$$b(f) = \log_{10}\left(\min\left(\max\left(10^{-10}, \text{real}\left(f\right)\right), 10^{10}\right)\right) + 10 \tag{4.6}$$

Applying the $b(f)$ to $f(\lambda, k_1, \zeta)$, we define $f'(\lambda, k_1, \zeta)$ such that

$$f'(\lambda, k_1, \zeta) = b(f(\lambda, k_1, \zeta)) \tag{4.7}$$

The function f' can be further simplified into a step function $g(\lambda, k_1, \zeta)$,

$$g(\lambda, k_1, \zeta) = \begin{cases} 1, \text{ if } f'(\lambda, k_1, \zeta) > 0 \\ 0, \text{ if } f'(\lambda, k_1, \zeta) \leq 0 \end{cases} \tag{4.8}$$

The function $g(\lambda, k_1, \zeta)$ gives us a sharp and clear boundary for calculating and visualizing the eigenvalue constraint (3.59).

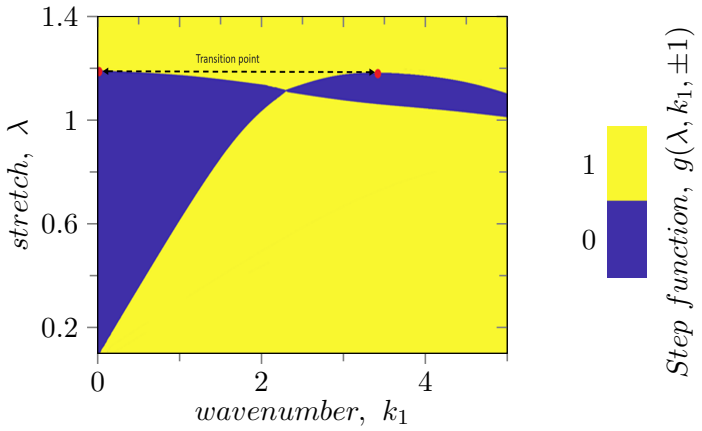

Figure 4.1: Characteristic eigenvalue function $f(\lambda, k_1)$ plot for one of the eigenvalues describing the transition between macroscopic instability and microscopic instability modes at $B_m = 4.9$, $c^{(f)} = 0.6$, $\chi^{(f)} = 0.9$

4.1.2 Examples of symmetric and anti-symmetric instability modes

Based on Eq (3.60) $\zeta_i = \pm 1$, two sets of solutions are obtained, one for each of the cases ± 1.

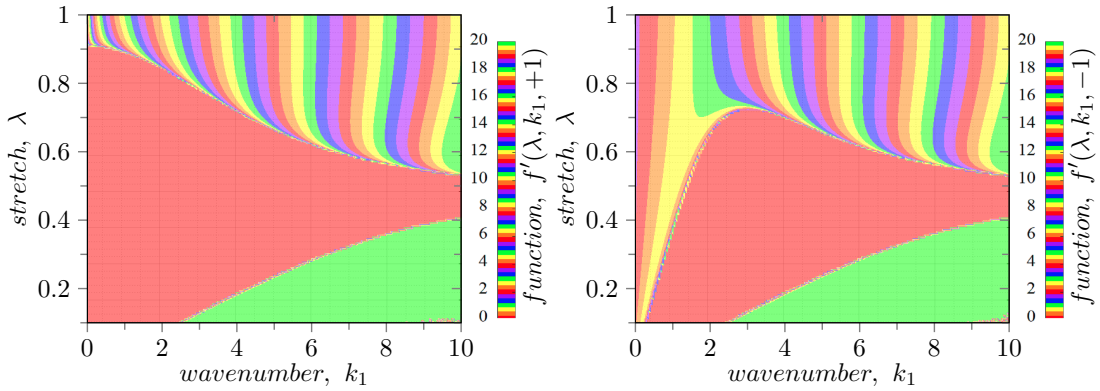

(a) Symmetric ($\zeta_i = +1$)

(b) Anti-symmetric ($\zeta_i = -1$)

Figure 4.2: The Eigenvalues characteristic functions f is contour plotted (4.4) for the eigenvalues ± 1. The continuous red region describes the positive eigen function, and the banded region is the negative eigen function. The x and y axes are stretch and k_1, respectively, and contours represent the value of eigen function for $c^{(f)} = 0.50$ for at $B_m = 0$.

The maximas for each of the contours in Fig. 4.2a,b are calculated and compared. Depending on which maxima is greater, we determine whether the corresponding mode

is symmetric or anti-symmetric. The symmetric and anti-symmetric λ_{cr} *vs* B_m plots are shown in solid (−) and dashed lines (- -) respectively in Fig. 4.3a. The symmetric curve usually (but not necessarily) corresponds to macroscopic instability. The anti-symmetric curve is always in the microscopic instability region. The transition point from macroscopic to microscopic instability is the intersection of the symmetric and anti-symmetric curves. The transition point is shown in k_{1cr} diagram as a sudden jump in the value of k_{1cr} is shown in Fig. 4.3b.

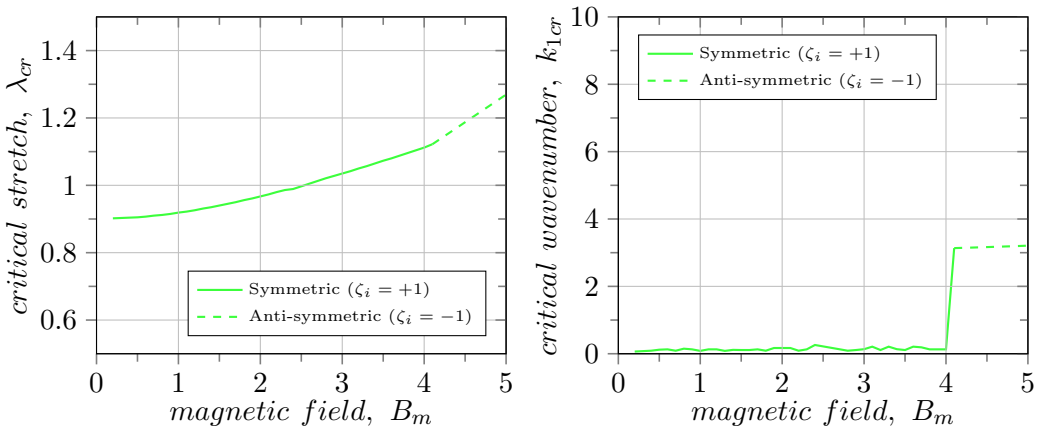

(a) λ_{cr} vs B_m (b) k_{1cr} vs B_m

Figure 4.3: The symmetric and anti-symmetric λ_{cr} *vs* B_m plots are shown in solid (−) and dashed (- -) lines respectively. Their intersection is usually the transition point between the macroscopic to microscopic instabilities at $c^{(f)} = 0.6$, $\chi = 0.95$

4.1.3 Numerical limitations

When calculating the eigenvalue near $\lambda_{cr} = 1$, matrix singularities are reached. Thus we must avoid this region in general and interpolate the values to get solutions within this region.

The four eigenvalue contour plots were generated for the K matrix in the special case of pure mechanical model (see sec. 3.15). As can be seen from Fig. 4.4, if we attempt to calculate the eigenvalues directly, discontinuities start showing up in the contour plots. Hence, it's quite cumbersome to create a robust algorithm over such a noisy data set as input.

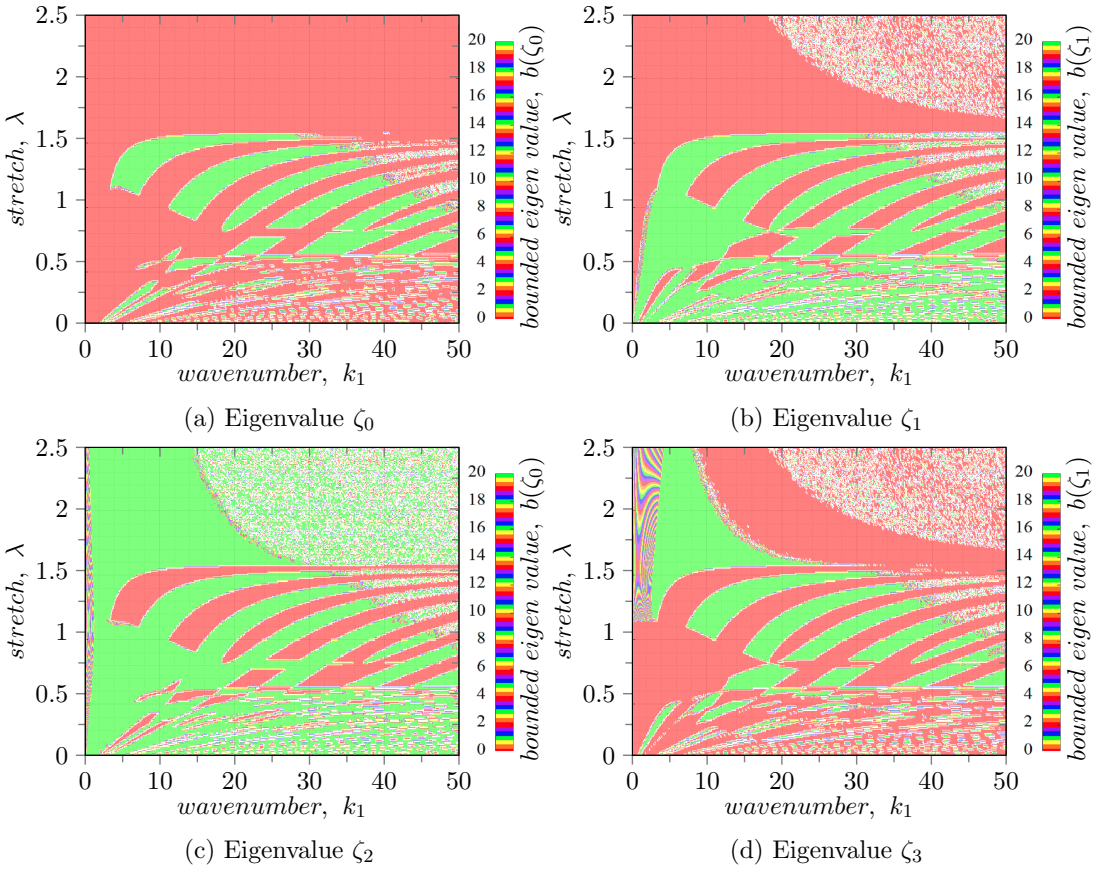

(a) Eigenvalue ζ_0

(b) Eigenvalue ζ_1

(c) Eigenvalue ζ_2

(d) Eigenvalue ζ_3

Figure 4.4: Four eigenvalue contour plots of the **K** matrix are generated in the special case of pure mechanical model (see sec. 3.15). The discontinuities in the contour plots prevent us from creating a robust algorithm for detecting the eigenvalue constraint

Hence it is not recommended to solve the constraint Eq. (3.59) directly using the actual eigenvalues of the matrix **K**. Instead, the characteristic eigenvalue polynomial f Eq. (4.4) is recommended to be used (after appropriate transformation to a step function g Eq. (4.8))

At extremely low and high volume fractions $c^{(f)} < 0.02$ and $c^{(f)} > 0.98$, numerical noise increases in the solution because of the matrix singularities caused by exponential terms involved, thus making this method impractical beyond this threshold of volume fractions. An example of this noise is shown in Fig. 4.5

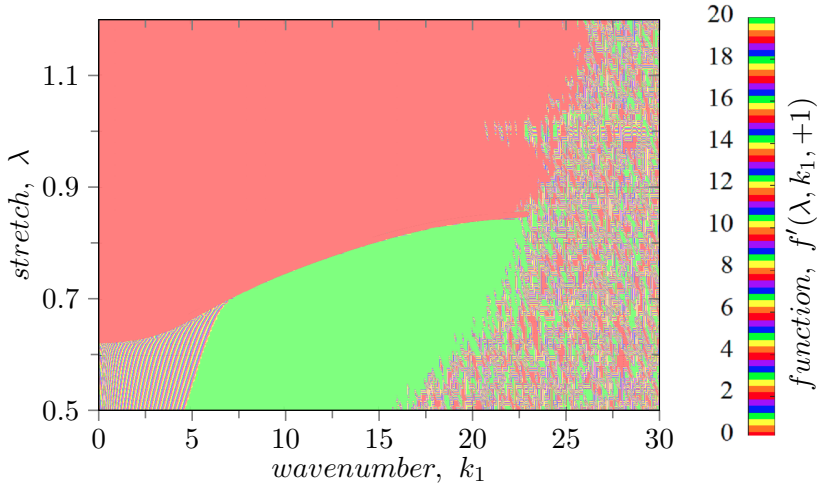

Figure 4.5: At low fiber volume fraction $c^{(f)} = 0.01$ and $\mu^{(f)} = 2.5$, numerical noise is observed because of $\mathbf{K}$ matrix singularities due to the exponential terms present in the solution.

4.2 Numerical Simulation

In the numerical simulation, the matrix phase, which is soft, is assumed to be magnetically inactive (i.e., $\mu^{(m)} = 1$). Here we focus on multilayered materials characterized by shear modulus contrast ratio $k_g = G^{(f)}/G^{(m)} = 10$ and three permeability ratios $k_\mu = \mu^{(f)}/\mu^{(m)} = (1.6, 5, 20)$

4.2.1 Loading conditions

We used the case of pure shear as given in Rudykh and Bertoldi (2013)

$$F = \lambda \boldsymbol{e}_1^0 \otimes \boldsymbol{e}_1^0 + \lambda^{-1} \boldsymbol{e}_2^0 \otimes \boldsymbol{e}_2^0 + \boldsymbol{e}_3^0 \otimes \boldsymbol{e}_3^0 \tag{4.9}$$

$$\boldsymbol{B}_{\text{out}}^0 = B^0 \boldsymbol{e}_2^0 \tag{4.10}$$

4.2.2 Energy models for the matrix and fiber phases

The composite is made of two phases, each having its own material parameters and energy model.

Matrix phase

For simplicity, we have considered the matrix phase (m) to be magnetically inactive $\left(\mu^{(m)}=1\right)$. The energy-density function of a two-phase composite is given below. Substitute $\mu^{(m)}=1$ and linear energy density function is

$$\Psi\left(\boldsymbol{F},\boldsymbol{B}^0\right)=\frac{G^{(m)}}{2}\left(I_1-3\right)+\frac{\boldsymbol{F}\boldsymbol{B}^0\cdot\boldsymbol{F}\boldsymbol{B}^0}{2\mu_0} \tag{4.11}$$

Note the Maxwell term $\frac{1}{2\mu_0}\boldsymbol{F}\boldsymbol{B}^0\cdot\boldsymbol{F}\boldsymbol{B}^0$ is still present even if the material is magnetically inactive. The matrix phase has a shear modulus $G^{(m)}$.

Fiber phase

The fiber phase (f) is magnetically active. The fiber phase has a shear modulus of $G^{(f)}$. There are two different energy densities applied to this phase. The linear energy model (2.47) and Langevin's energy model (2.56) are used to analyze the behavior of the fiber phase.

4.2.3 Non-dimensional numbers

For the non-dimensional analysis, the matrix phase (m) is taken as the reference material. Using the non-dimensional analysis, we make the following normalization in the numerical solution.

Magnetic field

The magnetic field can be non-dimensionalized with respect to $G^{(m)}\mu_0$. The non-dimensional magnetic fields are

$$B_m=\frac{B}{\sqrt{G^{(m)}\mu_0}} \tag{4.12}$$

Stretch ratio

The stretch ratio is the ratio of the length in the current configuration and the length in the reference configuration. If we take the $\boldsymbol{x}_1$ direction as a reference, the stretch in the $\boldsymbol{x}_1$ direction is λ and that in the $\boldsymbol{x}_2$ direction is $1/\lambda$.

$$1/\lambda=\frac{L}{L_0} \tag{4.13}$$

Shear-to-saturation ratio

A co-efficient η characterizes the ratio between magnetic saturation and the shear modulus.

$$\eta = \frac{m_s \mu_0}{\sqrt{G^{(m)} \mu_0}} \tag{4.14}$$

Wavenumber

The wavenumbers k_1 and k_2 are normalized with respect to the total initial height of a periodic layer.

$$\bar{k}_1 = k_1 L^0 \quad , \quad \bar{k}_2 = k_2 L^0 \tag{4.15}$$

Volume fraction

The volume fractions $c^{(m)}$ and $c^{(f)}$ vary between 0 to 1, and it is the length of each phase with respect to the length of each layer.

$$c^{(m)} = \frac{L^{(m)}}{L}, \quad c^{(f)} = \frac{L^{(f)}}{L} \tag{4.16}$$

Shear modulus ratio

The shear modulus ratio between the phases is

$$k_G = \frac{G^{(f)}}{G^{(m)}} \tag{4.17}$$

We used the shear modulus ratio of $k_G = 10$ in our examples.

Permeability ratio

The permeability ratio can be calculated from the ratio between the initial susceptibilities of the phases. In our examples, we assume $\mu^{(m)} = 1$.

$$k_\mu = \frac{\mu_r^{(f)}}{\mu_r^{(m)}} \tag{4.18}$$

Initial susceptibility

The initial susceptibility of the material is the ratio between the initial slope of the magnetization vs. the magnetic field curve. In our examples, we assume $\chi^{(m)} = 0$.

$$\chi^{(f)} = \frac{\mu_r^{(f)} - 1}{\mu_r^{(f)}} \tag{4.19}$$

Pressure term

Since the pressure term has the same dimensions of stress, it is normalized with respect to the shear modulus $G^{(m)}$.

$$\bar{p} = \frac{p}{G^{(m)}} \tag{4.20}$$

4.2.4 Constitutive tensors for different materials

The coefficients are derived for the magnetic field oriented along the $\boldsymbol{x}_2$ direction $\boldsymbol{B_0} = (0, B_0, 0)$ stretch λ along the $\boldsymbol{x}_1$ direction, along with the incompressibility condition.

Constitutive tensors for neo-Hookean laminates

Using the neo-Hookean energy function (2.44) and the tensor moduli equations (2.29) and combined with the Euler transformations (2.31), the following non-zero coefficients were derived for neo-Hookean laminates. The non-zero elastic tensor coefficients A_{ijkl} are

$$\mathcal{A}_{1111} = \mathcal{A}_{2121} = G^{(r)}\lambda^2, \tag{4.21}$$

$$\mathcal{A}_{1212} = \mathcal{A}_{2222} = \frac{G^{(r)}}{\lambda^2} \tag{4.22}$$

Constitutive tensors for neo-Hookean laminates with linear magnetic energy models

Using the energy function for the linear magnetic energy model (2.47) and the tensor moduli equations (2.29) and combined with the Euler transformations (2.31), the following non-zero coefficients were derived for neo-Hookean laminates with linear magnetic energy models. The non-zero magnetic tensor coefficients H_{ij} are

$$\mathcal{H}_{11} = \mathcal{H}_{22} = \frac{1}{\mu\mu_0} \tag{4.23}$$

The non-zero magneto-elastic coupling tensor coefficients M_{ijk} are

$$\mathcal{M}_{121} = \mathcal{M}_{211} = \frac{1}{\mu\mu_0\lambda}B^0, \tag{4.24}$$

$$\mathcal{M}_{222} = \frac{2}{\mu\mu_0\lambda}B^0 \tag{4.25}$$

The non-zero elastic tensor coefficients A_{ijkl} are

$$\mathcal{A}_{1111} = \mathcal{A}_{2121} = G^{(r)}\lambda^2, \tag{4.26}$$

$$\mathcal{A}_{1212} = \mathcal{A}_{2222} = \frac{G^{(r)}}{\lambda^2} + \frac{1}{\mu\mu_0\lambda^2}B^{0^2} \tag{4.27}$$

The corresponding pressure term is

$$p = \frac{G^{(r)}}{\lambda^2} + \frac{B^{0^2}}{\lambda^2 \mu_0} \frac{(1-\mu)}{\mu} \tag{4.28}$$

Constitutive tensors for ferromagnetic materials with Langevin's magnetic model

Using the energy function for Langevin's ferromagnetic model (2.56) and the tensor moduli equations (2.29) and combined with the Euler transformations (2.31), the following non-zero coefficients were derived for ferromagnetic materials with Langevin's magnetic model. The non-zero magnetic tensor coefficients H_{ij} are

$$\mathcal{H}_{11} = 1/\mu_0 + \frac{(m_s \mu_0)^2 \lambda^2}{3B^{0^2} \mu_0 \chi} - \frac{m_s \lambda \chi}{B^0} \operatorname{Coth}\left(\frac{3\chi|B|}{\mu_0 m_s}\right), \tag{4.29}$$

$$\mathcal{H}_{22} = 1/\mu_0 - \frac{(m_s \mu_0)^2 \lambda^2}{3B^{0^2} \mu_0 \chi} + 3\frac{\chi}{\mu_0} \left(\operatorname{Csch}\left(\frac{3\chi|B|}{\mu_0 m_s}\right)\right)^2 \tag{4.30}$$

The non-zero magneto-elastic coupling tensor coefficients M_{ijk} are

$$\mathcal{M}_{121} = \mathcal{M}_{211} = \frac{B^0}{\mu_0} \left(\frac{1}{\lambda} + \left(\frac{m_s \mu_0}{B^0}\right)^2 \frac{\lambda}{3\chi} - \left(\frac{m_s \mu_0}{B^0}\right) \coth\left(\frac{3\chi|B|}{\mu_0 m_s}\right)\right), \tag{4.31}$$

$$\mathcal{M}_{222} = \frac{B^0}{\mu_0} \left(\frac{2}{\lambda} - \left(\frac{m_s \mu_0}{B^0}\right)^2 \frac{\lambda}{3\chi} + \frac{3\chi}{\lambda} \left(\operatorname{Csch}\left(\frac{3\chi|B|}{\mu_0 m_s}\right)\right)^2\right) \tag{4.32}$$

The non-zero elastic tensor coefficients A_{ijkl} are

$$\mathcal{A}_{1212} = G^{(r)} \left(\frac{1}{\lambda^2} + \left(\frac{B^{0^2}}{G_m \mu_0}\right) \frac{1}{\lambda^2} + \frac{(m_s \mu_0)^2}{G_m \mu_0} \frac{1}{3\chi} - \left(\frac{B^0}{m_s \mu_0}\right) \frac{(m_s \mu_0)^2}{G_m \mu_0} \frac{\coth\left(\frac{3\chi|B|}{\mu_0 m_s}\right)}{\lambda}\right), \tag{4.33}$$

$$\mathcal{A}_{2222} = G^{(r)} \left(\frac{1}{\lambda^2} + \left(\frac{B^{0^2}}{G^{(r)} \mu_0}\right) \frac{1}{\lambda^2} - \frac{(m_s \mu_0)^2}{G^{(r)} \mu_0} \frac{1}{3\chi} + \left(\frac{B^{0^2}}{G^{(r)} \mu_0}\right) \frac{3\chi}{\lambda^2} \operatorname{Csch}\left[\frac{3\chi|B|}{\mu_0 m_s}\right]\right), \tag{4.34}$$

$$\mathcal{A}_{1111} = \mathcal{A}_{2121} = G^{(r)} \lambda^2 \tag{4.35}$$

The corresponding pressure term is

$$p = \frac{G^{(r)}}{\lambda^2} + \frac{m_s^2 \mu_0}{3\chi} - \frac{B^0 m_s}{\lambda} \coth\left(\frac{3\chi|B|}{m_s \mu_0}\right) \tag{4.36}$$

Constitutive tensors for neo-Hookean laminates with magnetic invariants I_4, I_5 and I_6

The tensor coefficients for the I_4 and I_6 model is calculated using similar methods as the other models. Using the energy function with additional invariants I_4 and I_6 (2.60) and the tensor moduli equations (2.29) and combined with the Euler transformations (2.31), the following non-zero coefficients were derived for neo-Hookean laminates with magnetic invariants I_4, I_5 and I_6. The non-zero magnetic tensor coefficients H_{ij} are

$$\mathcal{H}_{11} = \mathcal{H}_{22} = \frac{1}{\mu\mu_0}\left(\frac{\gamma_0}{\lambda^2} + \gamma_1 + \gamma_2\lambda^2\right) \tag{4.37}$$

The non-zero magneto-elastic coupling tensor coefficients M_{ijk} are

$$\mathcal{M}_{121}(B) = \mathcal{M}_{211}(B) = \frac{1}{\mu\mu_0}B\left(\frac{\gamma_0}{\lambda^2} + \gamma_1 + \gamma_2\lambda^2\right), \tag{4.38}$$

$$\mathcal{M}_{222}(B) = \frac{2}{\mu\mu_0}B\left(\gamma_1 + 2\frac{\gamma_2}{\lambda^2}\right) \tag{4.39}$$

The non-zero elastic tensor coefficients A_{ijkl} are

$$\mathcal{A}_{1111} = G^{(r)}\lambda^2, \tag{4.40}$$

$$\mathcal{A}_{1221} = \mathcal{A}_{2112} = \frac{B^2}{\mu\mu_0}\left(\gamma_2\lambda^2\right), \tag{4.41}$$

$$\mathcal{A}_{2121} = G^{(r)}\lambda^2 + \frac{B^2}{\mu\mu_0}\left(\gamma_2\lambda^2\right), \tag{4.42}$$

$$\mathcal{A}_{1212} = \frac{G^{(r)}}{\lambda^2} + \frac{B^2}{\mu\mu_0}\left(\gamma_1 + \gamma_2\left(\frac{2}{\lambda^2} + \lambda^2\right)\right), \tag{4.43}$$

$$\mathcal{A}_{2222} = \frac{G^{(r)}}{\lambda^2} + \frac{B^2}{\mu\mu_0}\left(\gamma_1 + \frac{6\gamma_2}{\lambda^2}\right) \tag{4.44}$$

The corresponding pressure term is

$$p = \frac{G^{(r)}}{\lambda^2} + \frac{B_0^2}{\lambda^2\mu\mu_0}\left(\gamma_1 + \frac{2\gamma_2}{\lambda^2} - \mu\right) \tag{4.45}$$

4.3 Examples for ferromagnetic energy model and comparison with linear magnetic model

In this section, we illustrate the microscopic analysis through the examples for the laminate MAEs with magnetically inactive matrix (i.e., $\chi^{(m)} = 0$ and $\mu^{(m)} = 1$) and different magnetic behaviors of the stiffer active layer. In the discussion hereafter, we denote the magnetic parameters corresponding to the stiffer active layer without the superscript (f), i.e., $\chi^{(f)} \to \chi$ and $\mu^{(f)} \to \mu$.

4.3.1 Magnetostriction in layered MAEs

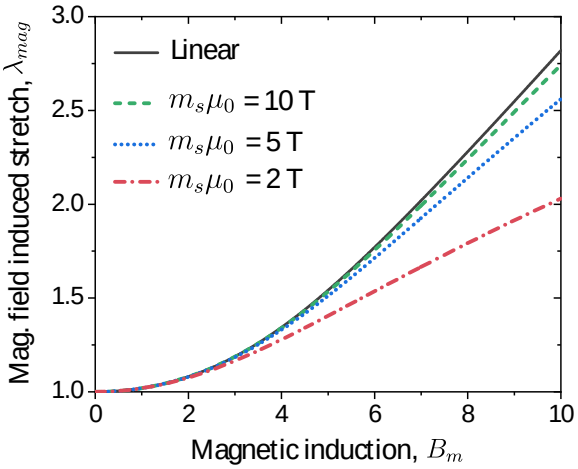

Figure 4.6: Magnetic field-induced stretch $\lambda_{mag} = \lambda_2$ as the function of normalized magnetic induction $B_m = B/\sqrt{G^{(m)}\mu_0}$. MAE with stiff layer's volume fraction $c^{(f)} = 0.4$, initial magnetic susceptibility $\chi = 0.9$, and initial shear modulus contrast $G^{(f)}/G^{(m)} = 10$ are considered.

In this subsection, we analyze the magnetic field-induced deformation in the layered MAEs. In Fig. 4.6, we plot the field-induced stretch as the function of normalized magnetic induction $B_m = B/\sqrt{G^{(m)}\mu_0}$. Here, λ_{mag} is the stretch-induced along the direction of the applied magnetic field ($\mathbf{e}_2$), which is determined using Eq. (3.12) as $\lambda_{mag} = \lambda_2 = \lambda^{-1}$. The results are shown for MAEs with stiff layer volume fraction $c^{(f)} = 0.4$, initial magnetic susceptibility $\chi = 0.9$, and initial shear modulus contrast $G^{(f)}/G^{(m)} = 10$. The black solid curve denotes the response of the MAE with the stiff layer characterized by linear magnetic behavior. For the stiff layer with ferromagnetic behavior, we consider three magnetic saturation values: $m_s\mu_0 = 10$ T (green dashed curve), $m_s\mu_0 = 5$ T (blue dotted curve), and $m_s\mu_0 = 2$ T (red dash-dotted curve).

Clearly, the magnetic field-induced stretch λ_{mag} increases with an increase in the applied magnetic field for both the MAEs with linear magnetic and ferromagnetic behaviors. We observe that MAE with linear magnetic behavior undergoes larger deformations as compared to those with ferromagnetic behavior. For instance, at $B_m = 7$, the induced stretch corresponding to linear magnetic MAE is $\lambda_{mag} = 2.01$, whereas in MAE with $m_s\mu_0 = 2$ T, it is $\lambda_{mag} = 1.66$. Moreover, among the MAEs with ferromagnetic behavior, the stretch λ_{mag} decreases with a decrease in magnetic saturation value. For example, at $B_m = 10$, the magnetic field-induced stretch decreases from $\lambda_{mag} = 2.74$ to $\lambda_{mag} = 2.03$ as magnetic saturation decreases from $m_s\mu_0 = 10$ T to $m_s\mu_0 = 2$ T (see green and red

curves).

The observed dependence of magneto-deformation on $m_s\mu_0$ values is due to the variation in MAE's effective magnetic permeability. In particular, with the decrease in the magnetic saturation values, the effective magnetic permeability also decreases (2.52), leading to an increase in the contribution of magnetic stress into the total stress, Eq. (3.5). However, Maxwell's stress $\boldsymbol{\sigma}_m^*$ does not change with MAE's magnetic properties, and to satisfy the mechanical traction-free boundary conditions, the total stress inside the MAE also remains constant, Eq. (3.6). Therefore, an increase in magnetic stress is compensated by a decrease in mechanical stress. Thus, the MAE undergoes comparatively smaller deformations as the active layer's magnetic saturation value decreases.

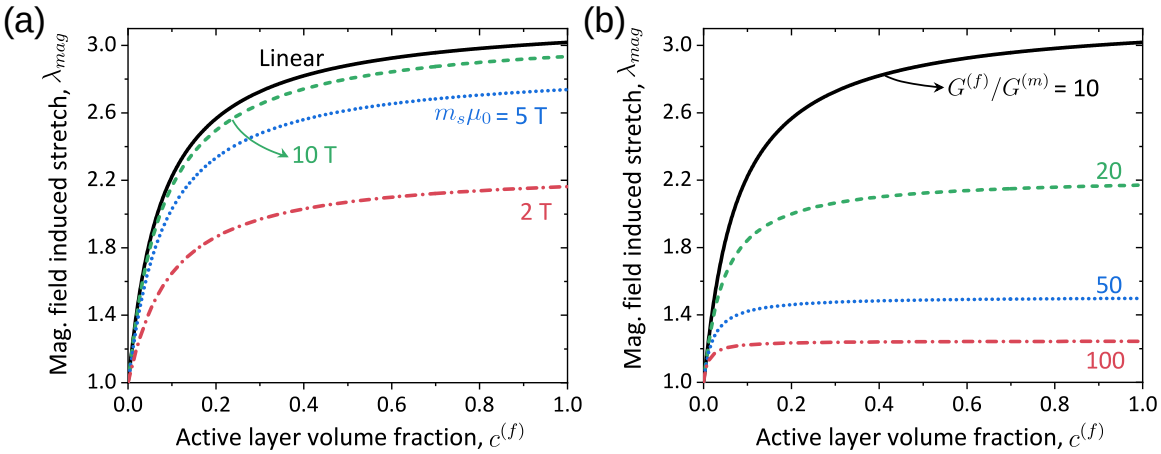

Figure 4.7: Magnetic field induced stretch $\lambda_{mag} = \lambda_2$ as the function of active layer volume fraction $c^{(f)}$. The results are shown for (a) ferromagnetic MAEs with $G^{(f)}/G^{(m)} = 10$ and (b) linear magnetic MAEs with different shear modulus contrast values. MAEs with initial magnetic susceptibility $\chi = 0.9$ are subjected to magnetic field $B_m = 10$.

Next, in Fig. 4.7, we plot the magnetic field-induced stretch as the function of stiff active layer volume fraction $c^{(f)}$. The MAEs with $\chi = 0.9$ are subjected to the magnetic field of magnitude $B_m = 10$. Similar to Fig. 4.6, in Fig. 4.7a, we consider the ferromagnetic MAEs with $G^{(f)}/G^{(m)} = 10$ having different magnetic saturation values. For completeness, we show the results for linear magnetic MAEs with different shear modulus contrasts in Fig. 4.7b.

We observe that the field-induced stretch monotonically increases with an increase in $c^{(f)}$, regardless of MAE's magnetic behavior (see Fig. 4.7a) and shear modulus contrast (see Fig. 4.7b). This is because only the stiff layer contributes to the response of MAEs under the applied magnetic field. Similar to the observations in Fig. 4.6, the induced stretch is higher for linear magnetic behavior, and λ_{mag} decreases with a decrease in

$m_s\mu_0$. As expected, the magnetic field-induced deformation decreases with an increase in shear modulus contrast (see Fig. 4.7b).

4.3.2 Magnetoelastic instabilities in layered MAEs

In this subsection, we analyze the magnetoelastic instabilities in MAEs with bilayered microstructure. First, we investigate the effect of the applied magnetic field B_m on the critical stretch λ_{cr} and wavenumber k_{cr}, and related instability modes. Here, λ_{cr} denotes the critical stretch value (λ_1 along the direction of layers $\mathbf{e}_1$) corresponding to the onset of instability. In the second part of this subsection, we examine the role of phase volume fraction in developing instabilities in MAEs with different magnetic behaviors. In the following examples, we consider the MAEs with initial shear modulus contrast $G^{(f)}/G^{(m)} = 10$.

Effect of magnetic field on magnetoelastic instabilities

We start by illustrating the influence of the applied magnetic field on the stability of MAEs with linear magnetic behavior. Fig. 4.8 shows the critical stretch (a) and normalized critical wavenumbers: k_1^* and k_2^* (b) as the functions of normalized magnetic induction B_m. The wavenumbers are normalized with respect to the period length L in the current configuration (see Fig. 3.1) as $k_1^* = k_1 L$ and $k_2^* = k_2 L$. We consider the MAEs with stiff layer volume fraction $c^{(f)} = 0.6$ and initial magnetic susceptibility $\chi = 0.95$. Here and thereafter, we use solid and dotted curves for macroscopic and microscopic instabilities, respectively (see Fig. 4.8a). Furthermore, solid and dash-dotted curves denote the critical wavenumbers k_1^* and k_2^*, respectively (see Fig. 4.8b).

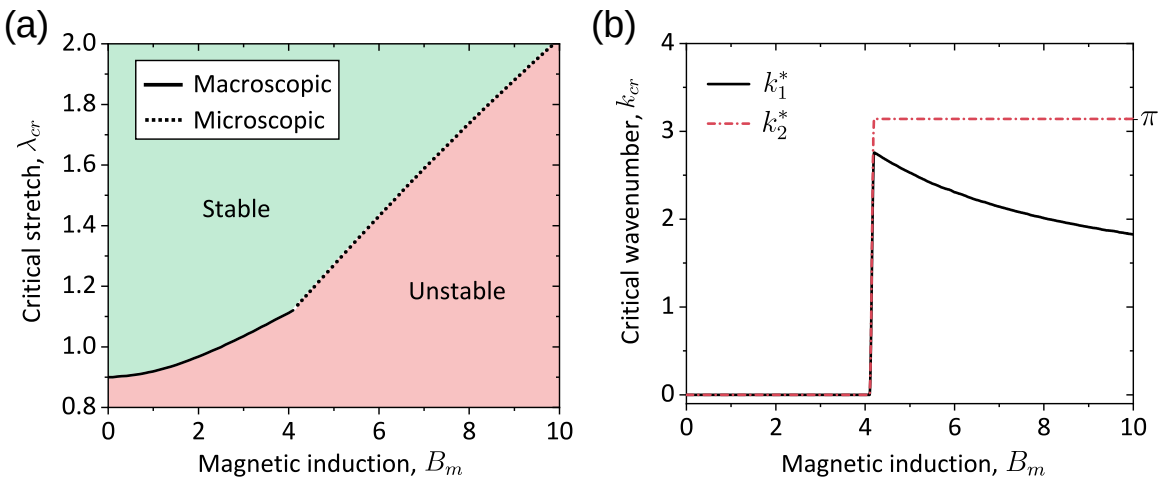

Figure 4.8: Critical stretch λ_{cr} (a) and normalized critical wavenumbers (b) vs. the normalized magnetic field B_m. MAEs with stiff layer's volume fraction $c^{(f)} = 0.6$ and initial magnetic susceptibility $\chi = 0.95$.

We find that the critical stretch increases with an increase in the applied magnetic field. Furthermore, we observe that when the MAE is subjected to a smaller magnetic field ($B_m \leq 2.5$), it develops instabilities under compressive strains ($\lambda_{cr} < 1$). Interestingly, at higher magnetic fields, MAE is unstable even under tensile strains. For example, the MAE is unstable for $\lambda < 1.59$, when subjected to $B_m = 7$. Moreover, we find that the instability mode switches at a certain threshold magnitude of magnetic induction B_m^{th}. In particular, macroscopic instability appears for $B_m < B_m^{th}$, whereas microscopic instability emerges for $B_m > B_m^{th}$. For the considered MAE, the threshold value is $B_m^{th} = 4.1$.

The transition in the instability mode is also evident from the evolution of the critical wavenumbers (k_1^* and k_2^*) with the magnetic field (see Fig. 4.8b). For $B_m > B_m^{th}$, the wavenumbers have finite non-zero values, hence, representing the microscopic instability. In particular, the MAEs develop an antisymmetric mode of microscopic instability, as the critical wavenumber $k_2^* = \pi$, when subjected to this range of magnetic field values (see. Fig. 4.8b). Moreover, we find that the wavenumber k_1^* monotonically decreases with an increase in B_m, hence, showing the tunability of buckling patterns with an applied magnetic field. For magnetic induction magnitudes smaller than B_m^{th}, both the critical wavenumbers (k_1^* and k_2^*) approach zero, $k_{cr} \to 0$, showing the long-wave or macroscopic loss of stability.

Effect of ferromagnetic behavior on the magnetoelastic instabilities

Next, we investigate the development of magnetoelastic instabilities in MAEs with ferromagnetic behavior. Fig. 4.9 shows the critical stretch (a),(c), and critical wavenumbers (b),(d) as functions of B_m for MAEs with $\chi = 0.95$. The results are shown for MAEs with stiff layer volume fractions: $c^{(f)} = 0.4$ (Fig. 4.9a and b) and (Fig. 4.9c and d). We consider the MAEs with magnetic saturation values: $m_s\mu_0 = 10$ T (blue curves), $m_s\mu_0 = 5$ T (red curves), and $m_s\mu_0 = 2$ T (green curves). The results for MAEs with the linear magnetic behavior are included for comparison (black curves).

Similar to MAEs with linear magnetic behavior, the MAEs with ferromagnetic behavior also develop instabilities at higher stretches when subjected to higher magnetic fields. However, we observe that the critical stretch at a particular magnetic induction magnitude decreases with a decrease in the MAE magnetic saturation value. For example, in MAEs with $c^{(f)} = 0.4$ at $B_m = 8$, the critical stretches (with corresponding magnetic saturation values) are $\lambda_{cr} = 1.55$ ($m_s\mu_0 = 10$ T), $\lambda_{cr} = 1.22$ ($m_s\mu_0 = 5$ T), and $\lambda_{cr} = 0.96$ ($m_s\mu_0 = 2$ T); for linear magnetic behavior, $\lambda_{cr} = 1.88$. Moreover, the critical stretches of MAEs with smaller magnetic saturation values, for example, $m_s\mu_0 = 5$ T and $m_s\mu_0 = 2$ T, approach a saturation value at higher values of B_m (see the red and green curves in Fig. 4.9a and c). These observations hold regardless of the volume fraction of phases.

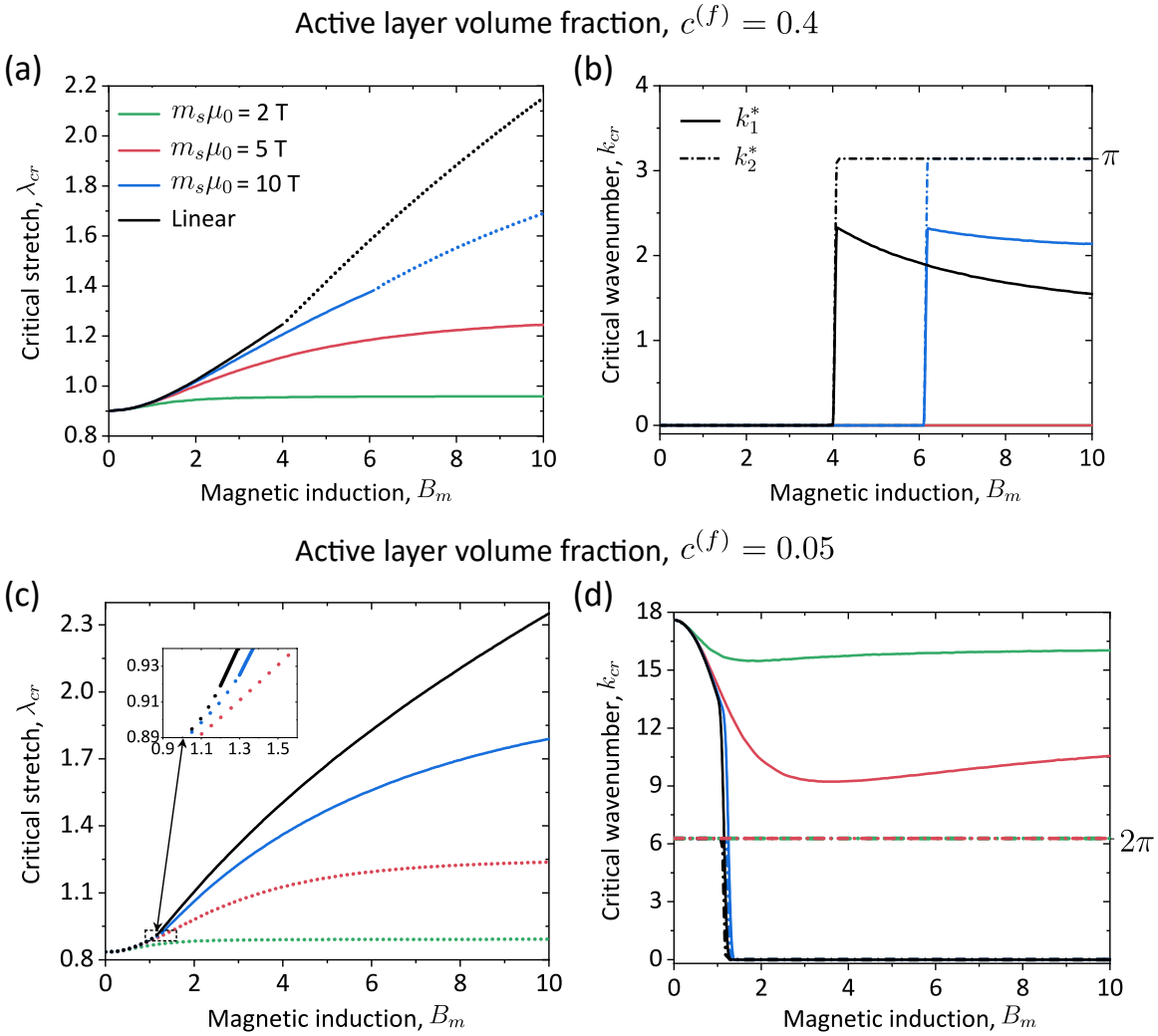

Figure 4.9: Critical stretch λ_{cr} (a),(c), and normalized critical wavenumbers (b),(d) vs. the normalized magnetic field B_m. MAEs with stiff layer's initial magnetic susceptibility $\chi = 0.95$ and volume fractions: $c^{(f)} = 0.4$ (a),(b) and $c^{(f)} = 0.05$ (c),(d) are considered.

The effect of the applied magnetic field on the buckling patterns and instability modes strongly depends on the stiff layer volume fraction and its magnetic behavior. First, consider the MAEs with a high stiff layer volume fraction, $c^{(f)} = 0.4$. We observe that in these MAEs, the threshold magnetic induction B_m^{th}, at which the instability mode switches, increases with a decrease in $m_s\mu_0$. Thus, the MAEs composites with lower magnetic saturations favor the long instability over the microscopic one. For the considered MAEs, the transition occurs at $B_m^{th} = 4$ (linear) and $B_m^{th} = 6.1$ ($m_s\mu_0 = 10$ T). Interestingly, the MAEs with magnetic saturation values $m_s\mu_0 = 5$ T and $m_s\mu_0 = 2$ T do not show any transition in the considered range of B_m, and develop macroscopic instabilities. We find

that the MAEs with $c^{(f)} = 0.4$ develop the antisymmetric mode of microscopic instabilities ($k_2^* = \pi$), for both magnetic behaviors. However, the wavelength of the buckling pattern is smaller (higher k_1^*) in MAEs with the ferromagnetic behavior as compared to linear ones when they are to develop microscopic instabilities (see the black and blue curves in Fig. 4.9b).

Effect of volume fractions on the magnetoelastic instabilities

The MAEs with smaller volume fraction, $c^{(f)} = 0.05$, develop microscopic instabilities when subjected to smaller magnitudes of the magnetic field. The instability mode switches to macroscopic at magnitudes $B_m > B_m^{th}$ (see Fig. 4.9c and d). Moreover, the threshold magnitude B_m^{th} increases with a decrease in $m_s\mu_0$ (see inset in Fig. 4.9c). However, for smaller magnetic saturation values, $m_s\mu_0 = 5$ T and $m_s\mu_0 = 2$ T, the transition in the instability mode does not occur in the considered range of the applied magnetic field. Hence, as opposed to MAEs with high volume fractions ($c^{(f)} = 0.4$), in MAEs with $c^{(f)} = 0.05$, a decrease in magnetic saturation values promotes microscopic (or finite-wavelength) instabilities. Moreover, these MAEs develop the symmetric mode of microscopic instability, with the critical wavenumber $k_2^* = 2\pi$ (see the dash-dotted curves in Fig. 4.9d).

The results indicate that in addition to the influence of the applied magnetic field and phase magnetic behavior, the instability development and associated buckling patterns significantly depend on the volume fraction of layers. See sec. 4.3.2 for details.

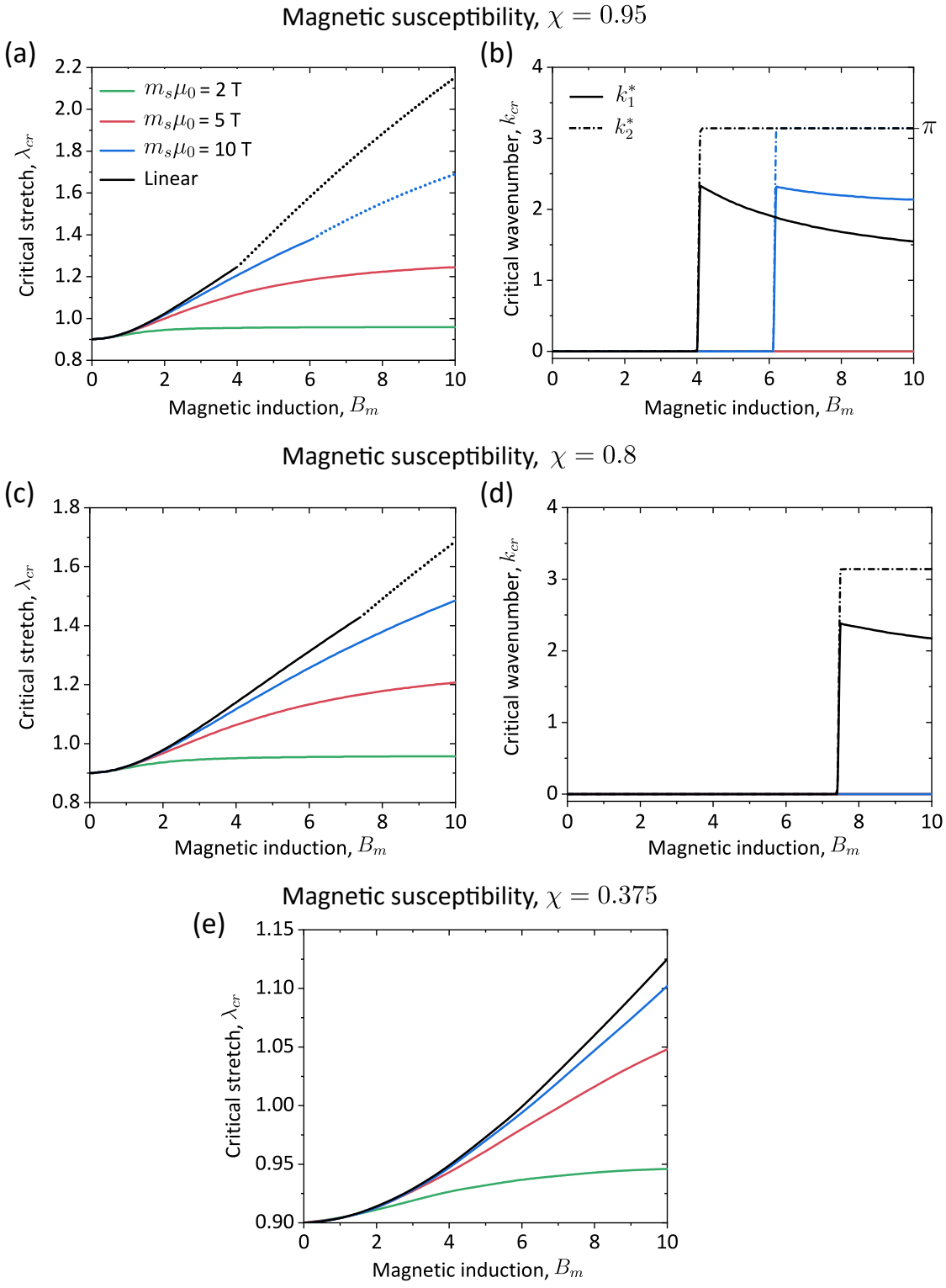

Figure 4.10: Critical stretch λ_{cr} (a),(c),(e) and normalized critical wavenumbers (b),(d) vs. the normalized magnetic field B_m. MAEs with stiff layer's volume fraction $c^{(f)} = 0.4$ and initial magnetic susceptibilities: $\chi = 0.95$ (a), (b); $\chi = 0.80$ (c), (d); and $\chi = 0.375$ (e) are considered.

Effect of initial magnetic susceptibility on the magnetoelastic instabilities

Next, we study the influence of initial magnetic susceptibility on the magnetoelastic instabilities in the ferromagnetic layered MAEs. To this end, in Fig. 4.10, we show the critical parameters corresponding to MAEs with initial magnetic susceptibilities: $\chi = 0.95$ (a), (b); $\chi = 0.80$ (c), (d); and $\chi = 0.375$ (e). The results are shown for MAEs with stiff layer volume fraction $c^{(f)} = 0.4$.

The critical stretch decreases with a decrease in the initial magnetic susceptibility; this is observed for all magnetic saturation values. For instance, the critical stretch at $B_m = 10$ corresponding to MAEs with $m_s\mu_0 = 10$ T decreases from $\lambda_{cr} = 1.69$ to $\lambda_{cr} = 1.10$ as susceptibility varies from $\chi = 0.95$ to $\chi = 0.375$ (compare the blue curves in Fig. 4.10a and e). Moreover, the critical wavenumber k_1^* increases with a decrease in χ, in the MAEs that develop microscopic instabilities. We note that the effect of initial magnetic susceptibility on the critical parameters, λ_{cr} and k_{cr}, is similar to that observed in the case of magnetic saturation values (see Fig. 4.9a and b). This is because a decrease in magnetic saturation and/or initial magnetic susceptibility values leads to a decrease in MAE's magnetization and vice-versa at a given magnetic field magnitude.

The initial magnetic susceptibility also significantly influences the instability mode in the MAEs. In particular, lower values of χ favor the occurrence of macroscopic instabilities in MAEs. For instance, in the linear magnetic MAEs, the threshold magnetic induction, at which the instability mode switches, increases from $B_m^{th} = 4$ to $B_m^{th} = 7.4$ as susceptibility changes from $\chi = 0.95$ to $\chi = 0.80$. For further smaller magnetic susceptibilities, for example, $\chi = 0.375$, no transition in the instability mode is observed, and the MAEs develop macroscopic instabilities, regardless of their magnetic behavior (see Fig. 4.10e).

Effect of volume fraction of phases on magnetoelastic instabilities

Here, we study the effect of the phase volume fraction on the magnetoelastic instabilities. First, we examine the linear magnetic MAEs with $\chi = 0.95$. In Fig. 4.11, we plot the critical stretch (a) and wavenumber (b) as the functions of stiff layer volume fraction $c^{(f)}$. We consider the MAEs subjected to $B_m = 1$ (blue curves), $B_m = 5$ (green curves), and $B_m = 10$ (red curves). For the sake of convenient discussion, in Fig. 4.11a, we have marked the first and second instability mode transition points as 'S' and 'A', respectively. In particular, 'S' represents the switch from *symmetric* microscopic instability mode to macroscopic, whereas 'A' denotes the transition from macroscopic to *antisymmetric* microscopic instability, with an increase in $c^{(f)}$.

For the MAEs subjected to smaller magnetic field levels, for example, $B_m = 1$, the critical stretch increases with an increase in $c^{(f)}$ up to a certain value; beyond that volume

fraction value, the critical stretch decreases with a further increase in the volume fraction. Moreover, when the stiff layer volume fraction is smaller than a particular threshold value, $c_{th}^{(f)}$, the MAEs develop symmetric microscopic buckling modes ($k_2^* = 2\pi$). However, at higher values of $c^{(f)}$, a macroscopic loss of stability occurs. We also observe that the wavelength of the buckling pattern increases (k_1^* decreases) with an increase in $c^{(f)}$, and it approaches the long-wave limit ($k_1^* \to 0$) for $c^{(f)} \geq c_{th}^{(f)}$. The corresponding threshold value is $c_{th}^{(f)} = 0.07$, which is marked as 'S' on the blue curve (see Fig. 4.11a). We note that a similar variation of critical parameters with stiff layer volume fraction has also been reported for layered composites subjected to purely mechanical loadings Slesarenko and Rudykh (2017).

Effect of higher magnetic induction values in volume fraction

However, MAEs subjected to higher magnetic induction values show contrastingly different instability mode transitions and highly non-monotonous variation of critical parameters. For example, consider the MAEs under $B_m = 5$; these MAEs, similar to MAE under $B_m = 1$, also show the first transition 'S' in the instability mode. Interestingly, these MAEs undergo an additional transition, back to microscopic instability, at higher values of $c^{(f)}$; this shift in the instability mode is marked as 'A' on the green curve in Fig. 4.11a. Both transitions are also evident from the evolution of critical wavenumbers with stiff layer volume fraction (see the green curves in Fig. 4.11b). Furthermore, we observe that in the MAEs developing microscopic instabilities, the critical wavelength significantly varies with the volume fraction. This high tunability of wavelength (or k_1^*) is very pronounced in the vicinity of the extreme volume fraction values, i.e., $c^{(f)} \to 0$ and $c^{(f)} \to 1$ (see Fig. 4.11b).

Remarkably, the morphologies of MAEs that are to develop microscopic instabilities, can exhibit antisymmetric and symmetric instability modes – with distinct values for critical wavenumber k_2^*, dictated by the stiff layer volume fraction. In particular, MAEs with $c^{(f)}$ smaller than that corresponding to the first transition point 'S', i.e., $c^{(f)} < c_{th_I}^{(f)}$, has $k_2^* = 2\pi$. However, for stiff layer volume fraction higher than that of 'A', $c^{(f)} > c_{th_{II}}^{(f)}$, has $k_2^* = \pi$ (see green dash-dotted curve). Similar behavior is observed for MAEs subjected to $B_m = 10$ (see the red curves). Thus, at high magnetic field magnitudes, MAEs with smaller $c^{(f)}$ develop *symmetric* mode of microscopic instability, long-wave instability emerges at moderate values of $c^{(f)}$, and microscopic instability with *antisymmetric* buckling pattern arises at higher stiff layer volume fractions.

The threshold stiff layer volume fractions for both transition points decrease with an increase in the magnitude of the applied magnetic field. For example, the threshold $c^{(f)}$ corresponding to the 'S' transition point decreases from $c_{th}^{(f)} = 0.07$ to $c_{th}^{(f)} = 0.04$ as the

applied magnetic field changes from $B_m = 1$ to $B_m = 5$. Moreover, the threshold values for 'A' decreases from $c_{th}^{(f)} = 0.25$ (at $B_m = 5$) to $c_{th}^{(f)} = 0.14$ (at $B_m = 10$). Hence, the application of a strong magnetic field favors the occurrence of the antisymmetric mode of microscopic instability.

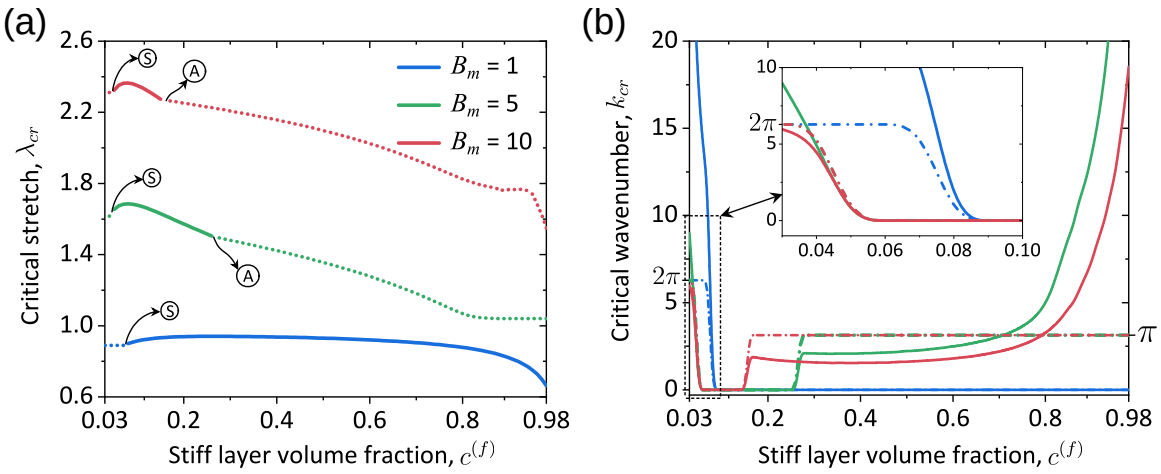

Figure 4.11: Critical stretch λ_{cr} (a) and normalized critical wavenumbers (b) vs. the stiff layer volume fraction $c^{(f)}$. Linear magnetic MAEs with $\chi = 0.95$ are subjected to $B_m = 1$, $B_m = 5$, and $B_m = 10$.

Effect of ferromagnetic behavior on volume fraction vs λ_{cr}

Next, we study the effect of volume fraction in MAEs with ferromagnetic behavior. Fig. 4.12 shows the critical stretch (a) and critical wave numbers (b) versus stiff layer volume fraction for the MAEs with magnetic saturation values $m_s\mu_0 = 10$ T (blue curves) and $m_s\mu_0 = 5$ T (red curves). We consider the MAEs with $\chi = 0.95$ subjected to magnetic induction $B_m = 10$. The results for the linear magnetic MAEs are denoted by the black curves and are added for comparison.

We observe that the instability in ferromagnetic MAEs develops at smaller stretches than in their linear magnetic counterparts. Among the ferromagnetic MAEs, the lesser the magnetic saturation value, the smaller is the critical stretch. Moreover, the critical wavelength (wavenumber) decreases (increases) with a decrease in $m_s\mu_0$. These findings are consistent with the previous observations in Fig. 4.9. Similar to the linear magnetic MAEs, ferromagnetic MAEs also offer a high tunability of the critical wavenumber k_1^*, especially in the vicinity of the extreme volume fraction values (see Fig. 4.12b).

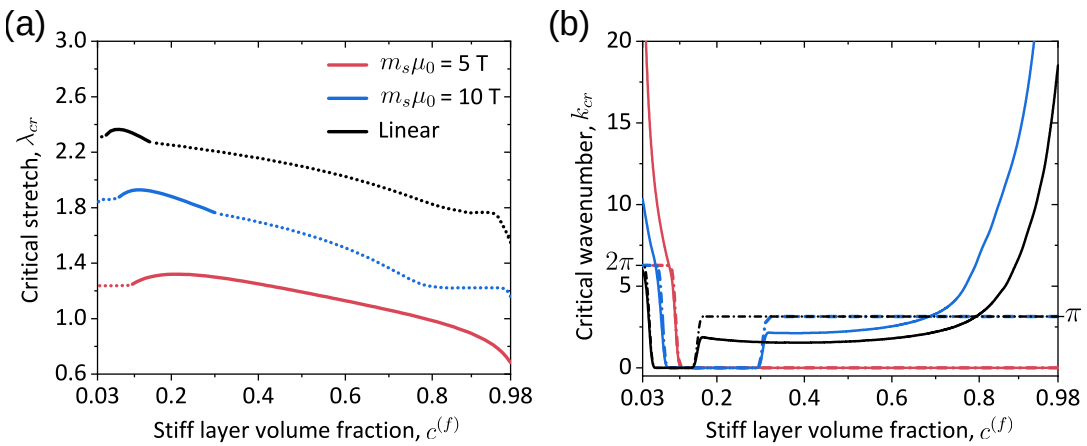

Figure 4.12: Critical stretch λ_{cr} (a) and normalized critical wavenumbers (b) vs. the stiff layer volume fraction $c^{(f)}$. Linear magnetic MAEs with $\chi = 0.95$ are subjected to $B_m = 10$. The results are shown for ferromagnetic MAEs with $m_s\mu_0 = 5$ T and $m_s\mu_0 = 10$ T, together with linear magnetic MAEs.

Comparing the critical parameters of ferromagnetic MAEs (Fig. 4.12) with those of linear magnetic MAEs (in Fig. 4.11), we find that a decrease in the magnetic field magnitude (in linear MAEs) has a similar influence as decreasing the magnetic saturation value (in ferromagnetic MAEs under a constant magnetic field). This occurs because of the magnetic saturation effect present in the ferromagnetic MAEs. In particular, the saturation effect takes place at smaller magnetic fields in MAEs with small saturation values. Therefore, when subjected to higher values of B_m, the influence of the applied magnetic field on the magnetoelastic tensors of ferromagnetic MAEs is significantly weaker than that in their magnetically linear counterparts.

The transition of instability modes also demonstrates the behavior resembling that in Fig. 4.11. For instance, MAEs with smaller saturation values ($m_s\mu_0 = 5$ T) have only the first transition point 'S', whereas MAEs with higher saturation value ($m_s\mu_0 = 10$ T) show two transitions. Moreover, the threshold values corresponding to the transitions decrease with an increase in $m_s\mu_0$. For example, the 'A' transition occurs at $c^{(f)} = 0.3$ (for $m_s\mu_0 = 10$ T) and $c^{(f)} = 0.15$ (for linear magnetic). The 'S' transition in MAEs with $m_s\mu_0 = 5$ T and $m_s\mu_0 = 10$ T occurs at $c^{(f)} = 0.1$ and $c^{(f)} = 0.07$, respectively. Hence, the MAEs with smaller values of $m_s\mu_0$ are less likely to develop antisymmetric microscopic instabilities.

Effect of initial magnetic susceptibilities $\chi^{(f)}$ on volume fraction $c^{(f)}$ vs critical strech λ_{cr}

Here, we illustrate the influence of the initial magnetic susceptibilities on the critical parameters and instability mode transition with phase volume fraction. Fig. 4.13 shows the critical parameters for linear magnetic MAEs with $\chi = 0.95$ (black curves), $\chi = 0.80$ (blue curves), and $\chi = 0.375$ (red curves). We consider the MAEs subjected to magnetic inductions $B_m = 1$ (Fig. 4.13a and b), $B_m = 5$ (Fig. 4.13c and d), and $B_m = 10$ (Fig. 4.13e and f).

Consistent with the findings in Fig. 4.10, we observe that the MAEs with lower values of χ develop instabilities at smaller stretch levels. Moreover, the critical wavenumber k_1^* decreases with an increase in χ, in the MAEs that develop microscopic instabilities. This holds independent of the magnitude of magnetic induction.

The interplay between the instability modes is also dictated by the magnetic susceptibility of the MAEs. In particular, we observe that the threshold value corresponding to the transition point 'S' increases with a decrease in χ, irrespective of the magnetic field's magnitude. For example, under $B_m = 5$, the transition 'S' occurs at $c^{(f)} = 0.04$ (for $\chi = 0.95$), $c^{(f)} = 0.07$ (for $\chi = 0.80$), and $c^{(f)} = 0.13$ (for $\chi = 0.375$). Moreover, we find that the occurrence of the second switch in instability mode with $c^{(f)}$ depends on the value of χ, together with the magnetic field. For instance, 'A' transition point is not observed for any of the MAEs subjected to $B_m = 1$. Under $B_m = 5$, however, 'A' transition only takes place for MAEs with $\chi = 0.95$. For MAEs subjected to $B_m = 10$, the second switch in instability mode is observed for $\chi = 0.95$ and $\chi = 0.8$. Similar to 'S' instability transition, for 'A' transition, the threshold volume fraction increases with a decrease in χ. For example, the corresponding threshold values for MAEs under $B_m = 10$ are $c^{(f)} = 0.15$ (for $\chi = 0.95$) and $c^{(f)} = 0.32$ (for $\chi = 0.80$).

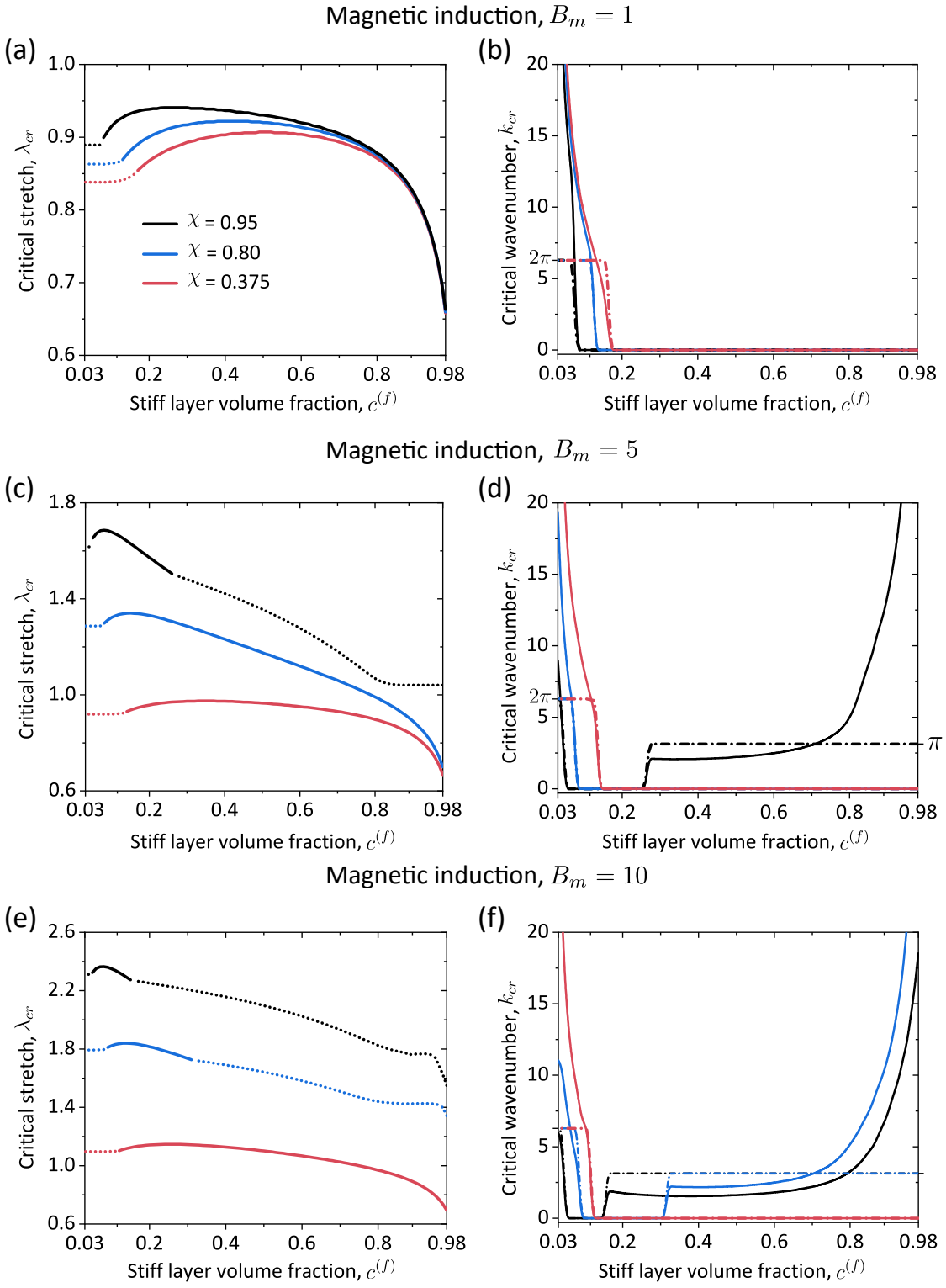

Figure 4.13: Critical stretch λ_{cr} (a),(c),(e) and normalized critical wavenumbers (b),(d),(f) vs. the stiff layer volume fraction $c^{(f)}$. Linear magnetic MAEs with initial magnetic susceptibilities $\chi = 0.95$, $\chi = 0.80$, and $\chi = 0.375$ are subjected to $B_m = 1$ (a), (b); $B_m = 5$ (c), (d); and $B_m = 10$ (e), (f).

4.4 Examples of energy models with additional invariants I_4 and I_6

In this subsection, we analyze how invariants I_4 and I_6 can affect the results of the instability analysis. We illustrate the analysis through the examples and discuss the effects of the invariants I_4 and I_6 along with invariant I_5. We examine the role of initial susceptibility and volume fractions in developing instabilities in MAEs with different γ_0, γ_1, and γ_2 coefficients. According to (2.62) the sum of the gamma coefficients must sum to unity. In the following examples, we consider the MAEs with initial shear modulus contrast $k_G = 10$.

4.5 Effect of γ_0 variation on magnetoelastic instabilities

Here, we study the morphologies of λ_{cr} and k_{1cr} as a function of the magnetic field B_m. We have parameterized the curves with γ_0 and γ_1 coefficients ranging from $\gamma_0 = -0.2$ to $\gamma_0 = 0.2$ and $\gamma_1 = 0.8$ to $\gamma_1 = 1.2$. We examine the linear magnetic MAEs with fiber susceptibility of $\chi = 0.8$ and $c^{(f)} = 0.8$, where all the transitions would be present and clearly visible. The constraints, $\gamma_2 = 0$ and $\gamma_0 + \gamma_1 = 1$ hold throughout this section. Here, the default values for which this system becomes identical to the linear magnetic model are $\gamma_0 = 0$ and $\gamma_1 = 1$. In Fig. 4.14, we plot the critical stretch (a) and wavenumber (b) as the functions of the magnetic field B_m. For the sake of convenient discussion, we have marked the symmetric macroscopic and anti-symmetric microscopic instability modes with solid $(-)$ and dashed lines (- -), respectively.

We observe that for smaller magnetic fields $B_m < 1$, the effects of the additional invariants on λ_{cr} were negligible. This is seen from the plot Fig. 4.14 as all $\lambda_{cr} \to 0.85$ for all γ_0 values. This was expected as the invariant terms contribute to the stability only when a magnetic field is present.

Moreover, the increase in γ_0 from $\gamma_0 = -0.2$ to $\gamma_0 = 0.2$ also impacted the transition behavior, as can be seen from Fig. 4.14b. The transitions from macroscopic to microscopic were observed from $B_m = 6$ to $B_m = 7$. As γ_0 increased, the B_m for the transitions in k_{1cr} decreased from $B_m = 6.8$ to $B_m = 6$, while the wavenumber k_{1cr} at the transitions increased from $k_{1cr} = 7.2$ to $k_{1cr} = 8.2$.

Before transitions, the critical stretch in the macroscopic region remained relatively unaffected by changes in γ_0. This can be seen in the exploded view from Fig. 4.14a, where before the transitions, the critical stretch was decreasing from $\lambda_{cr} = 1.02$ to $\lambda_{cr} = 1.04$. In contrast, after the transitions, the critical stretch in the microscopic region was slightly affected by the changes in γ_0 and increased with an increase in γ_0. The critical stretch increased from $\lambda_{cr} = 1.08$ to $\lambda_{cr} = 1.13$. The variation in λ_{cr} ($\Delta\lambda_{cr} = \lambda_{max} - \lambda_{min}$), which

is the difference between the min and max curves, also increased from $\Delta\lambda_{cr} = 0.025$, while after transitions this variation increased to $\Delta\lambda_{cr} = 0.05$.

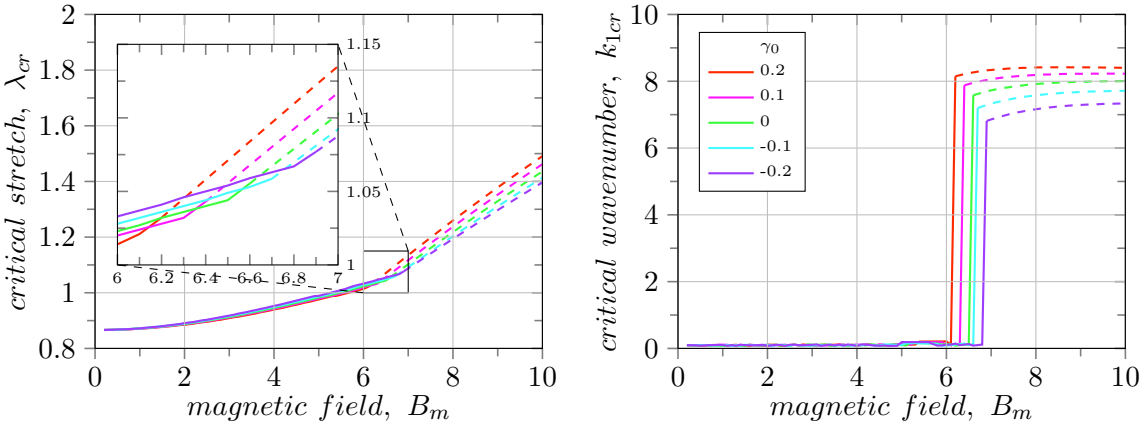

(a) λ_{cr} vs B_m (b) k_{1cr} vs B_m

Figure 4.14: Critical stretch λ_{cr} (a) and normalized critical wave numbers k_1 (b) vs. the normalized magnetic field B_m, for different γ_0 ranging from $\gamma_0 = -0.2$ to $\gamma_0 = 0.2$ values keeping $\gamma_2 = 0$. MAEs with stiff layer's volume fraction $c^{(f)} = 0.8$ and initial magnetic susceptibility $\chi = 0.8$ and the linear magnetic model

4.5.1 Effect of changing volume fraction on the critical stretch ratio vs. the magnetic field

Next, we study the effect of changing the volume fraction on the critical stretch ratio vs. the magnetic field under different parameterizations of γ_0. In Fig. 4.15, the critical stretch λ_{cr} are plotted in (a),(c),(e) while the critical wave numbers k_{1cr} are plotted in (b),(d),(f). Both curves are plotted as a function of the magnetic field on the x-axis. Each of the cases for Fig. 4.14 was simulated for different volume fractions from $c^{(f)} = 0.4$ to $c^{(f)} = 0.8$, while keeping $\gamma_2 = 0$ as constant.

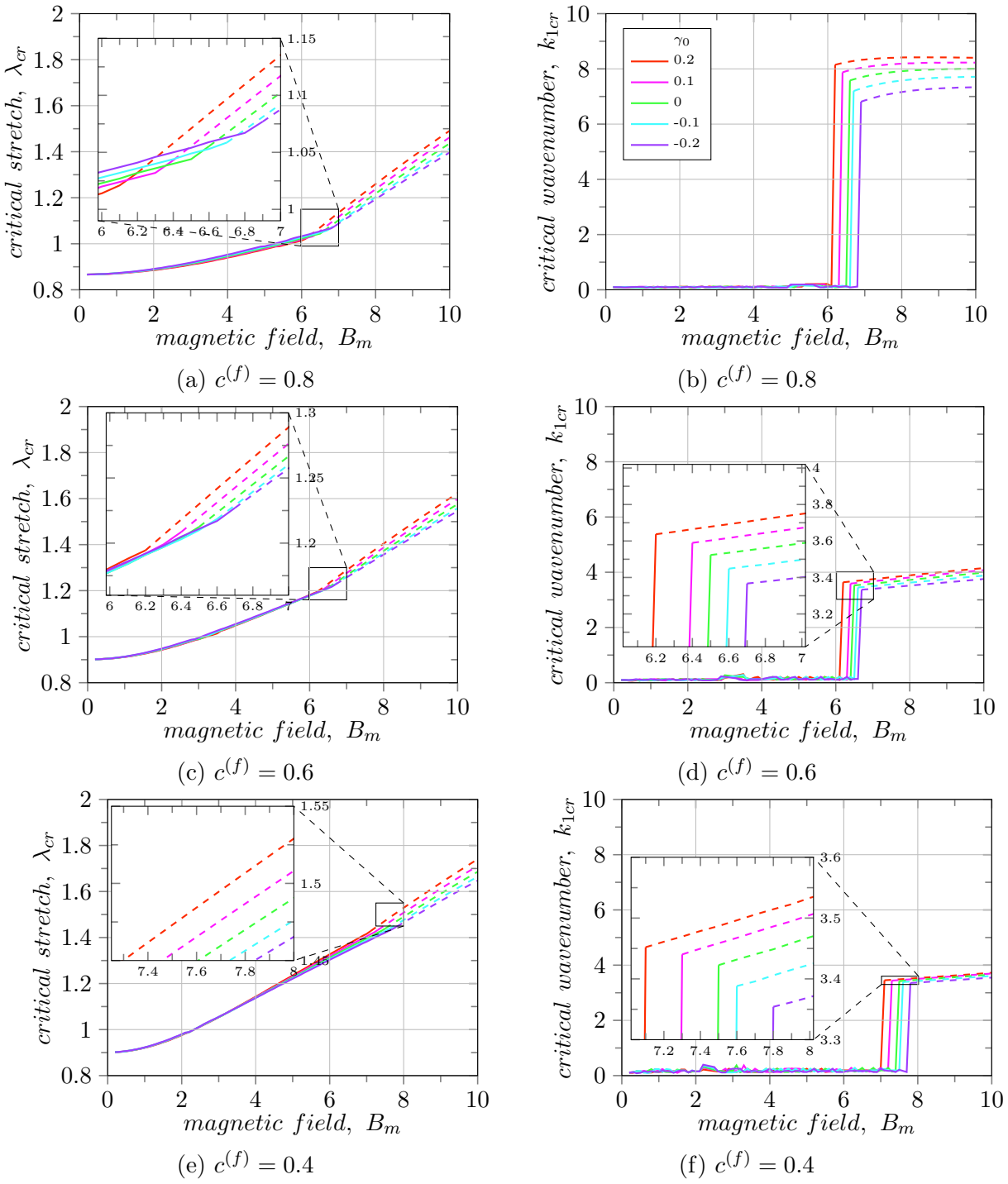

(a) $c^{(f)} = 0.8$ (b) $c^{(f)} = 0.8$

(c) $c^{(f)} = 0.6$ (d) $c^{(f)} = 0.6$

(e) $c^{(f)} = 0.4$ (f) $c^{(f)} = 0.4$

Figure 4.15: Critical stretch λ_{cr} (a),(c),(e) and normalized critical wavenumbers k_1 (b),(d),(f) both plotted against the magnetic field B_m. MAEs with $\chi = 0.8$ and fiber layer's volume fraction $c^{(f)} = 0.8$(a),(b); $c^{(f)}$=0.6(c),(d); $c^{(f)}$=0.4 (e),(d) are used as specifications. The curves are considered for different γ_0 values raging from $\gamma_0 = 0.2$ to $\gamma_0 = -0.2$ keeping $\gamma_2 = 0$

As the volume fraction of the fiber decreased from $c^{(f)} = 0.8$ to $c^{(f)} = 0.4$, the effect of changes in γ_0 remained almost the same, with some decrease in the mid-range volume fraction at $c^{(f)} = 0.6$. This can be seen from the comparison of the transition region spread in zoom view of λ_{cr} values in Fig. 4.15 (a) vs. (c); the λ_{cr} range decreased from $\lambda_{cr} = 1.08$ to 1.13 to $\lambda_{cr} = 1.26$ to $\lambda_{cr} = 1.29$ and then increased again to $\lambda_{cr} = 1.48$ to $\lambda_{cr} = 1.53$. The transition magnetic field region also increased from $B_m \in [6, 7]$ at $c^{(f)} = 0.8$ to $B_m \in [7, 8]$ at $c^{(f)} = 0.4$ (See Figs. 4.15 (b),(f)). And the average critical wave number k_{1cr} decreased from 8 to 4 and the variation in k_{1cr} also decreased from $\Delta k_{1cr} = 1$ to $\Delta k_{1cr} = 0.2$.

4.5.2 Effect of initial susceptibility χ and volume fraction $c^{(f)}$ variation on the critical ratio λ_{cr} characteristics

In this section, we study the effects of changing the initial susceptibility χ and volume fraction $c^{(f)}$ on the critical stretch λ_{cr} vs. magnetic field B_m, along with changing γ_0. In Fig. 4.16, λ_{cr} is plotted as a function of the magnetic field, and each of the cases was simulated for different χ values ranging from $\chi = 0.375$ to $\chi = 0.95$ and different mid-range volume fractions from $c^{(f)} = 0.8$ to $c^{(f)} = 0.2$. The corresponding μ_r values are $\mu_r = 1.6$, $\mu_r = 5$ and $\mu_r = 20$ respectively.

From the results in Fig. 4.16, we observe that the initial susceptibility χ plays a more significant role in reducing the effects of γ_0 variations than variations in the volume fraction. We observe that for higher $\chi = 0.95$, the variation in the different curves for λ_{cr} for γ_0 becomes negligible. i.e., $\Delta\lambda_{cr}$ decreases roughly from an average in the order of 0.2 to 0.02 for all the mid-range volume fractions $c^{(f)} \in [0.2, 0.8]$ as χ increases from $\chi = 0.375$ to 0.95. Moreover, at high initial susceptibility, the variation in the transition points is also lost for almost all values of $\gamma_0 \in [-0.2, 0.2]$. For e.g., at $c^{(f)} = 0.8$ (see Fig. 4.16 (c)), the transition point for λ_{cr} vs. B_m is $(4.8, 1)$ for all values of γ_0 and this same trend is observed for rest of the volume fractions till $c^{(f)} = 0.4$ at high susceptibility of $\chi = 0.95$. At low volume fractions $c^{(f)} = 0.2$, we begin to see a small variation in λ_{cr} and k_{1cr} (see Fig. 4.16 (l)). Thus higher initial susceptibility χ reduces the effect of the γ_0 coefficients on the magnetic field $\mathbf{B}$ vs k_{1cr} and λ_{cr} relationships.

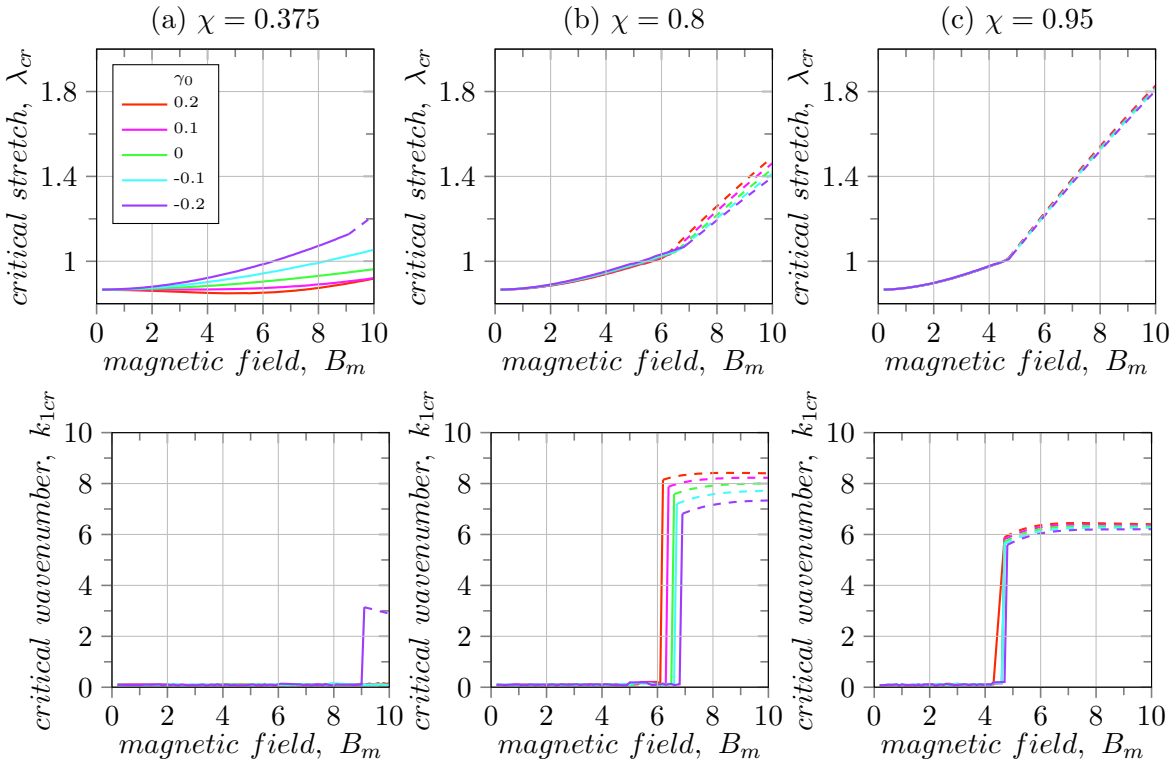

Volume fraction, $c^{(f)} = 0.8$

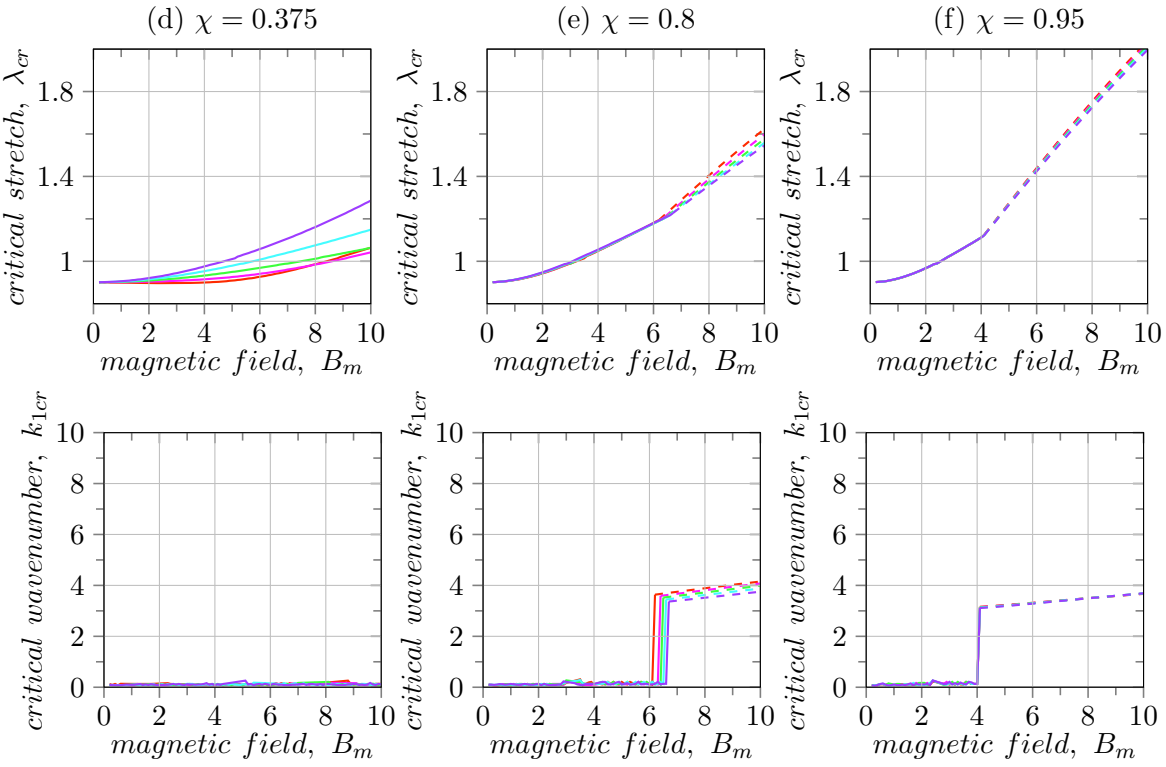

Volume fraction, $c^{(f)} = 0.6$

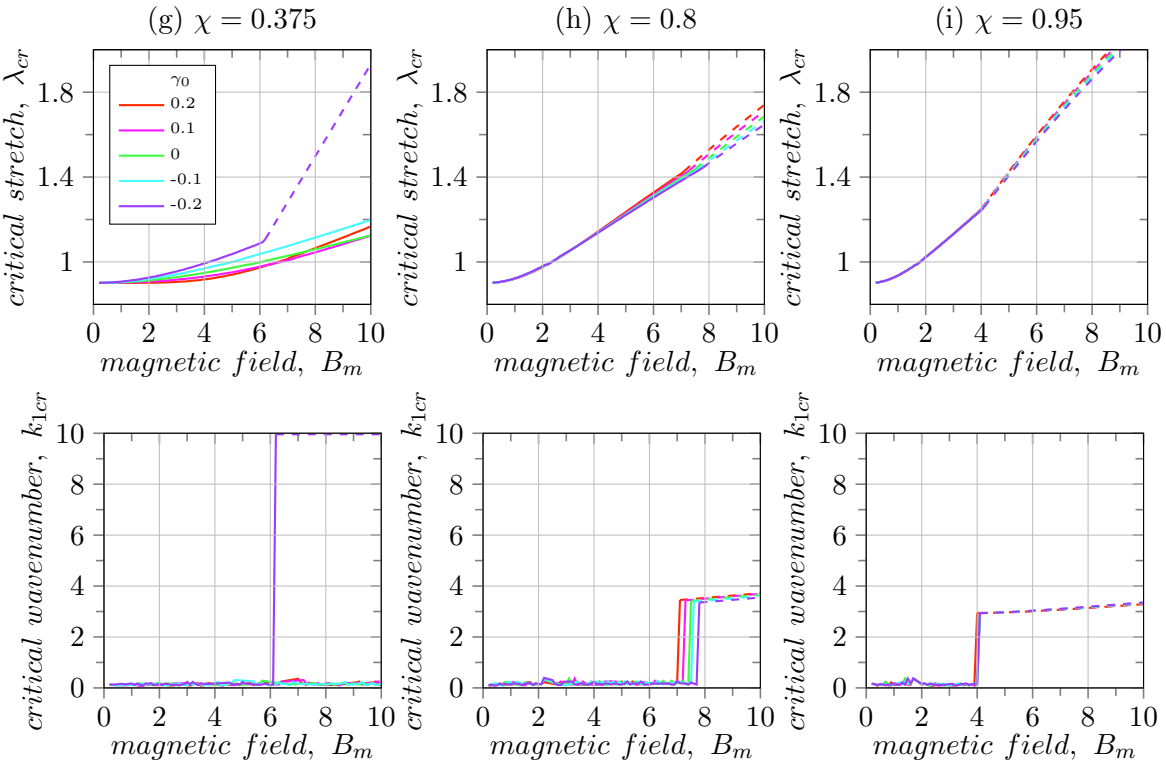

Volume fraction, $c^{(f)} = 0.4$

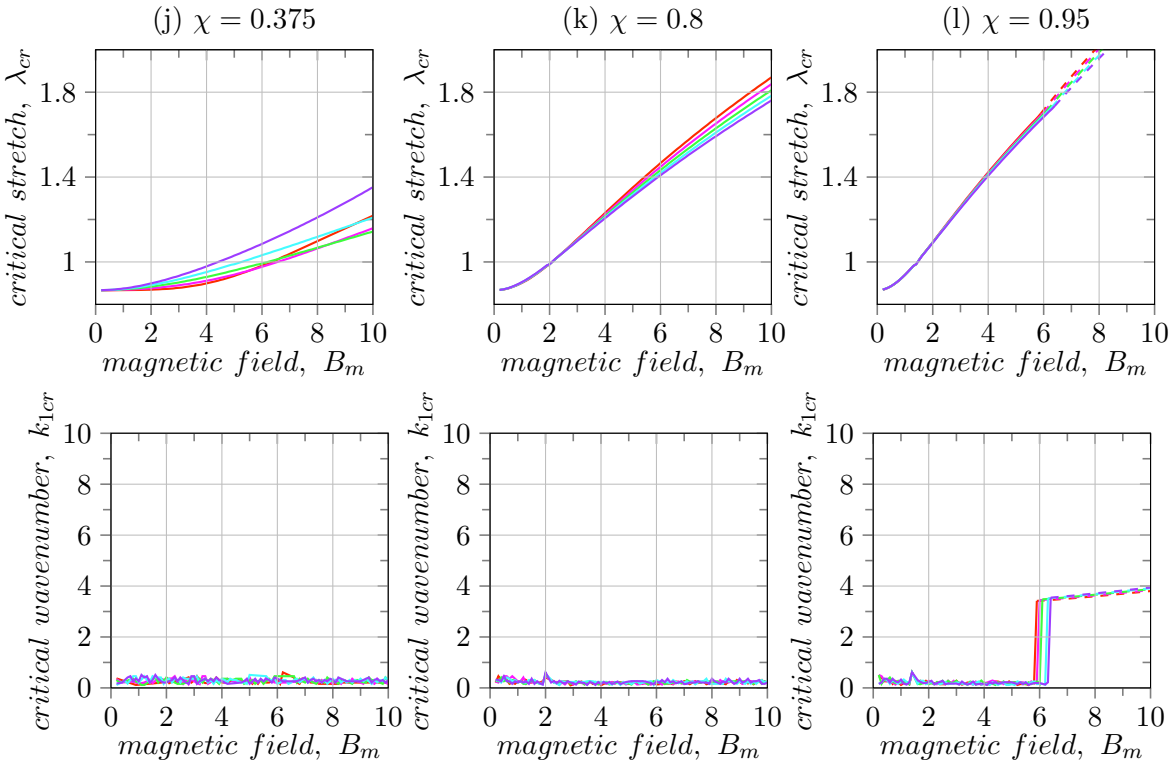

Figure 4.16: Critical stretch, λ_{cr} and critical wave-number, k_{1cr} vs. the normalized magnetic field B_m. MAEs with $\chi = 0.375, 0.8, 0.95$ are considered and of each of the χ values were simulated for stiff layer's volume fraction of $c^{(f)} = 0.2$, 0.4, 0.6, 0.8. The curves are considered for different γ_0 values ranging from $\gamma_0 = -0.2$ to $\gamma_0 = 0.2$ while keeping $\gamma_2 = 0$

4.5.3 Effect of initial susceptibility χ variation on the critical ratio λ_{cr} characteristics at low fiber volume fraction $c^{(f)}$

At low fiber volume fractions, the initial susceptibility plays a more important role in the effect of γ_0 coefficients, i.e., the effect of changes in γ_0 variation gets significantly reduced for higher susceptibility. This can be seen in the variation for all λ_{cr} curves, which reduces significantly at $\chi = 0.9$. But the variation in λ_{cr} is much greater when compared to the variation in mid-range volume fractions. In Fig. 4.14a, we observed that for smaller magnetic fields $B_m < 1$, the effects of the additional invariants on λ_{cr} were negligible. This is seen from the plot Fig. 4.14 as all the lines converge towards a single point as $B_m \to 0$ then $\lambda_{cr} \to 0.82$ for all γ_0 values and low volume fractions $c^{(f)} \leq 1$. Moreover, the increase in χ from $\chi = 0.375$ to $\chi = 0.9$ also impacted the transition behavior, as can be seen from

Fig. 4.17b. At $c^{(f)} = 0.1$, the transitions from symmetric microscopic to macroscopic were observed from $B_m = 6$ and $B_m = 8$ and $\chi = 0.375$ for different γ_0, while for $\chi = 0.8$ and $\chi = 0.9$ the transitions were observed at $B_m = 0.75$ and $B_m = 0.5$ respectively for all γ_0. At $c^{(f)} = 0.05$, the increase in γ_0 greatly impacted the transitions in high magnetic field region as can be seen from Fig. 4.17 f where $\chi = 0.9$ and $c^{(f)} = 0.05$. The transitions in k_{1cr} were seen for $\gamma_0 \leq 0$ from $B_m = 5.8$ to $B_m = 7.8$, while the wavenumber k_{1cr} at the transitions remained at $k_{1cr} = 7.9$. This tells us that low γ_0 values increase the chances of microscopic transitions at high magnetic fields for low-volume fractions for high susceptibility.

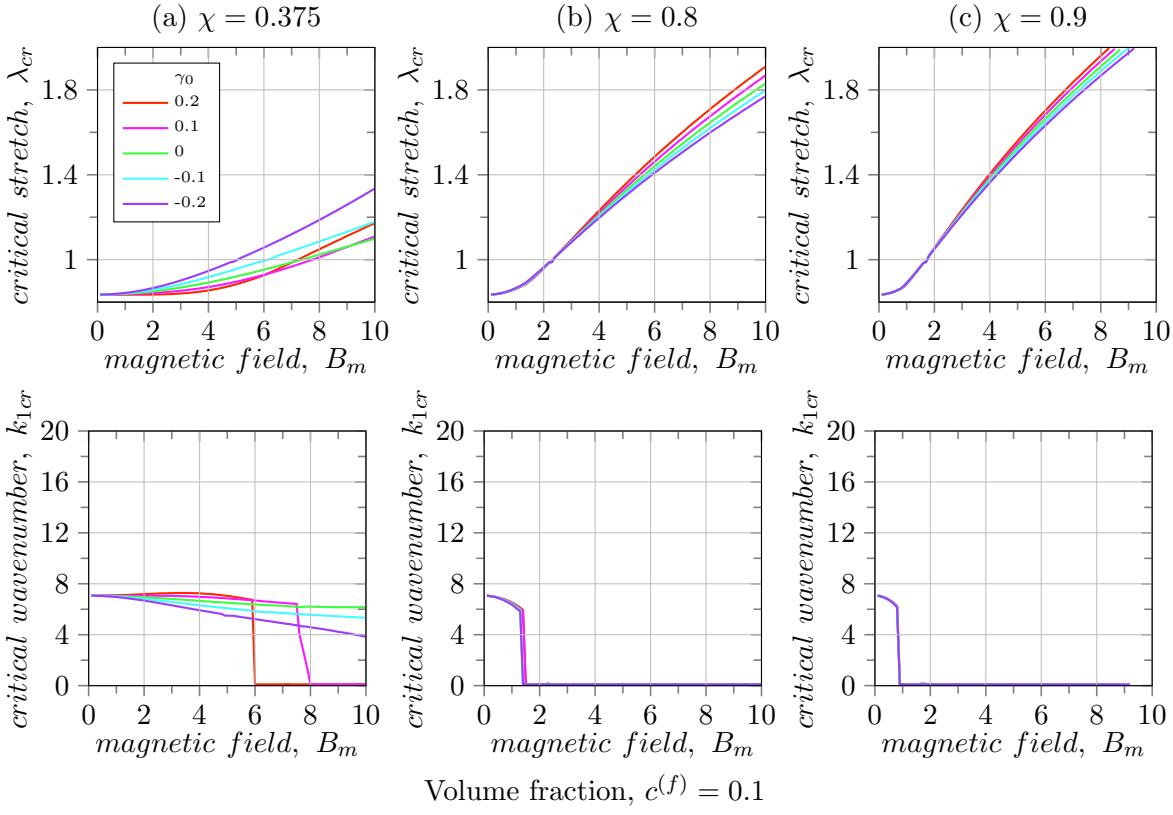

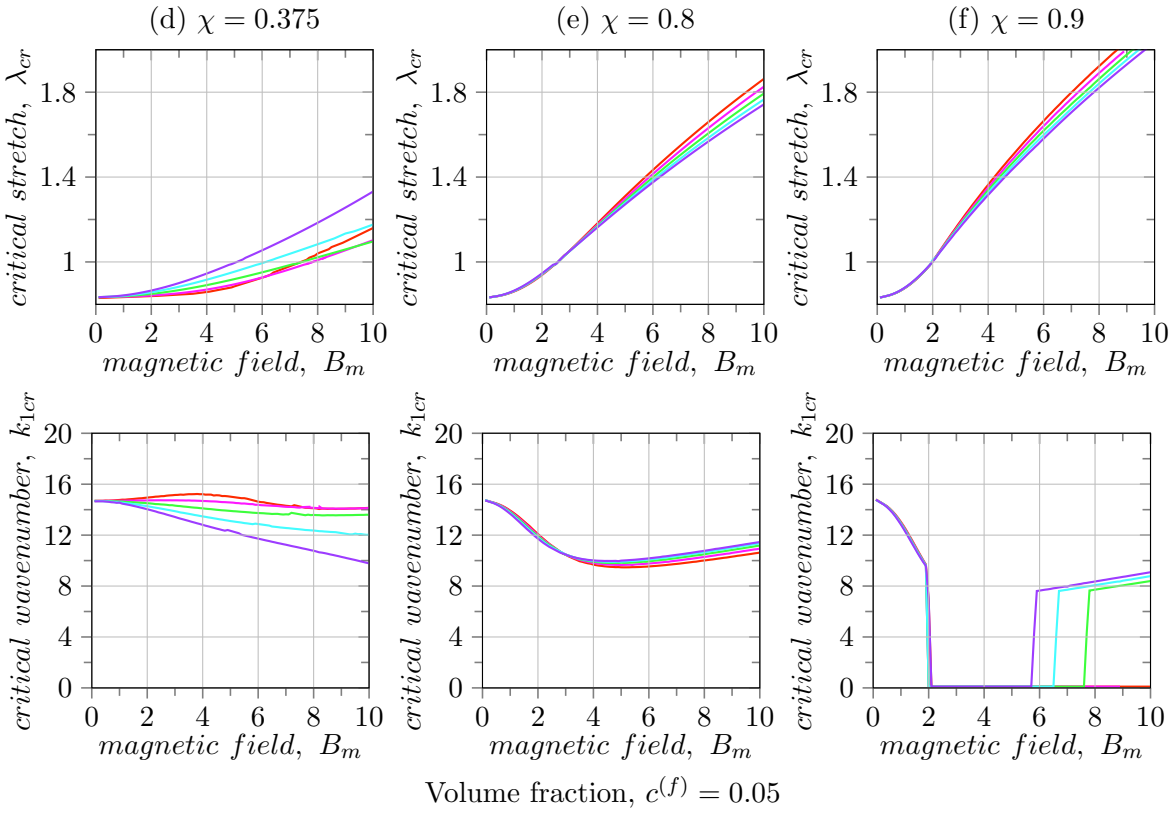

Figure 4.17: Critical stretch λ_{cr} vs. the normalized magnetic field B_m for MAEs with low fiber volume fraction $c^{(f)} = 0.05$, 0.1. The curves are considered for different γ_0 values ranging from $\gamma_0 = -0.2$ to $\gamma_0 = 0.2$ while keeping $\gamma_2 = 0$

4.6 Effect of γ_2 variation on magnetoelastic instabilities

Here, we study the morphologies of λ_{cr} and k_{1cr} as a function of the magnetic field B_m we have parameterized the curves with γ_2 and γ_1 coefficients ranging from $\gamma_2 = -0.2$ to $\gamma_2 = 0.2$ and $\gamma_1 = 0.8$ to $\gamma_1 = 1.2$. The constraints, $\gamma_0 = 0$ and $\gamma_2 + \gamma_1 = 1$ hold throughout this subsection. The default values for which this system becomes identical to the linear magnetic model are $\gamma_2 = 0$ and $\gamma_1 = 1$. In Fig. 4.18, we plot the critical stretch (a) and wavenumber (b) as the functions of the magnetic field B_m. We first examine the linear magnetic MAEs with fiber susceptibility of $\chi = 0.8$ and $c^{(f)} = 0.4$, where all the transitions would be present and clearly visible.

We observed that for smaller magnetic fields $B_m < 1$, the effects of the additional invariants on λ_{cr} were negligible. This is seen from the plot Fig. 4.18 as all $\lambda_{cr} \to 0.9$ for all γ_2 values.

Moreover, the increase in γ_0 from $\gamma_0 = -0.2$ to $\gamma_0 = 0.2$ also impacted the transition behavior, as can be seen from Fig. 4.18b. The transitions from macroscopic to microscopic were observed from $B_m = 6.5$ to $B_m = 8$. As γ_2 increased, the B_m for the transitions in k_{1cr} increased from $B_m = 6.5$ to $B_m = 7$, while the wavenumber k_{1cr} at the transitions remained almost constant at around $k_{1cr} = 3.5$. Thus γ_2 significantly affected the magnetic field for the transitions. As compared to changes in γ_0, the critical stretch in the macroscopic and microscopic region was significantly affected by the changes in γ_2. This can be seen from the fact that the critical stretch ratio at transitions decreased significantly from $\lambda_{cr} = 1.5$ to $\lambda_{cr} = 1.38$ as γ_2 increased from $\gamma_2 = -0.2$ to $\gamma_2 = 0.2$. This trend is opposite to that of γ_0, where critical stretch after transitions increased with an increase in γ_0. Moreover, in terms of the total variation, this change is much more significant, as compared to γ_0 (see Fig. 4.14). This is because, γ_2 is multiplied by I_6 in the magnetic energy equation (in 2.60), which has $\boldsymbol{C}^2$ factor (as per Eq. (2.61).) that greatly amplifies changes in the critical stretch in the total energy. Thus smaller changes in γ_2 bring about large changes in the critical stretch λ_{cr}.

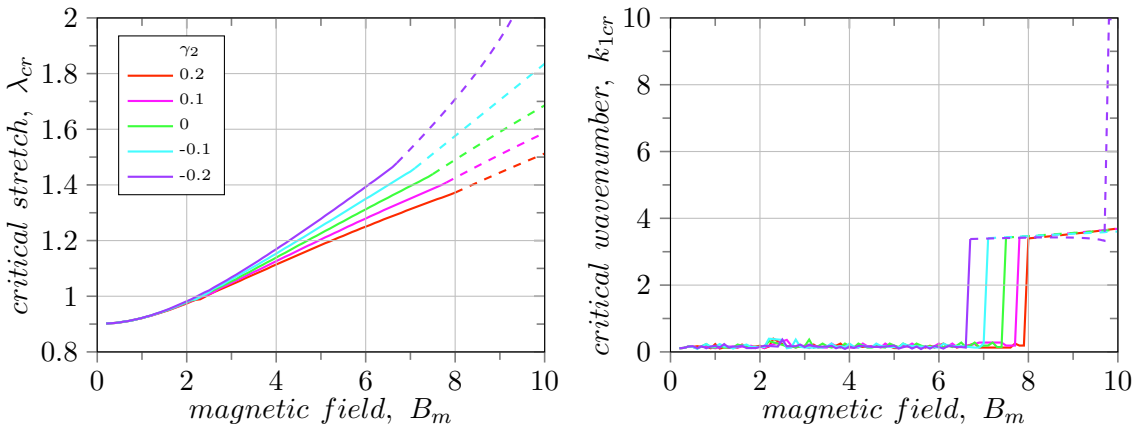

(a) λ_{cr} vs B_m (b) k_{1cr} vs B_m

Figure 4.18: Critical stretch λ_{cr} (a) and normalized critical wave numbers k_1 (b) vs. the normalized magnetic field B_m, for different γ_2 values ranging from $\gamma_2 = -0.2$ to $\gamma_2 = 0.2$ keeping $\gamma_0 = 0$. MAEs with stiff layer's volume fraction $c^{(f)} = 0.4$ and initial magnetic susceptibility $\chi = 0.8$ and the linear magnetic model

4.6.1 Effect of volume fraction variation on the γ_2 characteristic curves

Next, we study the effect of changing the volume fraction on the critical stretch ratio vs. the magnetic field. In Fig. 4.19, the critical stretch λ_{cr} are plotted in (a),(c),(e) while the critical wave numbers k_{1cr} are plotted in (b),(d),(f). Both of them are plotted as a

function of the magnetic field. Each of the cases for Fig. 4.19 was simulated for different mid range volume fractions from $c^{(f)} = 0.4$ to $c^{(f)} = 0.8$, while keeping $\gamma_0 = 0$ as constant.

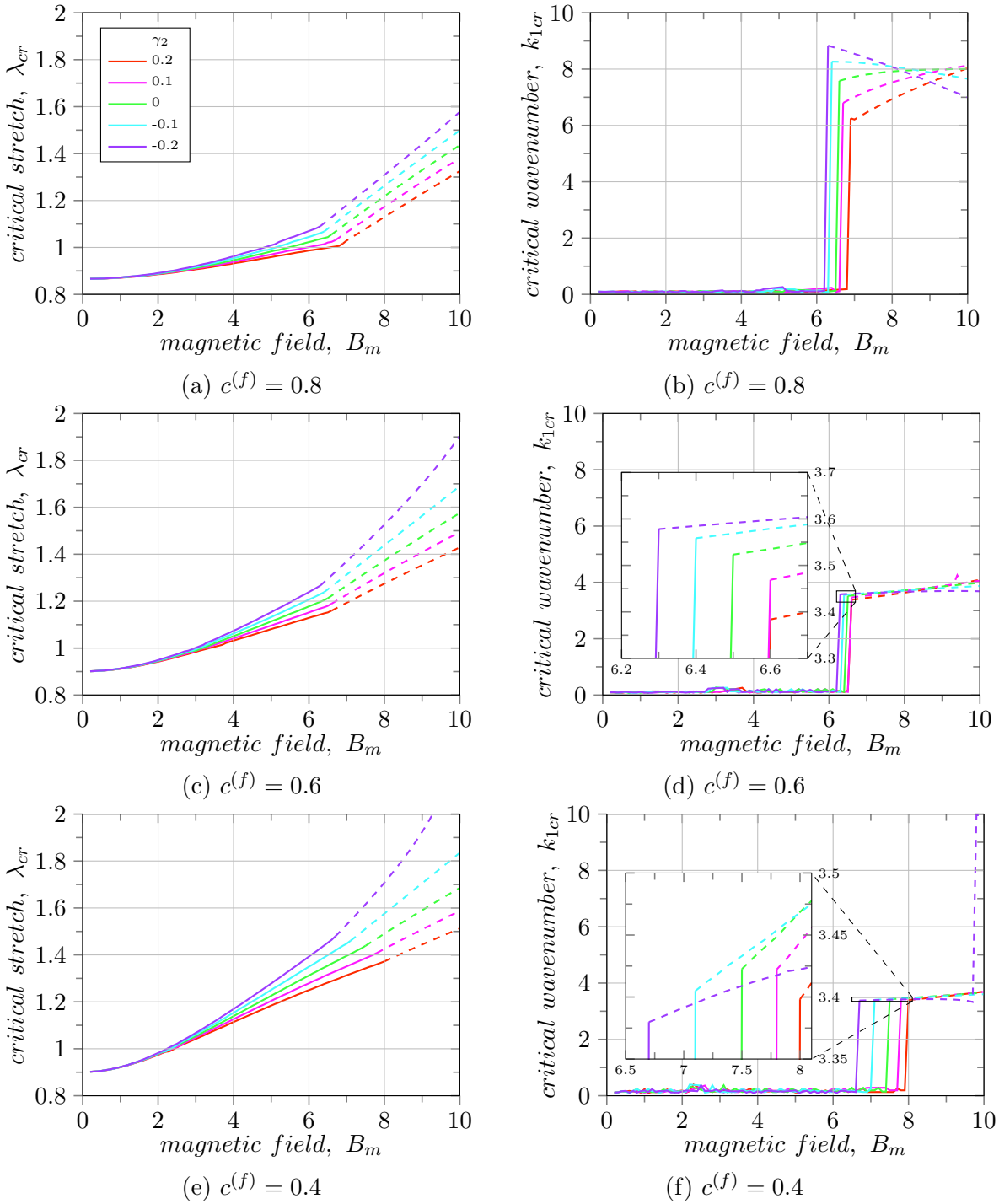

(a) $c^{(f)} = 0.8$ (b) $c^{(f)} = 0.8$

(c) $c^{(f)} = 0.6$ (d) $c^{(f)} = 0.6$

(e) $c^{(f)} = 0.4$ (f) $c^{(f)} = 0.4$

Figure 4.19: Critical stretch λ_{cr} (a),(c),(e) and normalized critical wavenumbers k_1 (b),(d),(f) both ploted against the magnetic field B_m. MAEs with $\chi = 0.8$ and fiber layer's volume fraction $c^{(f)} = 0.8$(a),(b); $c^{(f)}$=0.6(c),(d); $c^{(f)}$=0.4 (e),(d) are used as specifications. The curves are considered for different γ_2 values raging from $\gamma_2 = 0.2$ to $\gamma_2 = -0.2$ keeping $\gamma_0 = 0$

As the volume fraction of the fiber decreased from $c^{(f)} = 0.8$ to $c^{(f)} = 0.4$, the effect of changes in γ_2 was that at $B_m = 10$, the λ_{cr} variation increased from $\lambda_{cr} \in [1.3, 1.6]$ to $\lambda_{cr} \in [1.4, 1.9]$ and then increased again to $\lambda_{cr} \in [1.5, 2.5]$. This can be seen from the comparison of the transition region spread λ_{cr} values in Fig. 4.19 (a),(c), (e); In Fig. 4.19 (b) ,(d), (f); The transition magnetic field region first decreased also increased from $B_m \in [6.1, 6.4]$ at $c^{(f)} = 0.8$ to $B_m \in [6.3, 6.6]$ at $c^{(f)} = 0.6$ and then increased to $B_m \in [6.3, 8]$ at $c^{(f)} = 0.4$. At the transitions, k_{1cr} decreased from 8 to 4 and the variation in k_{1cr} also decreased from $\Delta k_{1cr} \in [1, 0.2]$

Because γ_2 is multiplied by the $\mathbf{C}^2$ (as in Eq (2.61)), the effect on stability is also highly non-linear, and so λ_{cr} increases more sharply when compared to the γ_0 case for all the volume fractions.

4.6.2 Effect of initial susceptibility χ and volume fraction variation on the γ_2 characteristics

In this section, we study the effects of changing the initial susceptibility χ and volume fraction $c^{(f)}$ on the critical stretch λ_{cr} vs. magnetic field B_m, along with changing γ_2. In Fig. 4.20, λ_{cr} is plotted as a function of the magnetic field, and each of the cases was simulated for different χ values ranging from $\chi = 0.375$ to $\chi = 0.95$ and different mid-range volume fractions from $c^{(f)} = 0.2$ to $c^{(f)} = 0.8$. The corresponding μ_r values are $\mu_r = 1.6$ to $\mu_r = 5$ and $\mu_r = 20$ respectively.

From the results in Fig. 4.20, we observe that the initial susceptibility χ plays a more significant role in reducing the effects of γ_2 variations than variations in the volume fraction. We observe that for higher χ, as the initial susceptibility χ increases, the variation in the different curves for γ_2 becomes negligible. Moreover, at high initial susceptibility $\chi = 0.95$, the variation in the transition points is lost for almost all values of γ_2. This can be seen in Fig. 4.20 (c),(f),(i),(l) from the fact that the intersection of the gamma curves reduces to almost a single point at $\chi = 0.95$ at all the volume fractions $0.4 < c^{(f)} < 0.8$. The exception is at $c^{(f)} = 0.2$ where we can see a range for k_{1cr} values from $k_{1cr} = 5.1$ to $k_{1cr} = 7.2$ and a range of $\lambda_{cr} = 1.7$ to $\lambda_{cr} = 1.85$ as can be seen in Fig. 4.20 (j). Thus higher initial susceptibility χ reduces the effect of the γ_2 and the I_6 terms on the magnetic field $\mathbf{B}$ vs. λ_{cr} relationship. Moreover, at high initial susceptibility, the variation in the transition points is lost for almost all values of γ; for e.g., at $c^{(f)} = 0.8$, the transition point for λ_{cr} vs. B_m is $(4.8, 1)$ for all values of γ_0 and this same trend is observed for rest of the volume fractions, till $c^{(f)} = 0.4$ at high susceptibility of $\chi = 0.95$ with the exception at $c^{(f)} = 0.2$. The variation in the λ_{cr} and k_{1cr} vs B_m curves is also lost at high $\chi = 0.95$ for $c^{(f)} \geq 0.4$

At low $\chi = 0.375$, the variation of λ_{cr} values is quite significant for all volume fractions $0.2 \leq c^{(f)} \leq 0.8$ as can be seen from all the plots of λ_{cr} vs. B_m in Fig. 4.20. The anti-symmetric microscopic transitions also disappear while we start to see symmetric microscopic transitions appear at $B_m = 7.5$ to $B_m = 9$.

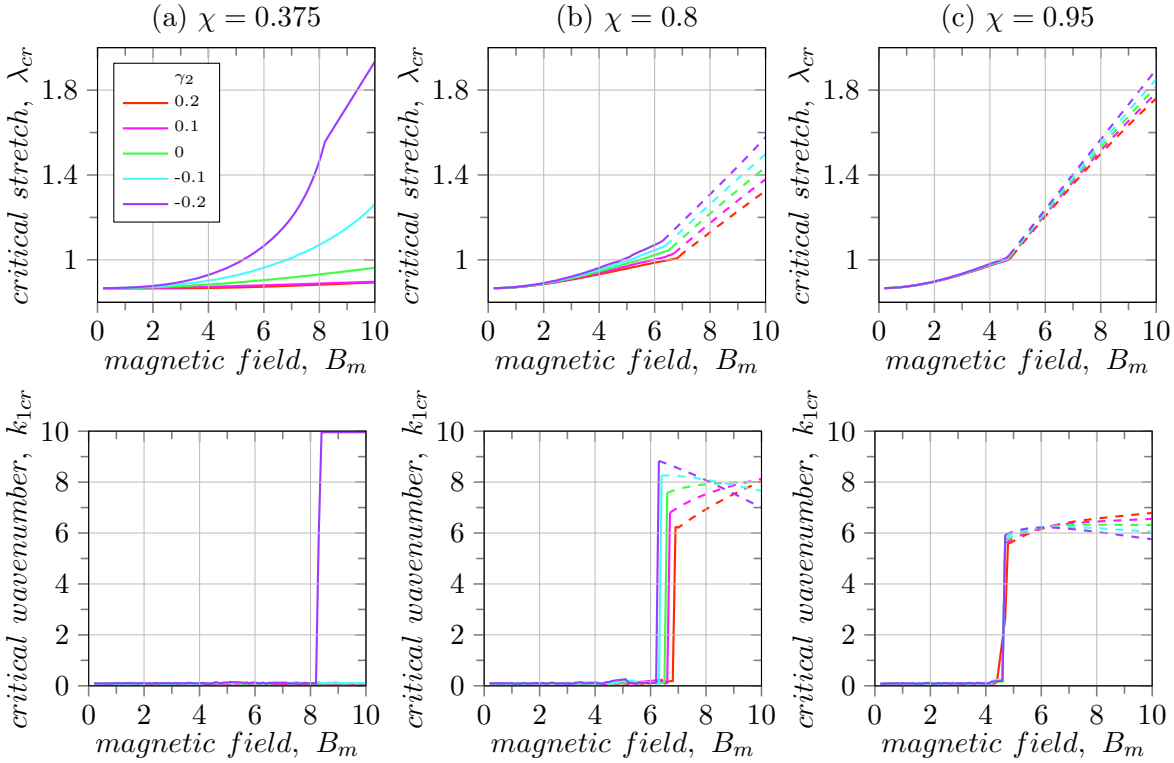

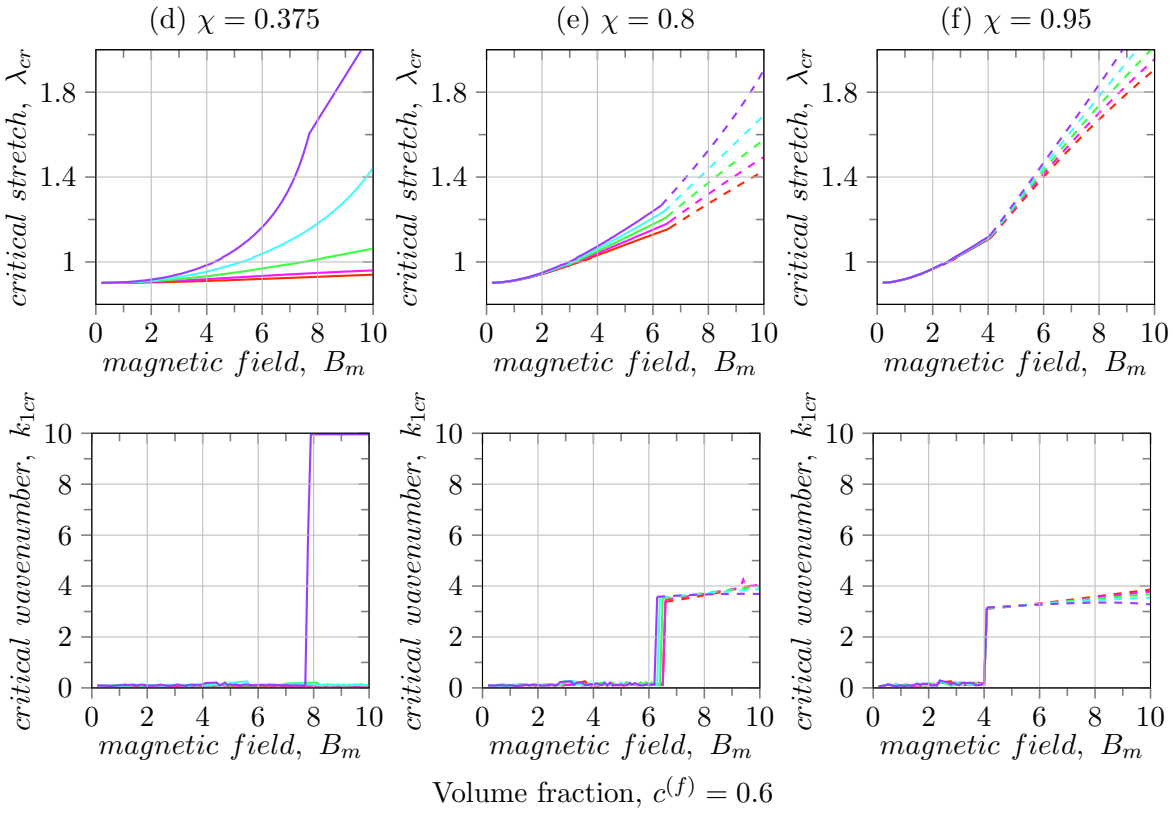
(d) $\chi = 0.375$
(e) $\chi = 0.8$
(f) $\chi = 0.95$
critical stretch, λ_{cr}
1
1.4
1.8
critical wavenumber, k_{1cr}
0
2
4
6
8
10
0
2
4
6
8
10
magnetic field, B_m
Volume fraction, $c^{(f)} = 0.6$

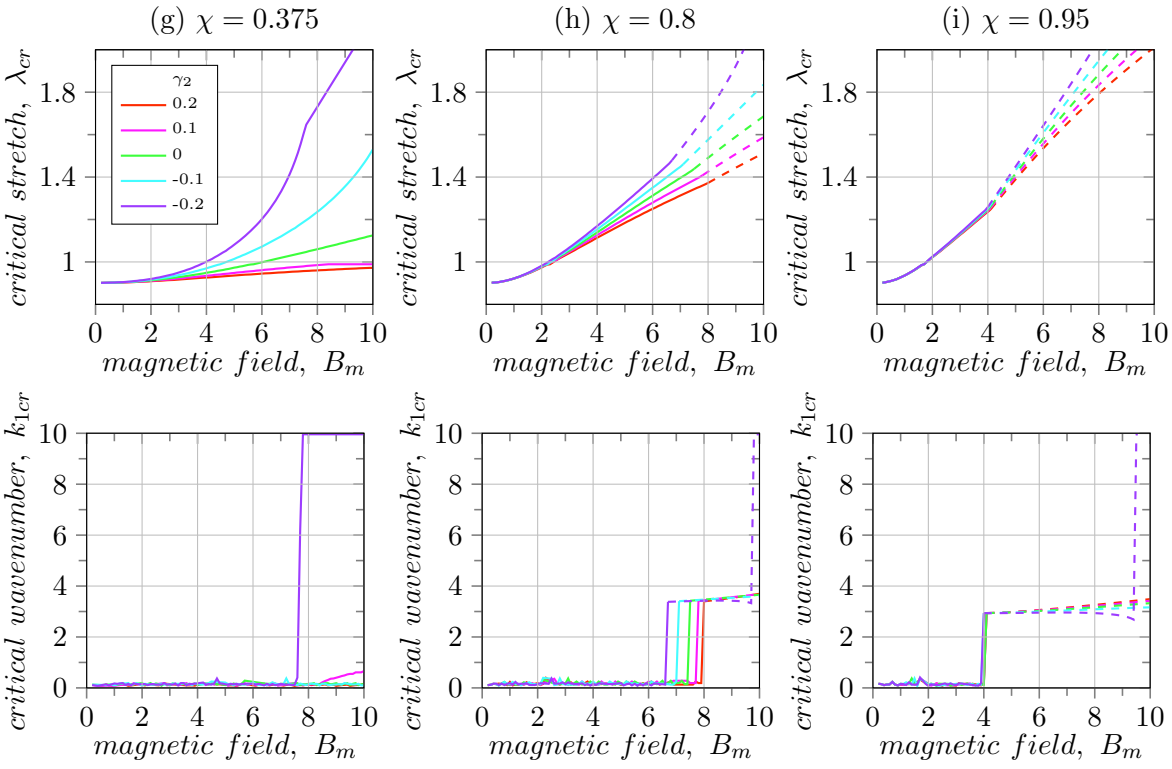

Volume fraction, $c^{(f)} = 0.4$

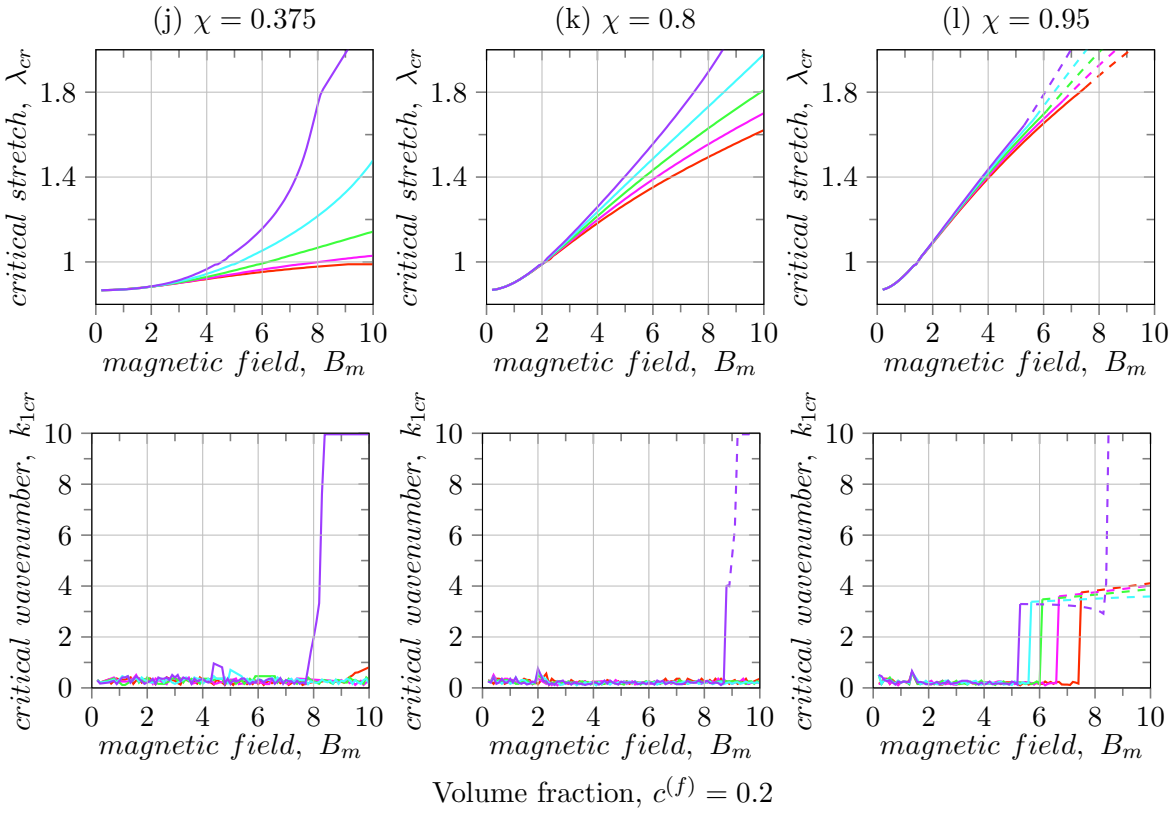

Figure 4.20: Critical stretch, λ_{cr} and critical wave-number, k_{1cr} vs. the normalized magnetic field B_m. MAEs with $\chi = 0.375, 0.8, 0.95$ are considered and of each of the χ values were simulated for stiff layer's volume fraction of $c^{(f)} = 0.2$, 0.4, 0.6, 0.8. The curves are considered for different γ_0 values ranging from $\gamma_2 = -0.2$ to $\gamma_2 = 0.2$ while keeping $\gamma_2 = 0$

4.6.3 Effect of initial susceptibility χ variation on the critical ratio λ_{cr} characteristics at low fiber volume fraction $c^{(f)}$

At low fiber volume fractions, the initial susceptibility plays a more important role in the effect of γ_2 coefficients, i.e., the effect of changes in γ_2 variation is present for susceptibility and volume fractions.

The variation in λ_{cr} is significantly higher for all low $c^{(f)}$ and χ values when compared to similar variation in γ_2 in the mid-range volume-fractions (see Fig. 4.20) as well as γ_0 at low volume fractions (see Fig. 4.17). This can be seen from all the λ_{cr} curves in Fig. 4.21).

In Fig. 4.21a, we observed that for smaller magnetic fields $B_m < 1$, the effects of the additional invariants on λ_{cr} were negligible. This is seen from the plot Fig. 4.21 as all the lines converge towards a single point as $B_m \to 0$ then $\lambda_{cr} \to 0.82$ for all γ_2 values at low

volume fractions $c^{(f)} \leq 1$.

Moreover, the increase in χ from $\chi = 0.375$ to $\chi = 0.9$ also impacted the transition behavior, as seen from Fig. 4.21. At $c^{(f)} = 0.1$, The transitions from symmetric microscopic to macroscopic were observed from $B_m = 4.5$ and $B_m = 6$ for $\gamma_2 \geq 0.1$, $\chi = 0.375$ and $c^{(f)} = 0.1$, while for $\chi = 0.8$ and $\chi = 0.9$ the transitions were observed at $B_m = 0.75$ and $B_m = 0.5$ respectively for all γ_2, At $c^{(f)} = 0.05$ Fig. 4.21(d),(e) (f), the increase in γ_2 greatly impacted the transitions in high magnetic field region as can be seen from Fig. 4.21 (f) where $\chi = 0.9$. The transitions in k_{1cr} were seen for $\gamma_2 \leq 0$ from $B_m \in [5.5, 7.7]$, while the wave-number k_{1cr} at the transitions remained in the range $k_{1cr} \in [8, 8.5]$.

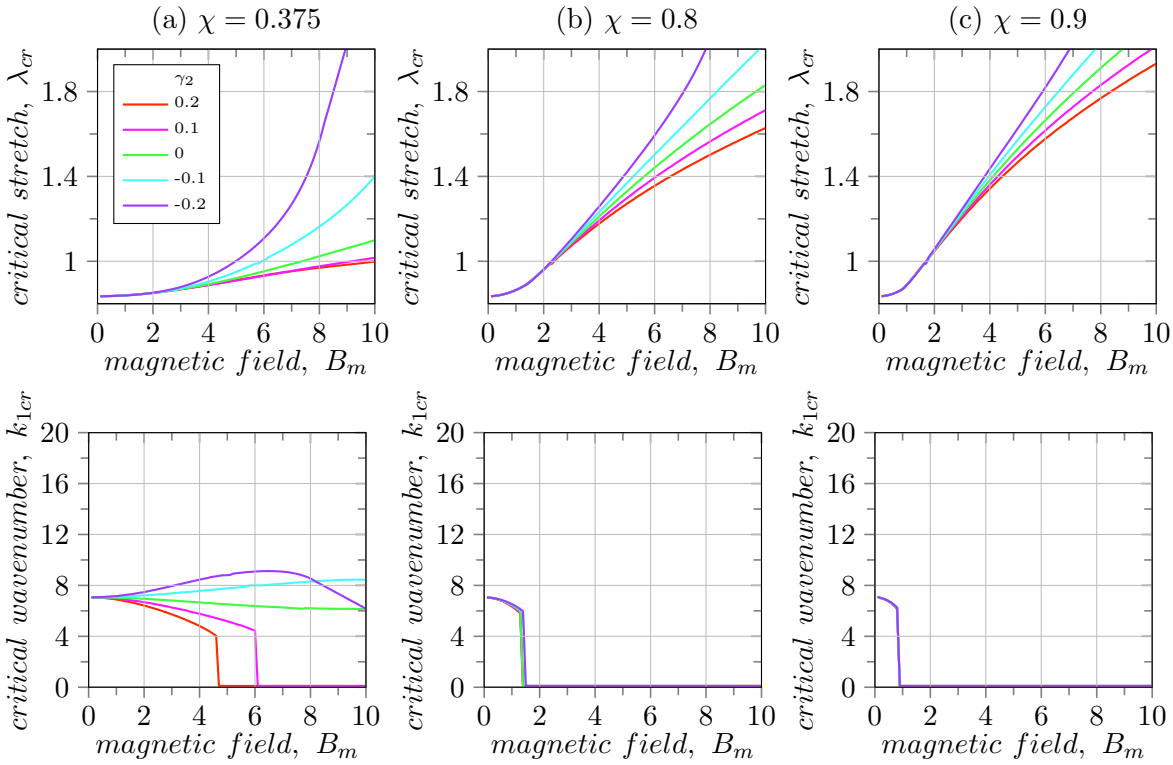

Volume fraction, $c^{(f)} = 0.1$

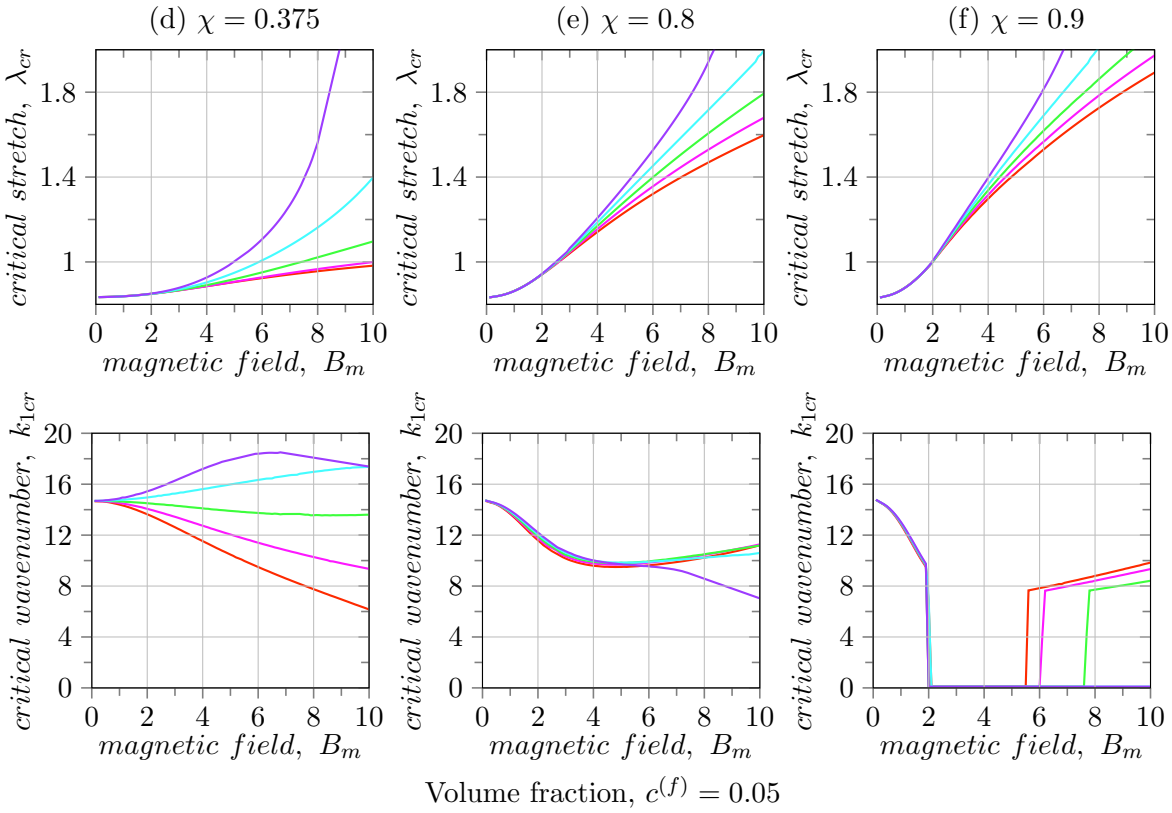

Figure 4.21: Critical stretch λ_{cr} vs. the normalized magnetic field B_m. MAEs with stiff layer's volume fraction low fiber volume fraction $c^{(f)} = 0.05, 0.1$. The curves are considered for different γ_2 values ranging from $\gamma_0 2 = -0.2$ to $\gamma_2 = 0.2$ while keeping $\gamma_0 = 0$

4.7 Differences between γ_0 and γ_2 characteristics

The effect of change in γ_2 was more drastic as compared to γ_0. This is because of the $\mathbf{C}^2$ factor involved in I_6 (2.61). When γ_2 increased, λ_{cr} also increased, thus decreasing the stability region. The increasing volume fraction also pushed the transition point further higher. As γ_2 contains higher order terms for F, it was also much harder to get a well-defined solution for higher values of γ_2. We can see this when some of the values for γ_0 abruptly stop at λ_{cr} while γ_0 values were available for a larger sub-domain than γ_2. Thus, further empirical evidence is required for the energy models for I_4 and I_6 to be verified.

Chapter 5

Conclusion

In this dissertation, we investigated the behavior of MAEs with biphasic layered microstructure with ferromagnetic hyperelastic phases. We considered the MAE laminates subjected to a magnetic field perpendicular to the direction of layers. First, we derived an explicit expression for the field-induced stretch in response to the remotely applied magnetic field. Second, we performed the magneto-elastic instability analysis for layered MAEs, by employing the small amplitude perturbation superimposed on finite deformations in the presence of a magnetic field. While the formulation developed here is general for any magnetic behavior of phases, the results are presented for the special class of MAEs with magnetically inactive matrix and active stiff layer phase.

5.1 MAEs deformation

We found that the layered MAEs experience tension along the direction of the magnetic field, and the induced stretch increases with an increase in the applied magnetic field. However, because of the magnetic saturation effect, the MAEs with smaller saturation values attain smaller deformation levels. We also showed that the MAEs with higher volume fractions of the active phase develop large deformations, irrespective of the shear modulus contrast between the phases.

5.2 Effect of magnetic field on instabilities

The layered MAEs, when subjected to higher magnitudes of the magnetic field, develop instabilities at higher stretches along the direction of layers (perpendicular to the magnetic field). MAEs are observed to be unstable even under tensile strains in the presence of a strong magnetic field. The magnetic saturation effect, however, results in a decrease

in critical stretch levels. Moreover, the wavelength of buckling patterns is shown to be highly tunable by the applied magnetic field. The comparison of critical parameters – for MAEs with various morphologies – shows that a decrease in magnetic susceptibility and/or magnetic saturation values (at a given magnetic field magnitude) has a similar response as reducing the applied magnetic field magnitude.

5.3 Effect of volume fraction on instability

The instability mode and their transitions in layered MAEs are strongly dictated by the volume fraction of phases together with the applied magnetic field. In the presence of a weak magnetic field, similar to the purely mechanical case of layered composites, the layered MAEs also show the transition in instability modes once, with the change in volume fraction. Thus, the symmetric microscopic instability occurs at small volume fractions of the active stiff phase, whereas macroscopic loss of stability occurs at higher volume fractions. Under higher magnetic fields, however, the MAE laminates show two transitions with three distinct instability modes at different active phase volume fractions. First, symmetric microscopic instability is detected at smaller volume fractions. Second, at moderate volume fractions, long-wave instability emerges. Interestingly, the MAEs with higher volume fractions develop microscopic instability with *anti-symmetric* buckling patterns. We found that under stronger magnetic fields, the range of active stiff phase volume fractions, at which the anti-symmetric mode is attained, further increases. Hence, the application of a magnetic field promotes the development of anti-symmetric buckling patterns. It is worth noting that the anti-symmetric microscopic instability mode is inadmissible in the purely mechanical setting (without a magnetic field).

5.4 Macroscopic and microscopic instability solution

In the case of microscopic instabilities, the general solution to the MAE was found to be a bi-directional periodic function. In the case of the macroscopic, the instability degenerates into a long-wave macroscopic instability which is periodic in one direction. This can also be seen from wave number k_1 is zero. Depending on the periodicity of the solution, the modes of instability can be either symmetric or anti-symmetric. Based on empirical observation of the solution, the anti-symmetric modes correspond to the microscopic instability while symmetric modes (usually) correspond to the macroscopic instability. Depending on which of the modes had the highest critical stretch (λ_{cr}), only one of the symmetric or anti-symmetric modes manifested as the default state of the MAE, and the point at which it transitioned was the transition point.

5.5 Numerical methods and analysis

The choice of numerical method greatly impacted our ability to correctly capture the solution space. Calculating the eigenvalues directly from the equations increased the numerical noise due to matrix singularities, and the effects of matrix exponents in the solution created discontinuities. Using polynomial functions of the eigenvalues solved the problem of numerical noise created by the exponential term within the solution. Using incremental changes in the solution also reduced solution time by reducing the size of the domain and improved the accuracy by confining the search domain to a smaller region around the solution. This made the algorithm more robust and less likely to fail due to arbitrary numerical noise.

5.6 Effect of the additional magnetic field invariants

We also took into consideration the effects of additional invariants I_4 and I_6 on the critical stretch ratio λ_{cr} and critical wave number k_{1cr}. For lower susceptibility values, even small changes in γ co-efficient caused larger changes in the characteristics of the stability region. In contrast, for higher susceptibility, the effect of variation in γ coefficients and their invariants I_4, I_5, and I_6 was greatly reduced. Changes in γ_2 and I_6 were found to have a larger effect on instability as compared to changes in γ_0 and I_4 since we have a higher order factor C^2 multiplying the magnetic term in the energy equation. The susceptibility had a significant impact on stability as compared to the volume fraction. For lower susceptibility, the variation of γ coefficients changed the stability region and the transition points. In contrast, for a higher susceptibility, the effect of changes γ was less significant on the stability region.

5.7 Impact of MAEs

The presented results can help widen the design space for novel materials with switchable functionalities with potential applications in remotely controlled soft micro-actuators and sensors. Moreover, the theoretically predicted anti-symmetric buckling mode can motivate further experimental studies of the micro-structured MAEs. In the study, we have considered the MAEs subjected to quasi-static loading; therefore, the viscous and inertial effects have not been considered. However, for the dynamic loading, these effects can influence the material stability, as observed, for example, in the soft laminates Slesarenko and Rudykh (2016). To investigate the influence of time-dependent magneto-mechanical loading on the instability development in MAEs, one should account for the phase rate-

dependent behavior and inertia in the modeling. Additionally, the understanding of the material behavior can benefit from the implementation of multi-scale modeling that could more accurately capture the global finite size effects, as well as smaller length-scale effects (such as, for example, dipole-dipole interactions).

Bibliography

Books

Bertotti, G. *Hysteresis in magnetism: for physicists, materials scientists, and engineers*. Gulf Professional Publishing, (1998).

Brown, W. F. *Magnetoelastic interactions*. Vol. 9. Springer, (1966).

Galipeau, E. *Non-linear homogenization of magnetorheological elastomers at finite strain*. English. Ed. by P. P. Castañeda. ProQuest Dissertations and Theses. 3551190. Ann Arbor: University of Pennsylvania, 262, (2012).

Holzapfel, G. *NONLINEAR SOLID MECHANICS. A Continuum Approach for Engineering*. John Wiley & Sons, (2001).

Kovetz, A. *Electromagnetic theory*. Vol. 975. Oxford University Press Oxford, (2000).

Ogden, R. W. *Non-linear elastic deformations*. Courier Corporation, (1997).

Truesdell, C. and Noll, W. *The non-linear field theories of mechanics*. Springer, (1965).

Wang, C.-c. and Truesdell, C. *Introduction to rational elasticity*. Vol. 1. Springer Science & Business Media, (1973).

Collections

Attard, B., Mohamed, A. E.-M. A., and Attallah, M. M. "19 - New materials development". *Fundamentals of Laser Powder Bed Fusion of Metals*. Ed. by I. Yadroitsev, I. Yadroitsava, A. du Plessis, and E. MacDonald. Additive Manufacturing Materials and Technologies. Elsevier, 529–562, (2021).

Bhattacharya, S. "Nanostructures in gene delivery". *Advances in Polymeric Nanomaterials for Biomedical Applications*. Elsevier, 101–135, (2021).

Coleman, B. D. and Noll, W. "The thermodynamics of elastic materials with heat conduction and viscosity". *The Foundations of Mechanics and Thermodynamics*. Springer, 145–156, (1974).

Inoue, A. and Kong, F. "Soft Magnetic Materials". *Encyclopedia of Smart Materials*. Ed. by A.-G. Olabi. Oxford: Elsevier, 10–23, (2022).

McHenry, M. "Magnetic Steels". *Encyclopedia of Materials: Science and Technology*. Ed. by K. J. Buschow, R. W. Cahn, M. C. Flemings, B. Ilschner, E. J. Kramer, S. Mahajan, and P. Veyssière. Oxford: Elsevier, 4961–4964, (2001).

Truesdell, C. and Toupin, R. "The classical field theories". *Handbuch der Physik, vol. III*. Springer, Berlin, (1960).

Proceedings

Ginder, J. M., Schlotter, W. F., and Nichols, M. E. "Magnetorheological elastomers in tunable vibration absorbers". *Smart structures and materials 2001: damping and isolation*. Vol. 4331. International Society for Optics and Photonics, 103–110, (2001).

Guan, X., Dong, X., and Ou, J. "Effect of soft magnetic materials blend on the properties of polymer-bonded Terfenol-D composites". *Behavior and Mechanics of Multifunctional and Composite Materials 2007*. Vol. 6526. SPIE, 602–606, (2007).

Rosen, B. W. "Mechanics of Composite Strengthening". *Fibre Composite Materials*. Am. Soc. Metals. Ohio, 37–75, (1965).

Articles

Abramchuk, S., Grishin, D., Kramarenko, E. Y., Stepanov, G., and Khokhlov, A. "Effect of a homogeneous magnetic field on the mechanical behavior of soft magnetic elastomers under compression". *Polymer Science Series A* 48.2, 138–145, (2006).

Alam, Z., Padmanabhan, S., and Sharma, A. K. "Magnetically tunable longitudinal wave band gaps in hard-magnetic soft laminates". *International Journal of Mechanical Sciences* 249, 108262, (2023).

Alapan, Y., Karacakol, A. C., Guzelhan, S. N., Isik, I., and Sitti, M. "Reprogrammable shape morphing of magnetic soft machines". *Science Advances* 6.19, eabc6414, (2020).

Anil, K., Bastola, and Hossain, M. "The shape – morphing performance of magnetoactive soft materials". *Materials and Design* 211, 110172, (2021).

Arora, N., Batan, A., Li, J., Slesarenko, V., and Rudykh, S. "On the Influence of Inhomogeneous Interphase Layers on Instabilities in Hyperelastic Composites". *Materials* 12.5, 763, (2019).

Arora, N., Li, J., Slesarenko, V., and Rudykh, S. "Microscopic and long-wave instabilities in 3D fiber composites with non-Gaussian hyperelastic phases". *International Journal of Engineering Science* 157, 103408, (2020).

Arora, N., Pathak, P., Chen, V., Juhl, A., Buskohl, P., and Rudykh, S. "Magnetoelastic instability induced pattern transitions in soft ferromagnetic laminates". *Bulletin of the American Physical Society*, 1–2, (2022).

Bastola, Anil, K., and Hossain, M. "A review on magneto-mechanical characterizations of magnetorheological elastomers". *Composites Part B: Engineering*, 108348, (2020).

Bednarek, S. "The giant magnetostriction in ferromagnetic composites within an elastomer matrix". *Applied Physics A* 68.1, 63–67, (1999).

Bednarek, S. "Tensoinductive effects in elastic ferromagnetic composites". *Chinese journal of Physics* 38.2, 169–181, (2000).

Bertoldi, K. and Boyce, M. C. "Mechanically triggered transformations of phononic band gaps in periodic elastomeric structures". *Phys. Rev. B* 77.5, 052105, (2008).

Bertoldi, K. and Gei, M. "Instabilities in multilayered soft dielectrics". *J. Mech. Phys. Solids* 59, 18–42, (2011).

Bertoldi, K. and Lopez-Pamies, O. "Some remarks on the effect of interphases on the mechanical response and stability of fiber-reinforced elastomers". *Journal of Applied Mechanics* 79.3, 031023, (2012).

Bira, N., Dhagat, P., and Davidson, J. R. "A review of magnetic elastomers and their role in soft robotics". *Frontiers in Robotics and AI* 7, 588391, (2020).

Bowen, L., Springsteen, K., Feldstein, H., Frecker, M., Simpson, T. W., and Lockette, P. von. "Development and validation of a dynamic model of magneto-active elastomer actuation of the origami waterbomb base". *Journal of Mechanisms and Robotics* 7.1, 011010, (2015).

Chen, L., Gong, X. L., and Li, W. H. "Microstructures and viscoelastic properties of anisotropic magnetorheological elastomers". *Smart Mater. Struct.* 16, 2645–2650, (2007).

Chen, T., Pauly, M., and Reis, P. M. "A reprogrammable mechanical metamaterial with stable memory". *Nature* 589.7842, 386–390, (2021).

Ciambella, J., Stanier, D. C., and Rahatekar, S. S. "Magnetic alignment of short carbon fibres in curing composites". *Composites Part B* 109, 129–137, (2017).

Crivaro, A., Sheridan, R., Frecker, M., Simpson, T. W., and Von Lockette, P. "Bistable compliant mechanism using magneto active elastomer actuation". *Journal of Intelligent Material Systems and Structures* 27.15, 2049–2061, (2016).

Cui, J., Huang, T. Y., Luo, Z., Testa, P., Gu, H., Chen, X. Z., Nelson, B. J., and Heyderman, L. J. "Nanomagnetic encoding of shape-morphing micromachines". *Nature* 575.7781, 164–168, (2019).

Danas, K., Kankanala, S. V., and Triantafyllidis, N. "Experiments and modeling of iron-particle-filled magnetorheological elastomers". *J. Mech. Phys. Solids* 60, 120–138, (2012).

Danas, K. and Triantafyllidis, N. "Instability of a magnetoelastic layer resting on a non-magnetic substrate". *J. Mech. Phys. Solids* 69, 67–83, (2014).

Dargahi, A., Sedaghati, R., and Rakheja, S. "On the properties of magnetorheological elastomers in shear mode: Design, fabrication and characterization". *Composites Part B: Engineering* 159, 269–283, (2019).

Deng, H., Gong, X., and Wang, L. "Development of an adaptive tuned vibration absorber with magnetorheological elastomer". *Smart Mater. Struct.* 15, N111–N116, (2006).

Dorfmann, A. and Haughton, D. "Stability and bifurcation of compressed elastic cylindrical tubes". *International Journal of Engineering Science* 44.18-19, 1353–1365, (2006).

Dorfmann, A. and Ogden, R. W. "Nonlinear magnetoelastic deformations". *Q. J. Mech. Appl. Math.* 57, 599–622, (2004).

Dorfmann, A. and Ogden, R. W. "Nonlinear magnetoelastic deformations". *Q. J. Mech. Appl. Math.* 57, 599–622, (2004).

Erb, R. M., Libanori, R., Rothfuchs, N., and Studart, A. R. "Composites reinforced in three dimensions by using low magnetic fields". *Science* 335.6065, 199–204, (2012).

Farshad, M. and Le Roux, M. "A new active noise abatement barrier system". *Polymer Testing* 23, 855–860, (2004).

Florijn, B., Coulais, C., and Hecke, M. van. "Programmable mechanical metamaterials: the role of geometry". *Soft matter* 12.42, 8736–8743, (2016).

Galich, P. I. and Rudykh, S. "Manipulating pressure and shear elastic waves in dielectric elastomers via external electric stimuli". *Int. J. Solids Struct.* 91, 18–25, (2016).

Galipeau, E. and Ponte Castañeda, P. "The effect of particle shape and distribution on the macroscopic behavior of magnetoelastic composites". *Int. J. Solids Struct.* 49, 1–17, (2012).

Galipeau, E., Rudykh, S., deBotton, G., and Ponte Castañeda, P. "Magnetoactive elastomers with periodic and random microstructures". *Int. J. Solids Struct.*, (2014).

Garcia-Gonzalez, D. and Hossain, M. "Microstructural modelling of hard-magnetic soft materials: Dipole–dipole interactions versus Zeeman effect". *Extreme Mechanics Letters* 48, (2021).

Garcia-Gonzalez, D. and Hossain, M. "A microstructural-based approach to model magneto-viscoelastic materials at finite strains". *International Journal of Solids and Structures* 208, 119–132, (2020).

Geymonat, G., Müller, S., and Triantafyllidis, N. "Homogenization of Nonlinearly Elastic Materials, Microscopic Bifurcation and Macroscopic Loss of Rank-One Convexity". *Arch. Rational. Mech. Anal.* 122, 231–290, (1993).

Ginder, J. M., Schlotter, W. F., and Nichols, M. E. "Magnetorheological elastomers in tunable vibration absorbers". *Proc. SPIE* 4331, 103, (2001).

Ginder, J., Clark, S., Schlotter, W., and Nichols, M. "Magnetostrictive phenomena in magnetorheological elastomers". *International Journal of Modern Physics B* 16.17n18, 2412–2418, (2002).

Gong, X., Fan, Y., Xuan, S., Xu, Y., and Peng, C. "Control of the damping properties of magnetorheological elastomers by using polycaprolactone as a temperature-controlling component". *Industrial & engineering chemistry research* 51.18, 6395–6403, (2012).

Goshkoderia, A. and Rudykh, S. "Stability of magnetoactive composites with periodic microstructures undergoing finite strains in the presence of a magnetic field". *Composites Part B* 128, 19–29, (2017).

Goshkoderia, A., Arora, N., Slesarenko, V., Li, J., Chen, V., Juhl, A., Buskohl, P., and Rudykh, S. "Tunable permittivity in dielectric elastomer composites under finite strains: Periodicity, randomness, and instabilities." *International Journal of Mechanical Sciences* 186, 105880, (2020).

Goshkoderia, A., Chen, V., Li, J., Juhl, A., Buskohl, P., and Rudykh, S. "Instability-Induced Pattern Formations in Soft Magnetoactive Composites". *Physical Review Letters* 124.15, 158002, (2020).

Greco, F., Leonetti, L., Lonetti, P., Luciano, R., and Pranno, A. "A multiscale analysis of instability-induced failure mechanisms in fiber-reinforced composite structures via alternative modeling approaches". *Composite Structures*, 112529, (2020).

Guan, X., Donga, X., and Ou, J. "Magnetostrictive effect of magnetorheological elastomer". *J. Magn. and Magn. Mat.* 320, 158–63, (2008).

Hoang, N., Zhang, N., and Du, H. "An adaptive tunable vibration absorber using a new magnetorheological elastomer for vehicular powertrain transient vibration reduction". *Smart Mater. Struct.* 20, 015019, (2011).

Hu, W., Lum, G. Z., Mastrangeli, M., and Sitti, M. "Small-scale soft-bodied robot with multimodal locomotion". *Nature* 554.7690, 81–85, (2018).

Ivaneyko, D., Toshchevikov, V., Saphiannikova, M., and Heinrich, G. "Mechanical properties of magneto-sensitive elastomers: unification of the continuum-mechanics and microscopic theoretical approaches". *Soft Matter* 10.13, 2213–2225, (2014).

Javili, A., Chatzigeorgiou, G., and Steinmann, P. "Computational homogenization in magneto-mechanics". *International Journal of Solids and Structures* 50.25-26, 4197–4216, (2013).

Jiles, D. and Atherton, D. "Ferromagnetic hysteresis". *IEEE Transactions on magnetics* 19.5, 2183–2185, (1983).

Jolly, M. R., Carlson, J. D., and Munoz, B. C. "A model of the behaviour of magnetorheological materials". *Smart Mater. Struct.* 5, 607–614, (1996).

Jolly, M. R., Carlson, J. D., and Munoz, B. C. "A model of the behaviour of magnetorheological materials". *Smart materials and structures* 5.5, 607, (1996).

Kankanala, S. V. and Triantafyllidis, N. "On finitely strained magnetorheological elastomers". *J. Mech. Phys. Solids* 52, 2869–2908, (2004).

Kankanala, S. V. and Triantafyllidis, N. "Magnetoelastic buckling of a rectangular block in plane strain". *J. Mech. Phys. Solids* 56, 1147–1169, (2008).

Karami Mohammadi, N., Galich, P. I., Krushynska, A. O., and Rudykh, S. "Soft magnetoactive laminates: large deformations, transverse elastic waves and band gaps tunability by a magnetic field". *Journal of Applied Mechanics* 86.11, (2019).

Kawasetsu, T., Horii, T., Ishihara, H., and Asada, M. "Mexican-hat-like response in a flexible tactile sensor using a magnetorheological elastomer". *Sensors* 18.2, 587, (2018).

Keip, M.-A. and Rambausek, M. "A multiscale approach to the computational characterization of magnetorheological elastomers". *International Journal for Numerical Methods in Engineering* 107.4, 338–360, (2016).

Keip, M.-A. and Rambausek, M. "Computational and analytical investigations of shape effects in the experimental characterization of magnetorheological elastomers". *International Journal of Solids and Structures* 121, 1–20, (2017).

Kim, H., Ahn, S.-k., Mackie, D. M., Kwon, J., Kim, S. H., Choi, C., Moon, Y. H., Lee, H. B., and Ko, S. H. "Shape morphing smart 3D actuator materials for micro soft robot". *Materials Today* 41, 243–269, (2020).

Kim, Y., Yuk, H., Zhao, R., Chester, . A., and Zhao, X. "Printing ferromagnetic domains for untethered fast-transforming soft materials". *Nature* 558, 274–279, (2018).

Kim, Y., Yuk, H., Zhao, R., Chester, S. A., and Zhao, X. "Printing ferromagnetic domains for untethered fast-transforming soft materials". *Nature* 558.7709, 274–279, (2018).

Kim, Y., Parada, G. A., Liu, S., and Zhao, X. "Ferromagnetic soft continuum robots". *Science Robotics* 4.33, eaax7329, (2019).

Kochmann, D. M. and Bertoldi, K. "Exploiting microstructural instabilities in solids and structures: from metamaterials to structural transitions". *Applied mechanics reviews* 69.5, 050801, (2017).

Koo, K. N., Ismail, A. F., Othman, M. H. D., Bidin, N., and Rahman, M. A. "Preparation and characterization of superparamagnetic magnetite (Fe3O4) nanoparticles: A short review". *Malaysian Journal of Fundamental and Applied Sciences*, (2019).

Krishnan, D. and Johnson, H. "Optical properties of two-dimensional polymer photonic crystals after deformation-induced pattern transformations". *J. Mech. Phys. Solids* 57.9, 1500–1513, (2009).

Lanotte, L., Ausanio, G., Iannotti, V., and Luponio Jr, C. "Influence of particle preorientation on elastomagnetic effect in a composite material of ellipsoidal Ni microparticles in a silicone matrix". *Applied Physics A* 77.7, 953–958, (2003).

Lanotte, L., Ausanio, G., Hison, C., Iannotti, V., and Luponio, C. "The potentiality of composite elastic magnets as novel materials for sensors and actuators". *Sensors and Actuators A: Physical* 106.1-3, 56–60, (2003).

Lerner, A. A. and Cunefare, K. A. "Performance of MRE-based vibration absorbers". *J. Intelligent Material Systems and Structures* 19, 551–563, (2008).

Li, J., Slesarenko, V., and Rudykh, S. "Auxetic multiphase soft composite material design through instabilities with application for acoustic metamaterials". *Soft Matter* 14.30, 6171–6180, (2018).

Li, J., Arora, N., and Rudykh, S. "Elastic instabilities, microstructure transformations, and pattern formations in soft materials". *Current Opinion in Solid State and Materials Science* 25.2, 100898, (2021).

Li, J., Pallicity, T. D., Slesarenko, V., Goshkoderia, A., and Rudykh, S. "Domain Formations and Pattern Transitions via Instabilities in Soft Heterogeneous Materials". *Advanced Materials* 31.14, 1807309, (2019).

Li, J. and Rudykh, S. "Tunable microstructure transformations and auxetic behavior in 3D-printed multiphase composites: The role of inclusion distribution". *Composites Part B: Engineering* 172, 352–362, (2019).

Lum, G. Z., Ye, Z., Dong, X., Marvi, H., Erin, O., Hu, W., and Sitti, M. "Shape-programmable magnetic soft matter". *Proceedings of the National Academy of Sciences of the United States of America* 113.41, E6007–E6015, (2016).

Luo, Z., Evans, B. A., and Chang, C.-H. "Magnetically actuated dynamic iridescence inspired by the neon tetra". *Acs Nano* 13.4, 4657–4666, (2019).

Makarova, L. A., Alekhina, Y. A., Rusakova, T. S., and Perov, N. S. "Tunable properties of magnetoactive elastomers for biomedical applications". *Physics procedia* 82, 38–45, (2016).

Maugin, G. A. and Eringen, A. C. "Deformable magnetically saturated media. I. Field equations". *J. Math. Phys.* 13, 143–155, (1972).

Montgomery, S. M., Wu, S., Kuang, X., Armstrong, C. D., Zemelka, C., Ze, Q., Zhang, R., Zhao, R., and Qi, H. J. "Magneto-mechanical metamaterials with widely tunable mechanical properties and acoustic bandgaps". *Advanced Functional Materials* 31.3, 2005319, (2020).

Mooney, M. "A theory of large elastic deformation". *Journal of Applied Physics* 11, 582–592, (1940).

Mooney, M. “A theory of large elastic deformation”. *Journal of applied physics* 11.9, 582–592, (1940).

Moreno, M., Gonzalez-Rico, J., Lopez-Donaire, M., Arias, A., and Garcia-Gonzalez, D. “New experimental insights into magneto-mechanical rate dependences of magnetorheological elastomers”. *Composites Part B: Engineering* 224, 109148, (2021).

Moreno-Mateos, M. A., Hossain, M., Steinmann, P., and Garcia-Gonzalez, D. “Hybrid magnetorheological elastomers enable versatile soft actuators”. *npj Computational Materials* 8.1, 162, (2022).

Moreno-Mateos, M. A., Hossain, M., Steinmann, P., and Garcia-Gonzalez, D. “Hard magnetics in ultra-soft magnetorheological elastomers enhance fracture toughness and delay crack propagation”. *Journal of the Mechanics and Physics of Solids* 173, (2023).

Moskvin, M. et al. “Cerium Oxide-Decorated γ-Fe2O3 Nanoparticles: Design, Synthesis and in vivo Effects on Parameters of Oxidative Stress”. *Frontiers in Chemistry* 8, 682, (Aug. 2020).

Mukherjee, D., Rambausek, M., and Danas, K. “An explicit dissipative model for isotropic hard magnetorheological elastomers”. *Journal of the Mechanics and Physics of Solids* 151, 104361, (2021).

Naseer, N., Fatima, H., Asghar, A., Fatima, N., Ahmed, N., Khan, A. U., and Ahmad, N. M. “Magnetically responsive hybrid polymer colloids for ultrasensitive molecular imaging”. *Journal of Colloid Science and Biotechnology* 3.1, 19–29, (2014).

Nguyen, H. H., Ta, H. K. T., Park, S., Phan, T. B., and Pham, N. K. “Resistive switching effect and magnetic properties of iron oxide nanoparticles embedded-polyvinyl alcohol film”. *RSC Advances* 10.22, 12900–12907, (2020).

Ogden, R. W. “On the thermoelastic modeling of rubber-like solids”. *J. of Thermal Stresses* 15, 533–557, (1992).

Ottenio, M., Destrade, M., and Ogden, R. “Incremental Magnetoelastic Deformations, with Application to Surface Instability”. *Journal of Elasticity* 90, 19–42, (2008).

Pal, A. and Sitti, M. “Programmable mechanical devices through magnetically tunable bistable elements”. *Proceedings of the National Academy of Sciences of the United States of America* 120.15, e2212489120, (2023).

Pathak, P., Arora, N., and Rudykh, S. “Magnetoelastic instabilities in soft laminates with ferromagnetic hyperelastic phases”. *International Journal of Mechanical Sciences* 213, 106862, (2022).

Piranda, B., Chodkiewicz, P., Hołobut, P., Bordas, S. P., Bourgeois, J., and Lengiewicz, J. “Distributed prediction of unsafe reconfiguration scenarios of modular robotic programmable matter”. *IEEE Transactions on Robotics* 37.6, 2226–2233, (2021).

Ponte Castañeda, P. and Galipeau, E. "Homogenization-based constitutive models for magnetorheological elastomers at finite strain". *J. Mech. Phys. Solids* 59, 194–215, (2011).

Psarra, E., Bodelot, L., and Danas, K. "Two-field surface pattern control via marginally stable magnetorheological elastomers". *Soft Matter* 13.37, 6576–6584, (2017).

Qi, S., Guo, H., Fu, J., Xie, Y., Zhu, M., and Yu, M. "3D printed shape-programmable magneto-active soft matter for biomimetic applications". *Composites Science and Technology* 188, 107973, (2020).

Rigbi, Z. and Jilken, L. "The response of an elastomer filled with soft ferrite to mechanical and magnetic influences". *Journal of magnetism and magnetic materials* 37.3, 267–276, (1983).

Rivlin, R. S. "Large Elastic Deformations of Isotropic Materials. V. The Problem of Flexure". *Proc. R. Soc. A* 195.1043, 463–473, (1949).

Rudykh, S. and Bertoldi, K. "Stability of Anisotropic Magnetorheological Elastomers in Finite Deformations: a Micromechanical Approach." *J. Mech. Phys. Solids* 61, 949–967, (2013).

Rudykh, S. and Boyce, M. "Transforming Wave Propagation in Layered Media via Instability-induced Interfacial Wrinkling". *Phys. Rev. Lett.* 112, 034301, (2014).

Rudykh, S. and deBotton, G. "Stability of anisotropic electroactive polymers with application to layered media". *Z. Angew. Math. Phys.* 62, 1131–1142, (2011).

Rudykh, S. and deBotton, G. "Instabilities of hyperelastic fiber composites: micromechanical versus numerical analyses". *J. Elasticity* 106, 123–147, (2012).

Rudykh, S., Lewinstein, A., Uner, G., and deBotton, G. "Analysis of microstructural induced enhancement of electromechanical coupling in soft dielectrics". *Appl. Phys. Lett.* 102, 151905, (2013).

Rus, D. and Tolley, M. T. "Design, fabrication and control of soft robots". *Nature* 521.7553, 467–475, (2015).

Scott, J. F. "Applications of magnetoelectrics". *Journal of Materials Chemistry* 22.11, 4567–4574, (2012).

Shim, J., Shan, S., Košmrlj, A., Kang, S. H., Chen, E. R., Weaver, J. C., and Bertoldi, K. "Harnessing instabilities for design of soft reconfigurable auxetic/chiral materials". *Soft Matter* 9.34, 8198–8202, (2013).

Sim, J., Wu, S., Dai, J., and Zhao, R. R. "Magneto-Mechanical Bilayer Metamaterial with Global Area-Preserving Density Tunability for Acoustic Wave Regulation". *Advanced Materials* 35.35, e2303541, (2023).

Slesarenko, V. and Rudykh, S. "Harnessing viscoelasticity and instabilities for tuning wavy patterns in soft layered composites". *Soft Matter* 12, 3677–3682, (2016).

Slesarenko, V. and Rudykh, S. “Microscopic and macroscopic instabilities in hyperelastic fiber composites”. *J. Mech. Phys. Solids* 99, 471–482, (2017).

Soria-Hernández, C. G., Palacios-Pineda, L. M., Elıas-Zúiga, A., Perales-Martınez, I. A., and Martınez-Romero, O. “Investigation of the effect of carbonyl iron micro-particles on the mechanical and rheological properties of isotropic and anisotropic MREs: constitutive magneto-mechanical material model”. *Polymers* 11.10, 1705, (2019).

Stanier, D. C., Ciambella, J., and Rahatekar, S. S. “Fabrication and characterisation of short fibre reinforced elastomer composites for bending and twisting magnetic actuation”. *Composites Part A: Applied Science and Manufacturing* 91, 168–176, (2016).

Stoner, E. and Wohlfarth, E. “A mechanism of magnetic hysteresis in heterogeneous alloys”. *IEEE Transactions on Magnetics* 27.4, 3475–3518, (1991).

Sun, S., Yang, J., Li, W., Deng, H., Du, H., Alici, G., and Yan, T. “An innovative MRE absorber with double natural frequencies for wide frequency bandwidth vibration absorption”. *Smart Materials and Structures* 25.5, 055035, (2016).

Sunaryono, S., Taufiq, A., Munaji, M., Indarto, B., Triwikantoro, T., Zainuri, M., and Darminto, D. “Magneto-elasticity in Hydrogels Containing Fe3O4 Nanoparticles and Their Potential Applications”. *AIP Conference Proceedings* 1555, 53–56, (Sept. 2013).

Szczygłowski, J. “Influence of eddy currents on magnetic hysteresis loops in soft magnetic materials”. *Journal of Magnetism and Magnetic Materials* 223.1, 97–102, (2001).

Tan, K., Wen, X., Gong, X., Deng, Q., and Shen, S. “Diversifying temporal responses of magnetoactive elastomers”. *Materials Research Express* 7.4, 045702, (2020).

Tang, J., Qiao, Y., Chu, Y., Tong, Z., Zhou, Y., Zhang, W., Xie, S., Hu, J., and Wang, T. “Magnetic double-network hydrogels for tissue hyperthermia and drug release”. *Journal of materials chemistry B* 7.8, 1311–1321, (2019).

Tang, S.-Y. et al. “Versatile microfluidic platforms enabled by novel magnetorheological elastomer microactuators”. *Advanced Functional Materials* 28.8, 1705484, (2018).

Tian, L., Tevet-Deree, L., deBotton, G., and Bhattacharya, K. “Dielectric elastomer composites”. *J. Mech. Phys. Solids* 60, 181–198, (2012).

Tian, T. F., Li, W. H., and Deng, Y. M. “Sensing capabilities of graphite based MR elastomers”. *Smart Mater. Struct.* 20, 025022, (2011).

Tiersten, H. “Coupled magnetomechanical equations for magnetically saturated insulators”. *J. Math. Phys.* 5.9, 1298–1318, (1964).

Toupin, R. A. “The Elastic Dielectric”. *Arch. Rational. Mech. Anal.* 5.6, 849–915, (1956).

Triantafyllidis, N. and Maker, B. N. “On the comparison between microscopic and macroscopic instability mechanisms in a class of fiber-reinforced composites”. *J. Appl. Mech., Trans. ASME* 52, 794–800, (1985).

Varga, Z., Filipcsei, G., and Zrinyi, M. "Smart composites with controlled anisotropy". *Polymer* 46.18, 7779–7787, (2005).

Vu, D. K. and Steinmann, P. "Nonlinear electro- and magneto-elastostatics: Material and spatial settings". *Int. J. Solids Struct.* 44.24, 7891–7905, (2007).

Wang, L., Zheng, D., Harker, P., Patel, A. B., Guo, C. F., and Zhao, X. "Evolutionary design of magnetic soft continuum robots". *Proceedings of the National Academy of Sciences* 118.21, e2021922118, (2021).

Wang, Q., Dong, X., Li, L., and Ou, J. "Mechanical modeling for magnetorheological elastomer isolators based on constitutive equations and electromagnetic analysis". *Smart Materials and Structures* 27.6, 065017, (2018).

Wu, B. and Destrade, M. "Wrinkling of soft magneto-active plates". *International Journal of Solids and Structures* 208, 13–30, (2021).

Yan, D., Aymon, B. F. G., and Reis, P. M. "A reduced-order, rotation-based model for thin hard-magnetic plates". *Journal of the Mechanics and Physics of Solids* 170, 105095, (2023).

Yan, D., Pezzulla, M., Cruveiller, L., Abbasi, P. M., and Reis, P. M. "Magneto-active elastic shells with tunable buckling strength". *Nature Communications* 12.1, 2831, (2021).

Yang, J., Gong, X., Deng, H., Qin, L., and Xuan, S. "Investigation on the mechanism of damping behavior of magnetorheological elastomers". *Smart materials and structures* 21.12, 125015, (2012).

Yang, X. and Keten, S. "Emergent elasticity relations for networks of bars with sticky magnetic ends". *Extreme Mechanics Letters* 65, 102093, (2023).

Yim, S. and Sitti, M. "Design and rolling locomotion of a magnetically actuated soft capsule endoscope". *IEEE Transactions on Robotics* 28.1, 183–194, (2011).

Yoon, J.-H., Yang, I.-H., Jeong, U.-C., Chung, K.-H., Lee, J.-Y., and Oh, J.-E. "Investigation on variable shear modulus of magnetorheological elastomer based on natural rubber due to change of fabrication design". *Polymer Engineering & Science* 53.5, 992–1000, (2013).

Yu, K., Fang, N. X., Huang, G., and Wang, Q. "Magnetoactive acoustic metamaterials". *Advanced Materials* 30.21, 1706348, (2018).

Zadov, B., Elmalem, A., Paperno, E., Gluzman, I., Nudelman, A., Levron, D., Grosz, A., Lineykin, S., and Liverts, E. "Modeling of Small DC Magnetic Field Response in Trilayer Magnetoelectric Laminate Composites". *Advances in Condensed Matter Physics* 18, 383728, (2012).

Zhang, Q., Cherkasov, A. V., Xie, C., Arora, N., and Rudykh, S. "Nonlinear elastic vector solitons in hard-magnetic soft mechanical metamaterials". *International Journal of Solids and Structures* 280, 112396, (2023).

Zhang, Q., Cherkasov, A. V., Arora, N., Hu, G., and Rudykh, S. "Magnetic field-induced asymmetric mechanical metamaterials". *Extreme Mechanics Letters* 59, 101957, (2023).

Zhang, Q. and Rudykh, S. "Magneto-deformation and transverse elastic waves in hard-magnetic soft laminates". *Mechanics of Materials* 169, 104325, (2022).

Zhao, R., Kim, Y., Chester, S. A., Sharma, P., and Zhao, X. "Mechanics of hard-magnetic soft materials". *Journal of the Mechanics and Physics of Solids* 124, 244–263, (2019).

Zhou, C. et al. "Ferromagnetic soft catheter robots for minimally invasive bioprinting". *Nature communications* 12.1, 5072, (2021).

Zrínyi, M., Barsi, L., and Büki, A. "Deformation of ferrogels induced by nonuniform magnetic fields". *The Journal of chemical physics* 104.21, 8750–8756, (1996).

Miscellaneous

Developers, G. *Magnetic permeability*. URL: https://em.geosci.xyz/content/physical_properties/magnetic_permeability/index.html, (2017).

Martínez, L. M. *Magnetic properties of nanoparticles*. URL: https://www.sepmag.eu/blog/magnetic-properties-of-nanoparticles, (Feb. 2018).